

2020
Volume 3
Issue 1
ISSN: 2578-2010

APPLIED CHEMICAL ENGINEERING

Volume 3 Issue 1 <https://systems.enpress-publisher.com/index.php/ACE>



ISSN 2578-2010



9 772578 201035

ACE



Editorial Board

Editor-in-Chief

Prof. Sivanesan Subramanian

Anna University
India

Prof. Hassan Karimi-Maleh

Department of Chemical Engineering, Laboratory of Nanotechnology,
Quchan University of Technology
Islamic Republic of Iran

Associate Editor

Prof. György Keglevich

Department of Organic Chemical Technology
Hungary

Editorial Board Member

Dr. Subrata Ghosh

The University of Manchester
United Kingdom

Dr. Michela Langone

University of Trento
Italy

Dr. Pradeep Lancy Menezes

University of Nevada Reno
United States

Prof. Judit Telegdi

Research Centre for Natural Sciences,
Hungarian Academy of Sciences
Hungary

Dr. Sadin Ozdemir

Mersin University
Turkey

Dr. Anita Tarbuk

University of Zagreb Faculty of Textile
Technology
Croatia

Dr. Rocio Maceiras

Centro Universitario de la Defensa
Spain

Prof. Vladimir Zaichick

Medical Radiological Research Center
Russian Federation

Dr. Munirah Abdullah

Imam Abdulrahman Bin Faisal University
Saudi Arabia

Dr. Khalisanni Khalid

Malaysian Agricultural Research and
Development Institute (MARDI)
Malaysia

Prof. Michael Daramola

University of the Witwatersrand
South Africa

Prof. Mahammad Babanly

Institute of Catalysis and Inorganic Chemistry,
Azerbaijan National Academy of Science
Azerbaijan

Applied Chemical Engineering

Editor-in-Chief

Prof. Sivanesan Subramanian

Anna University

India

Prof. Hassan Karimi-Maleh

Department of Chemical Engineering,

Laboratory of Nanotechnology,

Quchan University of Technology

Islamic Republic of Iran

Applied Chemical Engineering

<https://systems.enpress-publisher.com/index.php/ACE>

Contents

Original Research Article

- 1 Simulation study of pressure swing adsorption to purify helium using zeolite 13X**
Ehsan Javadi Shokroo, Mehdi Farniaei, Mehdi Baghbani
- 8 Efficiency of single and mixed dimeric surfactants micelles on solubilization of polycyclic aromatic hydrocarbons**
Naveen Kumar, Rashmi Tyagi, V.K. Tyagi
- 14 Heavy metal-induced oxidative stress and DNA damage as shown by RAPD-PCR in leaves of *Elodea canadensis***
Dilek Demirezen Yilmaz, Nuri Ercan, Fahriye Sumer Ercan
- 23 Iron removal from ground water using Egyptian cost-effective clay minerals**
H.M. Abdel-Ghafar, E.A. Abdel-Aal, B. E. El Anadouli
- 31 Photocatalytic oxidation of psychoactive drug Duloxetine: Degradation kinetics, inorganic ions and phytotoxicity evaluation**
Sophia Tsoumachidou, Maria Valari, Ioannis Poullos
- 43 Copper and lead ions removal from aqueous solution using MgO, nanostructured MgO**
Salah N. Farhan, Anees Abdullah Khadom, Abdul Mun'em Abbas Karim
- 49 Kinetics of dechlorination of atrazine using tin (SnII) at neutral pH conditions**
Vijay Kumar, Simranjeet Singh

Review Article

- 55 Carbon nanomaterials for metal-free electrocatalysis**
Ana M.B. Honorato, Mohd. Khalid

ORIGINAL RESEARCH ARTICLE

Simulation study of pressure swing adsorption to purify helium using zeolite 13X

Ehsan Javadi Shokroo^{1,2*}, Mehdi Farniaei¹, Mehdi Baghbani¹

¹ FAPKCO Engineering Group, Elite Foundation for Southern Zone, Shiraz, Iran. E-mail: ehsan.javadi@hotmail.com; mehdi.farniaei@yahoo.com; baghbani2003@yahoo.com

² Faculty of Engineering, Selinus University of Sciences and Literature, 40138 Bologna BO, Italy.

ABSTRACT

A two-bed pressure swing adsorption system on a commercial type of zeolite 13X adsorbent has been studied numerically over a wide range of operating conditions to helium separation from gaseous mixture. The model includes energy, mass and momentum balances. The coupled partial differential equations are solved using fully implicit fourth order Rung-Kutta scheme in the simulation. The effects of adsorption step pressure, adsorption step time and feed flow rate on the helium purity and recovery were investigated. Results shown that as the adsorption step pressure increases the helium purity will be increased. In addition, the helium recovery increases, and the helium purity decreases when the feed flow rate increases. Finally, the simulation results indicated a very good agreement with some current literature experimental work.

Keywords: Pressure Swing Adsorption; Helium Recovery; Mathematical Modeling; Numerical Simulation; Zeolite 13X

ARTICLE INFO

Received 4 January 2020
Accepted 27 February 2020
Available online 1 March 2020

COPYRIGHT

Copyright © 2020 Ehsan Javadi Shokroo, et al.
EnPress Publisher LLC. This work is licensed under the Creative Commons Attribution-NonCommercial 4.0 International License (CC BY-NC 4.0).
<http://creativecommons.org/licenses/by-nc/4.0/>

1. Introduction

Helium is a chemical element with symbol He and atomic number 2. It is a colorless, odorless, tasteless, non-toxic, inert and monatomic gas, which is the first in the noble gas group in the periodic table. The boiling and melting points of He are the lowest among all the elements.

Helium is the second lightest element and is the second most abundant element in the observable universe, being present at about 24% of the total elemental mass, which is more than 12 times the mass of all the heavier elements combined. Helium was first detected as an unknown yellow spectral line signature in sunlight during a solar eclipse in 1868 by French astronomer Jules Janssen. In 1903, large reserves of helium were found in natural gas fields in parts of the United States, which is by far the largest supplier of the gas today.

Liquid helium is used in cryogenics (its largest single use, absorbing about a quarter of production), particularly in the cooling of superconducting magnets, with the main commercial application being in MRI scanners. Helium's other industrial uses—as a pressurizing and purge gas, as a protective atmosphere for arc welding and in processes such as growing crystals to make silicon wafers, account for half of the gas produced. A well-known but minor use is as a lifting gas in balloons and airships^[1]. On the Earth, it is relatively rare 5.2 ppm by volume in the atmosphere.

Pressure swing adsorption (PSA) process is a wide operating unit to separate and purify the gases that operates based on capability of solids ad-

sorption and selective separation of gases. The important operational parameter in this system is the pressure, and most industrial units operate at/or vicinity of the surrounding temperature. Today, the PSA process is completely known in a wide region of the processes, and this process was preferred in contrast to other conventional separation methods, especially for lower capacity and higher purity.

Linde Group developed the world's first air separation plant for the production of oxygen in 1902 and the first production facility was set up as early as 1903. Since then, it is one of the world's largest helium suppliers and since 1994 Linde has been the sole provider of helium and helium separators by the method of swing adsorption. Bhushan^[2] purified helium by gas adsorption method in 2011. The purifier was designed to purify up to 40% impurity to give 4.5 grade or 99.995% pure helium by high pressure and low temperature cryosorption process. Activated carbons have been used for a long time at low temperature for cryogenic applications. The pore geometry and size can be used to optimize the carbon structure for a specific application. In 1978, Stoll *et al.*^[3] commissioned a fully automatic large capacity helium purifier which included operation, regeneration, re-cooling and re-pressurization time. In 2007, E. Van Cleve *et al.*^[4] developed a cryogenic pulsed laser deposition (PLD) system to deposit lithium films onto a quartz crystal microbalance (QCM) and adsorption isotherms of 4 He on lithium were measured. PLD system was used to form lithium substrates and the first helium adsorption measurements on this surface were reported. In 2008, Nisith Kr. Das^[1] employed a technique known as pressure swing adsorption to concentrate a lean amount of helium present in natural gas through selective physical elimination of N₂, CO₂, CH₄ and heavier hydrocarbons in a stepwise cycle sequence at present time intervals. In 2011, D. Martins *et al.*^[5] reported on the low temperature adsorption properties

of He, H₂, and N₂, using three activated carbons with different pore size distributions. In 2012, R. Majidia *et al.*^[6] used the molecular dynamics simulation to study the helium adsorption on the CNCs with a declination angle of 240° and 300°. The results indicated that the adsorption capacity of the CNCs became considerable by decreasing the declination angle. In the same year, Nisith Kr. Das *et al.*^[7] developed a helium purification system using a three-bed seven-step pressure swing adsorption (PSA). It removed impurities like N₂ and O₂ from a ternary mixture leaving out high-purity helium from the gas mixture. The PSA system operated successfully resulting in high-purity helium (>99.9%) with a yield of around 89%. The adsorption capability of carbon dioxide on 5A molecular sieve (5AMS) was investigated in a fixed-bed apparatus with two-road gas mixing system by dynamic column breakthrough method with helium as the carrier gas for helium purification system of high-temperature gas-cooled reactor (HTGR) in 2013 by Chang Hua *et al.*^[8]

In 2014, Bartolomei *et al.*^[9] performed quantum dynamical simulations on reliable new force fields in order to assess the graphdiyne capability for helium chemical and isotopic separation.

In this work, a semi-industrial PSA unit for helium recovery from gaseous mixture was simulated. In this process, the effect of some operating variables such as adsorption time, feed flow rate, and adsorption pressure on process performance was investigated. The simulated PSA process is a six-step process with the following sequence (**Figure 1**): (I) co-current feed pressurization (PR); (II) high-pressure adsorption (AD) step; (III) counter-current depressurizing pressure equalization (ED) step; (IV) counter-current blow down (BD) step; (V) counter-current purge with a light product (PG) step; (VI) co-current pressurizing pressure equalization (EP) step. The sequence time table of the PSA process was also depicted in **Table 1**.

Table 1. Step sequence of the PSA process

No.	1	2	3	4	5	6
Time (sec.)	25	60	10	25	60	10
Column 1	PR	AD	ED	BD	PG	EP
Column 2	BD	PG	EP	PR	AD	ED
SV1	on	on	off	on	on	off
SV2	off	off	on	off	off	off
SV3	off	off	off	off	off	on
SV4	on	on	off	on	on	off
SV5	on	on	off	on	on	off
SV6	on	on	off	on	on	off
SV7	off	off	off	off	on	off
SV8	off	on	off	off	off	off
SV9	off	off	off	off	on	off
SV10	off	on	off	off	off	off
SV11	off	on	off	off	on	off
SV12	off	on	off	off	off	off
SV13	off	off	off	on	on	off

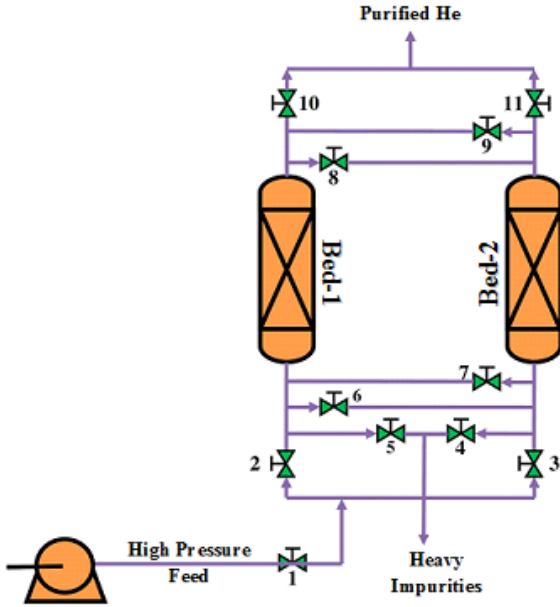


Figure 1. Schematic diagram of He-PSA.

2. Mathematical model

In order to develop a mathematical model for an adsorption bed, the following assumptions were made:

- 1- Gas behaves as an ideal gas;
- 2- The flow pattern is axially assumed as plug-flow model;
- 3- Equilibrium equations for air are expressed as multi-component Langmuir-Freundlich isotherm;
- 4- Rate of mass transfer is presented by linear driving force (LDF) relations;
- 5- Bed is clean at initial state and there is no gas flow in it;

According to these assumptions, dynamic be-

havior of system in terms of mass, energy and momentum balances can be expressed as follows:

Dimensionless partial mass balance for gas phase in the adsorption bed is^[9-12]:

$$-\left(\frac{1}{P_0^m}\right) \cdot \frac{\partial^2 y_i}{\partial z^2} + y_i \cdot \frac{\partial \hat{u}}{\partial z} + \hat{u} \cdot \left(\frac{\partial y_i}{\partial z} + y_i \cdot \left(\frac{1}{\hat{P}} \cdot \frac{\partial \hat{P}}{\partial z} - \frac{1}{\hat{T}} \cdot \frac{\partial \hat{T}}{\partial z}\right)\right) + \frac{\partial y_i}{\partial \tau} + y_i \cdot \left(\frac{1}{\hat{P}} \cdot \frac{\partial \hat{P}}{\partial \tau} - \frac{1}{\hat{T}} \cdot \frac{\partial \hat{T}}{\partial \tau}\right) + \left(\frac{\rho_p \cdot R \cdot T_0 \cdot \hat{T}}{P_0 \cdot \hat{P}}\right) \cdot \left(\frac{1-\varepsilon}{\varepsilon}\right) \cdot \left(q_{m,i} \cdot \frac{\partial \hat{q}_i}{\partial \tau} + \hat{q}_i \cdot \frac{\partial q_{m,i}}{\partial \tau}\right) = 0 \quad (1)$$

Dimensionless equilibrium loading of i th component for solid phase in the adsorption bed is:

$$\frac{\partial q_{m,i}}{\partial \tau} = \frac{\partial q_{m,i}}{\partial \hat{T}} \times \frac{\partial \hat{T}}{\partial \tau} = k_{2,i} T_0 \times \frac{\partial \hat{T}}{\partial \tau} \quad (2)$$

Dimensionless loading of i th component for solid phase in the adsorption bed is (LDF relation):

$$\frac{\partial \hat{q}_i}{\partial \tau} = \alpha_i \cdot \left(\frac{\beta_i y_i^{n_i}}{1 + \sum_{j=1}^N \beta_j y_j^{n_j}} - \hat{q}_i\right) - \left(\hat{q}_i \cdot \frac{\partial q_{m,i}}{\partial \tau}\right) \quad (3)$$

According to equation (3), the LDF relation depends on various parameters such as: equilibrium parameter for the Langmuir model, mole fraction of species i in the gas phase, average amount adsorbed and equilibrium parameter for the Langmuir model.

The equilibrium of triple Langmuir-Freundlich isotherm is as follows:

$$\hat{q}_i^* = \frac{\beta_i y_i^{n_i}}{1 + \sum_{j=1}^N \beta_j y_j^{n_j}} \quad (4)$$

where β , n and q_m are as follows:

$$q_{m,i} = k_1 + k_2 T_0 \hat{T} \quad (5)$$

$$\beta_i = k_3 \exp\left(\frac{k_4}{T_0 \hat{T}}\right) \quad (6)$$

$$n = k_5 + \frac{k_6}{T_0 \hat{T}} \quad (7)$$

Overall dimensionless mass balance for gas phase in the adsorption bed is^[13-16]:

$$\left(\frac{1}{\hat{P}}\right) \cdot \frac{\partial \hat{P}}{\partial \tau} + \frac{\partial \hat{u}}{\partial z} + \hat{u} \cdot \frac{\partial \hat{P}}{\partial z} - \left(\frac{1}{\hat{T}}\right) \cdot \left(\frac{\partial \hat{T}}{\partial \tau} + \hat{u} \cdot \frac{\partial \hat{T}}{\partial z}\right) + \left(\frac{P_p R T_0 \hat{T}}{P_0 \hat{P}}\right) \cdot \left(\frac{1-\varepsilon}{\varepsilon}\right) \cdot \sum_{i=1}^3 \left(q_{m,i} \cdot \frac{\partial \hat{q}_i}{\partial \tau} + \hat{q}_i \cdot \frac{\partial q_{m,i}}{\partial \tau}\right) = 0 \quad (8)$$

Dimensionless energy balance for gas phase in the adsorption bed is^[17-21]:

$$-\left(\frac{1}{\rho_p^h}\right) \cdot \frac{\partial^2 \hat{T}}{\partial z^2} + \varepsilon \cdot \left(\hat{u} \frac{\partial \hat{T}}{\partial z} + \hat{T} \frac{\partial \hat{u}}{\partial z}\right) + \left(\varepsilon_t + \frac{\rho_B \cdot c_{p,s}}{\rho_g \cdot c_{p,g}}\right) \cdot \frac{\partial \hat{T}}{\partial \tau} - \left(\frac{\rho_B}{T_0 \cdot \rho_g \cdot c_{p,g}}\right) \cdot \frac{\partial \hat{T}}{\partial \tau} - \left(\frac{\rho_B}{T_0 \cdot \rho_g \cdot c_{p,g}}\right) \cdot \frac{\partial \hat{T}}{\partial \tau} = 0$$

$$\sum_{i=1}^3 \left[(q_{m,i} \cdot \frac{\partial \hat{q}_i}{\partial \tau} + \hat{q}_i \cdot \frac{\partial q_{m,i}}{\partial \tau}) \cdot (-\Delta \bar{H}_i) \right] + \left(\frac{2h_i L}{R_{B,i} U_0 \rho_g c_{p,g}} \right) \cdot (\hat{T} - \hat{T}_w) = 0 \quad (9)$$

Dimensionless energy balance for the wall of adsorption bed is:

$$\frac{\partial \hat{T}_w}{\partial \tau} = \left[\frac{2\pi \cdot R_{B,i} \cdot h_i \cdot L}{\rho_w \cdot c_{p,w} \cdot A_w \cdot U_0} \right] \cdot (\hat{T} - \hat{T}_w) - \left[\frac{2\pi \cdot R_{B,o} \cdot h_o \cdot L}{\rho_w \cdot c_{p,w} \cdot A_w \cdot U_0} \right] \cdot (\hat{T}_w - \frac{T_{atm}}{T_0}) \quad (10)$$

Cross-sectional area of adsorption bed wall is:

$$A_w = \pi \cdot (R_{B,o}^2 - R_{B,i}^2) \quad (11)$$

Ergun equation is utilized in order to investigate the pressure drop across the adsorption bed^[22,23].

$$-\frac{d\hat{P}}{d\hat{z}} = [a \cdot \mu \cdot U_0 \cdot \hat{u} + b \cdot \rho \cdot U_0^2 \cdot \hat{u} \cdot |\hat{u}|] \cdot \left(\frac{L}{P_0}\right) \quad (12)$$

$$a = \frac{150}{4R_p^2} \cdot \frac{(1-\varepsilon)^2}{\varepsilon^2}; b = 1.75 \frac{(1-\varepsilon)}{2R_p \varepsilon} \quad (13)$$

Physical properties of adsorbents and characteristics of adsorption bed are depicted in **Tables 2** and **3**, respectively.

Table 2. Physical properties of bed and adsorbent^[24]

Characteristic	Zeolite 13X
Type	Sphere
Average pellet size, R_p (cm)	0.07
Pellet density, ρ_p (g/cm ³)	1.17
Heat capacity, C_{ps} (cal/g.K)	0.32
Bed porosity, ε	0.391
Bed density, ρ_B (g/cm ³)	0.713

Table 3. Adsorption bed properties^[25]

Characteristic	Zeolite 13X
Length, L (cm)	76
Inside radius, R_{Bi} (cm)	2.138
Outside radius, R_{Bo} (cm)	2.415
Heat capacity of the column, C_{pw} (cal/g.K)	0.12
Density of column, ρ_w (g/cm ³)	7.83
Internal heat-transfer coefficient, h_i (cal/cm ² .K.s)	9.2×10^{-4}
External heat-transfer coefficient, h_o (cal/cm ² .K.s)	3.4×10^{-4}
Axial thermal conductivity, K_L (cal/cm.s.K)	6.2×10^{-5}
Axial dispersion coefficient, D_L (cm ² /s)	1×10^{-5}

3. Results and discussion

The fourth order Runge-Kutta Gill scheme was used to solve a mathematical model considered as coupled partial differential equations. The experimental data obtained from literatures has been simulated in order to validate the simulation results in this study^[10,22,26]. An experimental and simulation

study of a PSA unit which is running a traditional Skarstrom cycle and a Skarstrom cycle with co-current equalization owing to separate oxygen from air using a 5A zeolite has been proposed by Mendes *et al.*^[11] in 2001. Moreover, a small-scale two-bed six-step PSA process using zeolite 13X was performed by Jee *et al.*^[27-30] in order to provide oxygen-enriched air. They showed that there is a strong effect of feed flow rate on O₂ purity. The effects of adsorption and desorption on zeolite 5A and CMS beds were investigated in a mixture of N₂/O₂/Ar by Jee *et al.*^[28] in 2004. A non-isothermal mathematical model was applied in order to simulate the adsorption dynamics in their studies^[26].

Figures 2(a) and **(b)** indicate the effect of product flow rate and P/F on the purity and recovery of oxygen during PSA process, respectively. The impact of temperature variations in gas phase during adsorption as a function of time is illustrated in **Figure 2(c)**. It is obviously seen that there is a relatively high accuracy in the simulation of experimental data^[27].

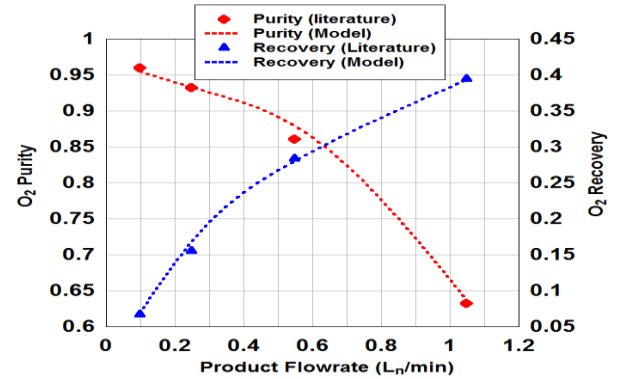


Figure 2a. Numerical simulation of experimental data in this work^[23].

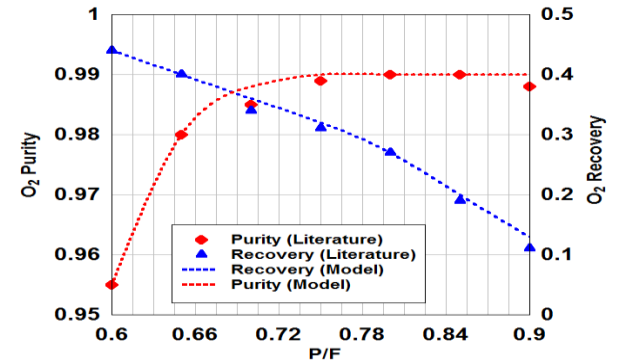


Figure 2b. Numerical simulation of experimental data in this work^[10].

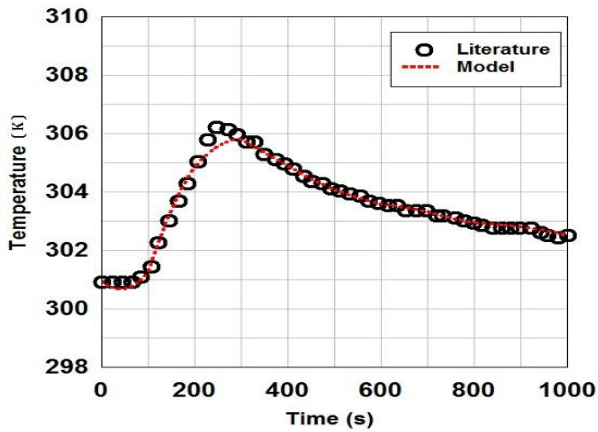


Figure 2c. Numerical simulation of experimental data in this work^[26].

Figure 3 shows the effects of feed flow rate on helium purity and recovery at adsorption pressure of 8.5 bar and adsorption time of 20 sec. In this figure it can be seen that the increase in feed leads to a decrease in the helium purity while helium recovery has increased. The feed flow will rise at a constant purge flow in these simulations, which the P/F decreases and subsequently helium purity decreases. At a certain purge flow rate when the feed amount increases therefore, the P/F ratio is reduced and finally, the product purity decreases. In the other word, dead space of the bed in the adsorption step will rise with the feed flow rate. Thus, purging the bed in the purge step requires more purgative flow. In these simulations, a constant purge flow rate causes a reduction in the helium purity with the feed flow rate.

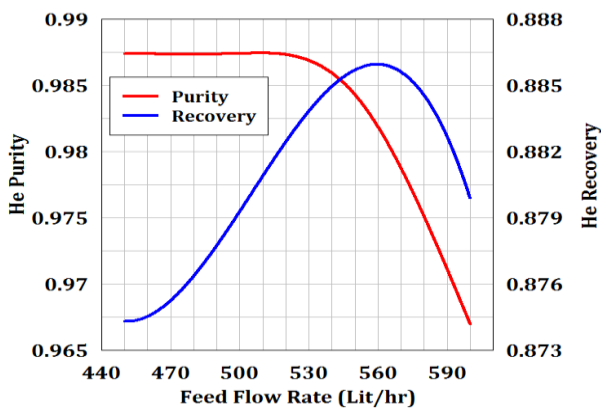


Figure 3. Helium purity and recovery variations versus feed flow rate.

The variations of helium purity and recovery in terms of adsorption step time at pressure of 5.5 bar and P/F of 0.1 are shown in **Figure 4**. It is clear from this figure that increase of adsorption

time leads to reduction in helium purity. It is due to the well-known breakthrough time of the adsorption beds. Thus, the adsorption time should be near to the breakthrough time in order to achieve the maximum process performance in terms of adsorption time. In fact, the adsorption time is a required time for occurring breakthrough time. After this time, the product purity is decreased while the entire capacity of the bed has not utilized before this time. Therefore, the adsorption time must be close to the breakthrough time in order that the best process performance in terms of adsorption time is achieved^[10]. With referring to this figure, the best time for adsorption is 25 sec. Furthermore, it should be noted that, the helium recovery is in reverse order with its purity at all points. It was evident that the recovery reduces as the gas volume of the feed increases through increasing the adsorption time. **Figure 5** shows the effect of adsorption step pressure on the process performance. It is apparent from this figure that the higher adsorption pressure improves the PSA unit performance. As the adsorption pressure increases, the amount of adsorbed heavy species on the adsorbent will be increased and therefore, the helium purity increases. For the favorable isotherm systems, if the pressure is increased, the highly adsorbed species are more adsorbed and the product purity will be increased. This result was seen in the literature^[10-12,15,16,21,26,31,32]. Helium concentration profile curves are depicted in **Figure 6**. It is obvious from this figure that the helium purity has a minimum and maximum quantity in the blow down step because of depressurized bed and the pressurization step as result of the cleansed bed, respectively.

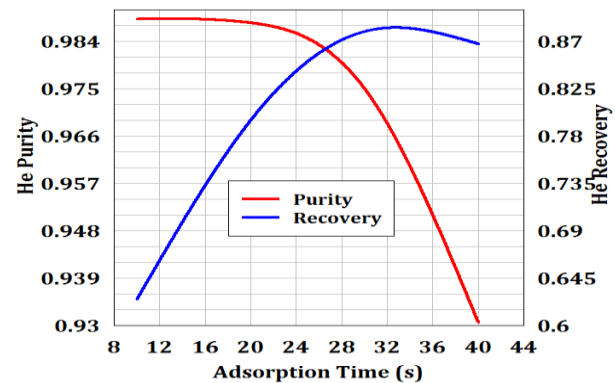


Figure 4. Variations of helium purity and recovery in terms of adsorption step time.

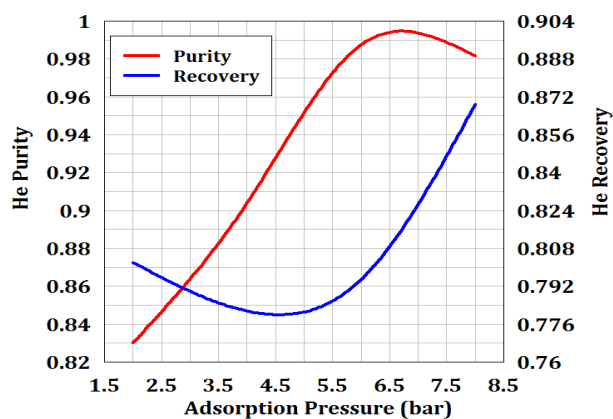


Figure 5. Variations of helium purity and recovery in terms of adsorption step pressure.

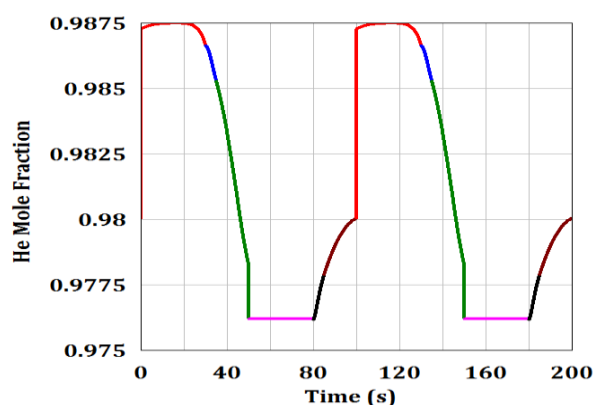


Figure 6. Helium concentration profile along a whole cycle at the top of the bed.

4. Conclusions

Helium separation from gaseous mixture in a two-bed pressure swing adsorption setup on a commercial type of zeolite 13X adsorbent has been studied numerically over a wide range of operating conditions. The influences of adsorption step pressure, adsorption step time and feed flow rate on the process performance were investigated. Results showed that as the adsorption step pressure increases, the helium purity will be increased. The time of the adsorption step is clearly defined through the physical properties of the bed such as length, diameter, adsorbent type as well as the feed flow rate. Furthermore, the helium recovery increases, and the helium purity decreases when the feed flow rate increases. Finally, a considerable agreement was found between the experimental data and the simulation results for various operating variables.

Conflict of interest

The authors declare that they have no conflict

of interest.

References

1. Das NKr, Chaudhuri H, Bhandari RK, *et al.* Purification of helium from natural gas by pressure swing adsorption. *Current Science* 2008; 95(12): 1684–1687.
2. Bhushan J. Helium purification by gas adsorption method master of technology [MSc thesis]. Rourkela: National Institute of Technology; 2011.
3. Stoll AP, Taylor LG, Steel AJ. Helium purifiers. *Proceedings of the seventh international cryogenic engineering conference (ICEC7)*; 1978. p. 642–647.
4. Van Cleve E, Taborck P, Rutledge JE. Helium adsorption on lithium substrates. *Journal of Low Temperature Physics* 2008; 150: 1–11.
5. Martins D, Catarino I, Lopes D, *et al.* Low temperature adsorption versus pore size in activated carbons. *International Cryocooler Conference, Inc.*, Boulder, CO. 2011.
6. Majidia R, Ghanbarzadeh S, Jodaee asl N. Molecular dynamics simulation of helium adsorption on carbon nanocones with disclination angles of 240 ° and 300 °. *The 4th international conference on nanostructures (ICNS4)*; 2012.
7. Das NKr, Kumar P, Mallik C, *et al.* Development of a helium purification system using pressure swing adsorption. *Current Science* 2012; 103(6): 631–634.
8. Chang Hua, Wu Z, Yao M, *et al.* Experimental investigation and modeling of adsorption of carbon dioxide on 5A molecular sieve for helium purification of high-temperature gas-cooled reactor. *Energy Procedia* 2013; 39(9): 208–226.
9. Bartolomei M, Carmona-Novillo E, Hernández MI, *et al.* Graphdiyne pores: “Ad Hoc” openings for helium separation applications *The Journal of Physical Chemistry* 2014; 118(51): 29966–29972.
10. Ruthven DM. *Principle of adsorption and adsorption processes*. New York: John Wiley & Sons, Inc. 1984.
11. Mendes AMM, Costa AVC, Rodrigues AE. Analysis of nonisobaric steps in nonlinear bicomponent pressure swing adsorption systems. *Application to Air Separation Industrial & Engineering Chemistry Research* 2000; 39(1): 138–145.
12. Mendes AMM, Costa AVC, Rodrigues AE. Oxygen separation from Air by PSA: modeling and experimental results part I: Isothermal operation. *Separation and Purification Technology* 2001; 24(1): 173–188.
13. Milton RM (inventors). UNION CARBIDE CORP (assignee). Molecular sieve adsorbents. U.S. patent. 2,882,244. 1959 Apr.
14. Yang RT. *Adsorbents: Fundamentals and applications*. New Jersey: John Wiley & Sons, Inc.; 2003.
15. Ritter JA, Liu Y. Tapered pressure swing adsorption columns for simultaneous air purification and solvent vapor recovery. *Industrial & Engineering Chemistry Research* 1998; 37(7): 2783–2791.
16. Rege SU, Yang R, Qian K, *et al.*

- Air-prepurification by pressure swing adsorption using single/layered beds. *Chemical Engineering Science* 2001; 56(8): 2745–2759.
17. Mivechian A, Pakizeh M. Hydrogen recovery from Tehran refinery off-gas using pressure swing adsorption, gas absorption and membrane separation technologies: Simulation and economic evaluation. *Korean Journal of Chemical Engineering* 2013; 30(4): 937–948.
 18. Jang SC, Yang S, Oh SG, *et al.* Adsorption dynamics and effects of carbon to zeolite ratio of ordered beds for multi component gas adsorption. *Korean Journal of Chemical Engineering* 2011; 28(2): 583–590.
 19. Kim YH, Lee DG, Moon DK, *et al.* Effect of bed void volume on pressure vacuum swing adsorption for air separation. *Korean Journal of Chemical Engineering* 2014; 31(1): 132–141.
 20. Ruthven DM, Farooq S, Knaebel KS. *Pressure swing adsorption*. New York: VCH Publications Inc.; 1994.
 21. Teague KG, Edgar TF. Predictive dynamic model of a small pressure swing adsorption. *Industrial & Engineering Chemistry Research* 1999; 38(10): 3761–3775.
 22. Zaman M, Lee JH. Carbon capture from stationary power generation sources: A review of the current status of the technologies. *Korean Journal of Chemical Engineering* 2013; 30(8): 1497–1526.
 23. Hoshyargar V, Fadaei F, Ashrafizadeh SN. Mass transfer simulation of nanofiltration membranes for electrolyte solutions through generalized Maxwell-Stefan approach. *Korean Journal of Chemical Engineering* 2015; 32: 1388–1404.
 24. Grande CA. Advances in pressure swing adsorption for gas separation. *International Scholarly Research Notices Chemical Engineering* 2012; 1–13.
 25. Jee JG, Lee JS, Lee CH. Air separation by small-scale two-bed medical O₂ pressure swing adsorption. *Industrial & Engineering Chemistry Research* 2001; 40(16): 3647–3658.
 26. Chou CT, Chen L. Simulation of a four-bed pressure swing adsorption process for oxygen enrichment. *Industrial & Engineering Chemistry Research* 1994; 33(5): 1250–1258.
 27. Jee JG, Park HJ, Haam SJ, *et al.* Effects of nonisobaric steps and isobaric steps on O₂ pressure swing adsorption for an aerator. *Industrial & Engineering Chemistry Research* 2002; 41(17): 4383–4392.
 28. Jee JG, Lee SJ, Lee CH. Comparison of the adsorption dynamics of air on Zeolite 5A and carbon molecular sieve beds. *Korean Journal of Chemical Engineering* 2004; 21(6): 1183–192.
 29. Jee JG, Park MK, Yoo HK, *et al.* Adsorption and desorption characteristics of air on zeolite 5a, 10x, and 13x fixed beds. *Separation Science and Technology* 2002; 37(15): 3465–3490.
 30. Lee SJ, Jung JH, Moon JH, *et al.* Parametric study of the three-bed pressure-vacuum swing adsorption process for high purity O₂ generation from ambient air. *Industrial & Engineering Chemistry Research* 2007; 46(11): 3720–3728.
 31. Lin L. Numerical simulation of pressure swing adsorption process [MSc thesis]. Xi'an, China: Xidian University; 1990.
 32. Wilson SJ, Beh CCK, Webley PA, *et al.* The effects of a readily adsorbed trace component (water) in a bulk separation PSA process: The case of oxygen VSA. *Industrial & Engineering Chemistry Research* 2001; 40(12): 2702–2713.

ORIGINAL RESEARCH ARTICLE

Efficiency of single and mixed dimeric surfactants micelles on solubilization of polycyclic aromatic hydrocarbons

Naveen Kumar^{1*}, Rashmi Tyagi², V.K. Tyagi³

¹ Department of Chemistry, School of Basic and Applied Sciences, Shobhit University, Gangoh-247341, U.P., India.

E-mail: naveen.kumar@shobhituniversity.ac.in; naveenharsana@gmail.com

² Department of Chemical Engineering, Jaypee University of Engineering & Technology, Guna-473226, M.P., India.

³ Department of Oil & Paint Technology, Harcourt Butler Technological Institute, Kanpur-208002, U.P., India.

ABSTRACT

The solubilization of polycyclic aromatic hydrocarbons (PAHs) such as naphthalene, phenanthrene and pyrene by single and mixed anionic dimeric surfactants was investigated and correlated with micellar properties of these surfactants. The surface and micellar properties of single and binary mixed combinations of anionic dimeric surfactants have been studied through surface tension as well as conductivity measurements at 300 K. The associations between their micelle properties and solubilizing efficiency towards PAHs have been quantified and discussed in terms of the molar solubilization ratio (MSR), micelle-water partition coefficient (K_m) and standard free energy of solubilization (ΔG_s^0). The negative value of ΔG_s^0 exhibits spontaneously the solubilization process. The MSR values increase with the order “pyrene < phenanthrene < naphthalene”. The current study provides significant information for the selection of mixed dimeric surfactants for solubilizing water-insoluble compounds.

Keywords: Anionic Dimeric Surfactants; Polycyclic Aromatic Hydrocarbons; Solubilization

ARTICLE INFO

Received 17 January 2020
Accepted 12 March 2020
Available online 16 March 2020

COPYRIGHT

Copyright © 2020 Naveen Kumar, *et al.*
EnPress Publisher LLC. This work is licensed under the Creative Commons Attribution-NonCommercial 4.0 International License (CC BY-NC 4.0).
<http://creativecommons.org/licenses/by-nc/4.0/>

1. Introduction

The contamination of soil and water by hydrophobic organic compounds (HOCs) are a universally widespread environmental problem. HOCs are found in the priority list of hazardous substances as listed by the agency for toxic substances and disease registry of USA^[1]. Among these compounds, polycyclic aromatic hydrocarbons (PAHs) are more hazardous compounds to human health due to their mutagenic and carcinogenic nature^[2,3]. PAHs constitute a class of hazardous organic compounds consisting of two or more fused benzene rings in linear, angular or cluster arrangements. These hydrophobic pollutants are byproducts of the incomplete combustion of organic matter. The major sources of PAHs are the wastes from the combustion of fossil fuel, incineration of industrial waste and petroleum products viz., coal tar, crude oil, creosote, vehicle emissions, etc.^[4] These organic pollutants defile sea water, sediments and soil and also remain in the atmosphere for a long time due to their low solubility in water. Because of their higher hydrophobicity and poor solubility in water, the removal of PAHs from the contaminated sites becomes excessively difficult. Advancement of desorption and removal of these organics from soil is challenge to researchers and technologists.

It is well known that surfactants can enhance the aqueous solubility of hydrophobic compounds by incorporating them into the hydrophobic cores

of micelles. This process is called solubilization^[5]. Micelle-enhanced solubilization of hydrophobic compounds is clearly one of the primary applications of surfactants in liquid media. It has been reported that the solubility of PAH increases linearly with surfactant concentration above the critical micelle concentration (CMC)^[6-8]. However, most of the previous studies related to solubilizing of PAHs on the use of conventional surfactants having single monomers with a single hydrophobic tail and a single hydrophilic head group^[9,10]. A more modern and advanced surfactant to aid the removal of contaminants from soil dimeric surfactant, differently from conventional surfactant, dimeric surfactant consisting of two hydrophobic tails and two hydrophilic head groups connected by a spacer group^[11]. Their surface active properties are better to corresponding conventional surfactants with the same chain length. Therefore, they have much lower CMC values and are more capable in lowering the surface tension of water^[12]. Recently, dimeric surfactants were shown to be of great interest in industrial and scientific application due to their efficient solubilization capabilities^[13,14]. As the dimeric surfactants form larger micelles than the conventional surfactants, it should have a superior solubilizing capacity.

The specific objectives of the present study are to explain how partitioning of PAHs are influenced by the micelles of anionic dimeric surfactants and to have the idea about the synergistic solubilization by their equimolar mixed surfactant systems. In this study, we have studied water solubilization enhancement of three PAHs such as naphthalene, phenanthrene and pyrene, having different polarity by anionic dimeric surfactants (CADs, $s = 12$ and 16). The molar solubilization ratio (MSR), micelle-water partition coefficient (K_m) and standard free energy of solubilization (ΔG^0_s) towards PAHs have been determined.

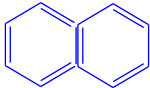
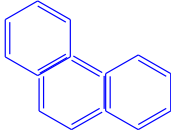
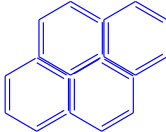
2. Experimental procedures

2.1 Materials

The anionic dimeric surfactants with carboxylate head group, CADs, were synthesized in our laboratory, according to our recently reported method^[15,16]. The molar ratio of reactants i.e., fatty

amine (N-methyldodecylamine or N-methylhexadecylamine) and EDTA dianhydride was 2:1 and the mixture was refluxed in methanol for 20 h at 50 °C. The purification and characterization of synthesized compound was done as discussed previously^[15]. Naphthalene (Naph), phenanthrene (Phen) and pyrene (Py) were used as polycyclic aromatic hydrocarbon in the present work and were also procured by sigma Aldrich. The formulas and aqueous properties of PAHs are listed in **Table 1**. Surfactant solutions were prepared in double distilled water.

Table 1. Showing water solubility of the selected PAHs^[17]

Compound	Molecular structure	Molecular weight (g/mol)	Water solubility at 25 °C (mg/L)
Naphthalene		128.2	34.4
Phenanthrene		178.2	1.0
Pyrene		202.3	0.16

2.2 Methods

2.2.1 Solubility measurements

The solubility measurement was similar to described elsewhere^[18]. The solubility of PAHs i.e., naphthalene, phenanthrene and pyrene, were measured in CADs solutions. Surfactant solutions were placed in 25 ml flasks at concentrations higher than CMC. An amount of each PAH in excess of its apparent solubility was added to each flask. Extra amount of PAHs was added to ensure maximum solubility in surfactant solution. These samples are then agitated on magnetic stirrer and allowed to stand for about 24 h. After this, the sample was collected and then centrifuged at 5000 rpm to settle down the excess amounts of PAHs. The determination of PAHs concentration was done by UV spectrophotometer (Elico SL 210). 1 ml of the supernatant surfactant solution taken and diluted to 10 ml in

flask with 1 ml methanol and rest with the corresponding surfactant-water solution. Naphthalene, phenanthrene and pyrene in the solutions were analyzed at the wavelengths of 220 nm, 254 nm and 334 nm, respectively. All experiments were performed at room temperature (22–26 °C).

2.2.2 Surface tension measurements

The CMC of the pure and mixed surfactant systems were determined by the surface tension measurement. The surface tension was determined using the Du Noüy tensiometer (Jencon, India) by the platinum ring detachment method. The tensiometer was calibrated through double-distilled water, and the platinum ring was perfectly cleaned and dried prior every observation. The surface tension values were measured until constant surface tension values indicated that equilibrium had been reached. The accuracy of the measurements was within $\pm 0.1 \text{ mNm}^{-1}$.

3. Results and discussion

3.1 CMC of the single and equimolar binary CADs surfactants

Solubilization is closely related to the solution properties of the surfactant micelles. Therefore, to better understand the solubilization power, we have studied the micellar properties of selected single dimeric surfactants and their equimolar mixtures. The CMC values of single as well as of binary surfactant mixtures (CAD₁₂₋₁₆) were examined on the basis of tensiometric measurements. Surface tension decreases as the concentration of the CADs increases. The CMC values of the single and binary surfactant systems are tabulated in **Table 2**, which were determined from the **Figure 1**. The CMC values of CAD₁₂ and CAD₁₆ were observed following order CAD₁₆ < CAD₁₂. The surfactant's chain length is main driving factor for micellization as well as hydrophobic interactions. As the hydrophobic chain length of dimeric surfactant increases, much water molecules are released, bringing about more entropy increase, and micellization of anionic dimeric with longer hydrophobic tail becomes at lower concentration.

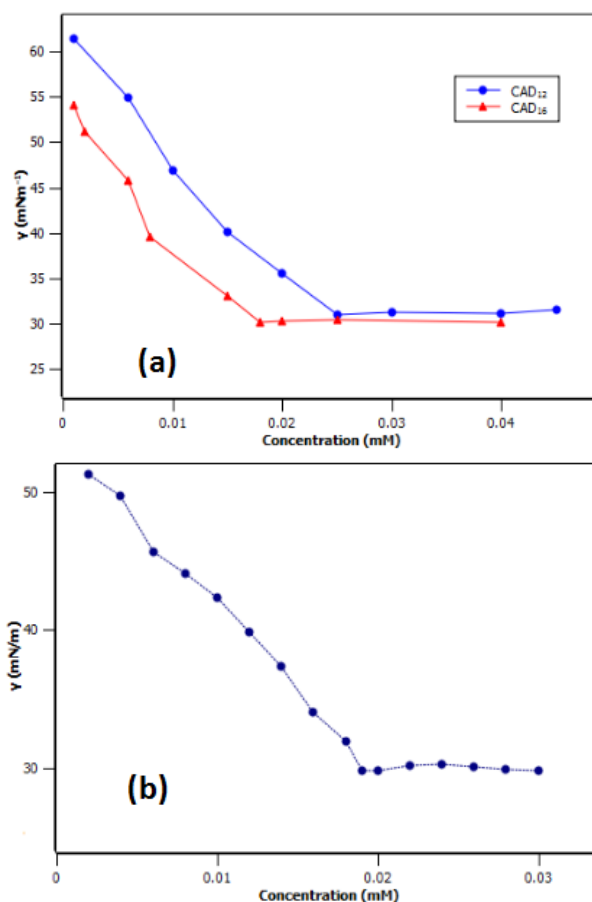


Figure 1. Plots of the surface tension (γ) vs. concentration of the single; CAD₁₂ and CAD₁₆ (a) and binary dimeric surfactant combinations; CAD₁₂₋₁₆ (b), at 25 °C.

Table 2. Micellization properties of single and mixed dimeric surfactant systems at 25 °C

Micellization parameters	CAD ₁₂	CAD ₁₆	CAD ₁₂₋₁₆
CMC _{exp} (mM)	0.025	0.018	0.021
CMC _{ideal} (mM)	-	-	0.019
γ_{cmc} (mN/M)	31.0	30.1	29.8
Π_{cmc} (mN/M)	41.0	41.9	42.2
$\Gamma_{cmc} \times 10^{10}$ (mol/cm ²)	4.09	4.67	4.71
A_{cmc} (nm ² × 10 ² /molecule)	40.6	35.6	36.1

3.2 Interfacial parameters

Various surface properties such as, surface excess or adsorption (Γ_{cmc}), occupied area per molecule (A_{cmc}) and surface pressure at the CMC (Π_{cmc}) of individual as well as equimolar binary surfactant systems were determined, which is given in **Table 2**. The adsorption efficacy of selected surfactants and their mixtures at the air/solution interface were calculated by Gibbs equation^[19].

$$\Gamma_{cmc} = (-1/2.303nRT)(d\gamma/d\log C)_T \quad (1)$$

where R and T are the ideal gas constant and tem-

perature, respectively, and n is a constant, which depends on the number of species constituting the surfactant. Γ_{cmc} values were used to calculate the minimum area per surfactant molecule (A_{cmc}) at the air/water interface using the equation^[19]:

$$A_{cmc} = 1 / N_A \Gamma_{cmc} \quad (2)$$

Where, N_A is Avogadro's number. The values of the surface pressure at the CMC (Π_{cmc}) were determined from the following equation^[19]:

$$\Pi_{cmc} = \gamma_0 - \gamma_{cmc} \quad (3)$$

Where, γ_0 and γ_{cmc} are the surface tension of the solvent and surface tension of the mixture at the CMC, respectively.

3.3. Interaction of the mixed micelles systems

For the equimolar binary mixed solutions, the interactions between the surfactant molecules (synergism or antagonism) can be explained by various parameters and equations. For ideal mixing of dimeric surfactants system, the ideal CMC value was calculated using the Clint equation^[20].

$$\frac{1}{c_i} = \frac{\alpha}{c_1} + \frac{(1-\alpha)}{c_2} \quad (4)$$

Where, C_1 and C_2 are the CMC and the mole fraction of component 1 and 2 in mixed surfactant systems and α stands for the stoichiometric molar fraction. **Table 2** indicates that obtained CMC values (CMC_{exp}) was lower than ideal CMC values (CMC_{ideal}), as signified in the formation of mixed micelles, which demonstrate a negative deviation with respect to ideal mixture for binary mixed systems. It is expressed that the mixing effect of CADs surfactant system is more reliable than expected in the ideal state due to the two tails of dimeric surfactant allowing the micellar molecules even more hydrophobic.

3.4. Solubilization of PAHs by individual and mixed dimeric surfactants

Prior to measure the solubilization power of binary mixtures of CADs, single systems were first studied to understand the efficiency of anionic dimeric surfactants. Plots for the variations of solubility of PHAs with concentration of single dimer-

ics CAD_{12} and CAD_{16} are shown in **Figure 2** and **3**. All the figures show that with the increasing of concentration of CADs, concentration of dissolved PHAs is also increasing, or solubility increases with the increasing concentrations of dimerics above the CMC. This phenomenon demonstrates that solubilization is closely associated to micellization.

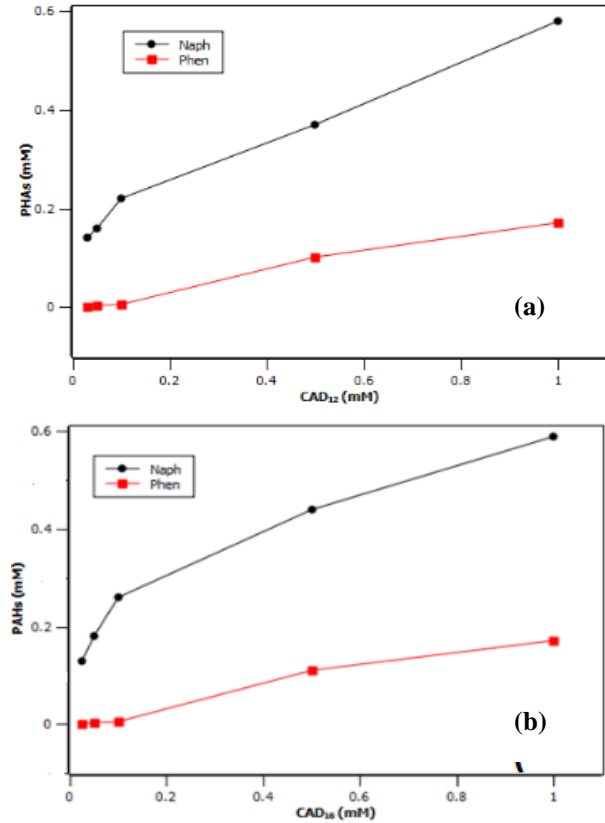


Figure 2. Variation of the solubility of PHAs with surfactant concentration CAD_{12} (a) and CAD_{16} (b).

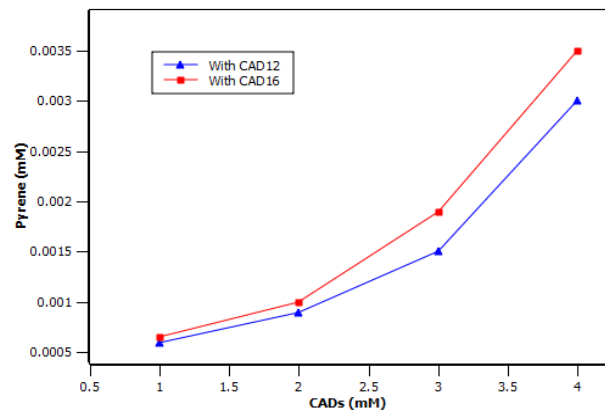


Figure 3. Variation of the solubility of pyrene with surfactant concentration CAD_{12} (■) and CAD_{16} (▲).

Therefore, water solubility of selected PHAs by equimolar binary mixed systems of CAD_{12-16} was further to be determined. The apparent solubility of PHAs increases linearly with

equimolar binary mixed surfactant combinations (**Figure 4** and **5**). This process showing the formation of mixed micelles and their potential ability to increase the solubility of PHAs in water.

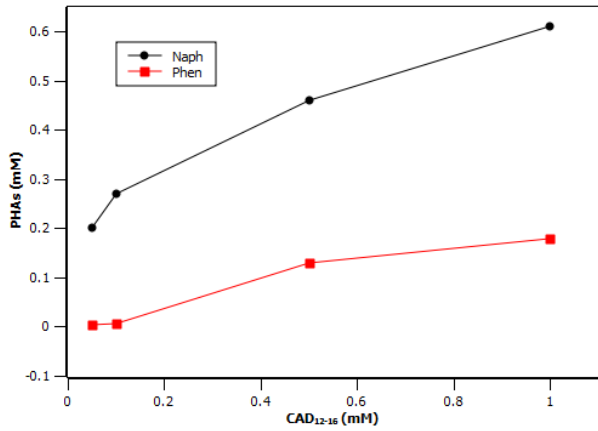


Figure 4. Solubilization of PAHs in CAD₁₂₋₁₆ mixed surfactants.

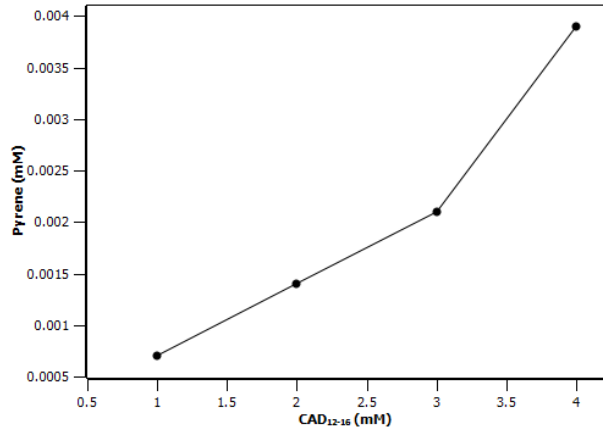


Figure 5. Solubility of pyrene with CAD₁₂₋₁₆ mixed surfactants.

To measure the effectiveness of CADs in solubilizing, molar solubilization ratio (MSR) has been determined. The MSR is characterized as the number of moles of compound solubilized by 1 mol of micellized surfactant, which is given by Edwards *et al.*^[21] and Wei J *et al.*^[18].

$$MSR = \frac{S_{ac} - S_{cmc}}{C_{ac} - CMC} \quad (5)$$

where, S_{ac} is the apparent solubility of a PAH compound at the surfactant concentration greater than the CMC; C_{ac} is the surfactant concentration, at which S_{ac} is measured; and S_{cmc} is the PAH solubility at the CMC. The MSR may be obtained from the slope of the variation of solubilize concentration against surfactant concentration and obtained values are listed in **Table 3**.

In addition to MSR, the effectiveness of solu-

bilization, the partition coefficient K_m was also calculated, which is defined as distribution of the mole fraction of PAHs between surfactant micelles and the aqueous phase has been obtained as following^[21]:

$$K_m = \frac{S_{ac} - S_{cmc}}{(C_{ac} - CMC + S_{ac} - S_{cmc})(V_w S_{cmc})} \quad (6)$$

where, V_w is the molar volume of water (1.8×10^{-2} l/mol at 25 °C^[21]).

Table 3. Molar solubilization ratios (MSR) of PHAs in individual and mixed surfactant systems at room temperature

Surfactant system	MSR		
	Naph	Phen	Py
CAD ₁₂	0.027	0.018	0.0006
CAD ₁₆	0.035	0.028	0.0007
CAD ₁₂₋₁₆	0.031	0.021	0.00067

Thus, an expression for K_m can be rearranged by substituting MSR to produce:

$$K_m = \frac{55.4 \times MSR}{S_{cmc}(1 + MSR)} \quad (7)$$

From the thermodynamic point of view, solubilization behavior of binary surfactant systems can be measured by the standard free energy of solubilization (ΔG_S^0) calculated by the following equation^[22]. The obtained values of K_m and ΔG_S^0 are given in **Table 4**.

$$\Delta G_S^0 = -RT \ln K_m \quad (8)$$

Table 4. log K_m and in equimolar mixed dimeric surfactants

(8) PAHs	log K_m	(kJ/mol)
Naph	5.46	-31.21
Phen	5.38	-29.87
Py	4.49	-25.61

4. Conclusion

Water solubility enhancements of PAHs in single anionic dimeric and their equimolar binary mixed systems have been measured. The associations between their micelle properties and solubilizing efficiency single and binary surfactant systems for naphthalene, phenanthrene and pyrene are expressed in terms of MSR and other parameters. The MSR values increase with the order “pyrene < phenanthrene < naphthalene”. The current study gives significant information for the selection of mixed dimeric surfactants for solubilizing water-insoluble compounds. The experimental results

of this study will be useful to know the solubilization properties of mixed anionic dimeric surfactant systems and significant to provide statistical proof for exploring novel surfactant systems for practical soil and water remediation.

Conflict of interest

The authors declare that they have no conflict of interest.

References

1. Zhang Y, Maier WJ, Miller RM. Effect of rhamnolipids on the dissolution, bioavailability, and biodegradation of phenanthrene. *Environmental Science & Technology* 1997; 31(8): 2211–2217.
2. Khan S, Cao Q. Human health risk due to consumption of vegetables contaminated with carcinogenic polycyclic aromatic hydrocarbons. *Journal of soil & sediments* 2012; 12(2): 178–184.
3. Yu H, Huang G, Wei J, *et al.* Solubilization of mixed polycyclic aromatic hydrocarbons through a rhamnolipid biosurfactant. *Journal of Environmental Quality* 2011; 40(2): 477–483.
4. Menzie CA, Potocki BB, Santodonato J, *et al.* Exposure to carcinogenic PAHs in the environment. *Environmental Science & Technology* 1992; 26(7): 1278–1284.
5. Tongcumpou C, Acosta E, Quencer LB, *et al.* Microemulsion formation and detergency with oily soils: II. Detergency formulation and performance. *Journal of Surfactants and Detergents* 2003; 6(3): 205–214.
6. Zhu L, Zhao B, Li Z. Water solubility enhancements of PAHs by sodium castor oil sulfonate microemulsions. *Journal of Environmental Science* 2003; 15(5): 583–589.
7. Chun C, Lee J, Park JW. Solubilization of PAH mixtures by three different anionic surfactants. *Environmental Pollution* 2002; 118(3): 307–313.
8. Rao KJ, Paria S. Solubilization of naphthalene in the presence of plant-synthetic mixed surfactant systems. *Journal of Physical Chemistry B* 2009; 113(2): 474–481.
9. Zhu L, Feng S. Synergistic solubilization of polycyclic aromatic hydrocarbons by mixed anionic-nonionic surfactants. *Chemosphere* 2003; 53: 459–467.
10. Aoudia M, Al-Haddabi B, Al-Harhi Z, *et al.* Sodium Lauryl ether sulfate micellization and water solubility enhancement towards naphthalene and pyrene: Effect of the degree of ethoxylation. *Journal of Surfactants and Detergents* 2010; 13: 103–111.
11. Menger FM, Littau CA. Gemini-surfactants: Synthesis and properties. *Journal of the American Chemical Society* 1991; 113(4): 1451–1454.
12. Zana R. *Novel surfactants*. New York: Marcel Dekker, Inc.; 1998.
13. Kumar N, Tyagi R. Industrial applications of dimeric surfactants: A review. *Journal of Dispersion Science & Technology* 2014; 35 (2): 205–214.
14. Kumar N, Tyagi R. Dimeric surfactants: promising ingredients of cosmetics and toiletries. *Cosmetics* 2013; 1: 3–13.
15. Kumar N, Tyagi R. Synthesis of anionic carboxylate dimeric surfactants and their interactions with electrolytes. *Journal of Taibah University for Science* 2015; 9(1): 69–74.
16. Kumar N, Tyagi R. Synthesis and surface studies of anionic gemini surfactant in the different counter-ions. *International Journal of Industrial Chemistry* 2015; 6: 59–66.
17. Verschuere K. *Handbook of environmental data on organic chemicals*. 3rd ed. In: Van Nostrand R (editor). New York: Van Nostrand Reinhold; 1996.
18. Wei J, Huang G, Yu H, *et al.* Efficiency of single and mixed Gemini/conventional micelles on solubilization of phenanthrene. *Chemical Engineering Journal* 2011; 168(1): 201–207.
19. Rosen MJ. *Surfactants and interfacial phenomena*. 3rd ed. New York: John Wiley & Sons; 2004.
20. Clint JH. Micellization of mixed nonionic surface active agents. *Journal of the Chemical Society Faraday Transactions* 1975; 171: 1327–1334.
21. Edwards DA, Luthy RG, Pittsburgh PA. Solubilization of polycyclic aromatic hydrocarbons in micellar nonionic surfactant solutions. *Environmental Science & Technology* 1991; 25: 127–133.
22. Rangel-Yagui CO, Hsu HWL, Pessoa-Jr A, *et al.* Micellar solubilization of ibuprofen: influence of surfactant head groups on the extent of solubilization. *Revista Brasileira de Ciências Farmacêuticas* 2005; 41(2): 237–246.

ORIGINAL RESEARCH ARTICLE

Heavy metal-induced oxidative stress and DNA damage as shown by RAPD-PCR in leaves of *Elodea canadensis*

Dilek Demirezen Yilmaz^{1*}, Nuri Ercan², Fahriye Sumer Ercan³

¹Faculty of Science, Department of Biology, Erciyes University, Kayseri, Turkey. E-mail: demirez@erciyes.edu.tr

²Faculty of Agriculture, Ahi Evran University, Kırşehir, Turkey.

³Faculty of Architecture and Engineering, Department of Genetic and Bioengineering, Ahi Evran University, Kırşehir, Turkey.

ABSTRACT

The objective of the study was to evaluate the antioxidant response and DNA damage of heavy metals (Cd, Cu and Cr) in *Elodea canadensis*. Superoxide dismutase (SOD), catalase (CAT), Glutathione reductase (GR) and lipid peroxidation levels of leaves of *Elodea canadensis* which was exposed to different concentrations of heavy metals (Cd: 2, 5, 10, 15, 25 ppb; Cu: 200, 500, 1000, 2500 ppb and Cr: 1, 3, 10, 15, 25 ppb) in a hydroponic culture were determined spectrophotometrically. The highest induction in SOD and CAT activities were determined at highest concentration of heavy metals. The Random Amplified Polymorphic DNA Polymerase Chain Reaction (RAPD-PCR) technique was used to investigate the variation of DNA banding patterns of samples that exposed to different concentrations of heavy metals. Changing in band intensity and the gain and loss of bands were demonstrated the genotoxic effect of heavy metals. Bioaccumulation, oxidative responses and DNA damages were shown that *Elodea canadensis* represents a useful bioindicator.

Keywords: *Elodea Canadensis*; Oxidative Stress; DNA Damage; RAPD-PCR

ARTICLE INFO

Received 6 March 2020
Accepted 29 April 2020
Available online 4 May 2020

COPYRIGHT

Copyright © 2020 Dilek Demirezen Yilmaz, et al.
EnPress Publisher LLC. This work is licensed under the Creative Commons Attribution-NonCommercial 4.0 International License (CC BY-NC 4.0).
<https://creativecommons.org/licenses/by-nc/4.0/>

1. Introduction

Metals form one of the major groups of genotoxic environmental pollutants for soil and aquatic ecosystems. These dangerous pollutants usually originate from industry and agricultural activities like pesticides and fertilizers. The toxic effect of heavy metals in plants and animals has been investigated by many researchers^[1-3]. Heavy metal originated phytotoxicity often related to production of reactive oxygen species (ROS) in plants and potentially toxic that compared with molecular oxygen^[4].

The metal's molecular damaging action is not clearly known, but studies suggested that the oxidative damage is caused by metal toxicity^[5]. There are several cellular stress responses and damages in cellular components like membranes, proteins and DNA. Comet, micronucleus and chromosome aberration assays have been used to measure the genotoxic effect of heavy metals on plants in many studies^[6-8].

The advances in molecular biology provide the development of sensitive and useful techniques for DNA analysis in ecotoxicology. Random Amplified Polymorphic DNA (RAPD) is a DNA-based technique and used to detect the differences of DNA fingerprints from control and exposed DNA to a genotoxic effects. DNA damaging agents such as heavy metals and UV radiation in plants induce genomic DNA alterations and

RAPD-PCR can be successfully applied to determine these alterations^[9].

The advantage of DNA-based techniques is especially related to sensitivity and short response time of these techniques. RAPD-PCR is also used for species classification, genetic mapping and phylogeny studies. Nowadays, it is known that a novel biomarker assay for the detection of DNA damages and mutations like rearrangements, point mutation, insert or deletions of DNA in many living things has been carried out^[10,11]. RAPD fragments are detected by agarose gel electrophoresis and changing in band intensity, and the gain and loss of bands are demonstrated the genotoxic effect of damaging agents.

Heavy metal contamination as a result of natural or anthropogenic activities is a serious problem in the world^[12]. The accumulation of these heavy metals in plants causes many physiological and biochemical changes^[13]. These pollutants cause production of ROS that can cause important harm to plant cell structures. To overcome the oxidative damage, plants have advanced a common network of antioxidant enzymes, such as superoxide dismutase (SOD, EC 1.15.1.1), catalase (CAT, EC 1.11.1.6), peroxidase (POD, EC 1.11.1.7)^[14].

The objectives of the present study were to investigate DNA damage induced by different heavy metals in *Elodea canadensis* and changes in antioxidants levels.

2. Materials and methods

2.1 Genomic DNA isolation, RAPD amplification method and estimate of genomic template stability

DNA extraction was performed by using CTAB method^[15]. The concentration of extracted DNAs was measured at 260 nm and the purity was evaluated by the ratio of OD₂₆₀/OD₂₈₀ with a spectrophotometer (ACTGene Micro-Spectrophotometer). The A₂₆₀/A₂₈₀ ratio demonstrates the DNA purity, and 1.8–2.0 values suggest “pure DNA”.

Amplification of both nuclear DNA that extracted by CTAB method was performed using 2 µl of DNA template in a 15 µl reaction that

contains PCR buffer 1.5 µl (10X buffer with (NH₄)₂ SO₄, Thermo Fisher), MgCl₂ (2.5 mM, Thermo Fisher) 1.2 µl, dNTP (10 mM stock solution) 0.5 µl, BSA (10 mg/mL) 0.6 µl, primers (10µM, Opc) 1.0 µl, Taq Polymerase (5 u/µl, Thermo Fisher) 0.25 µl and filled up with sterile deionized water to the final volume.

The temperature profile for the RAPD-PCR was initially denaturing at 94 °C for 2.5 min, followed by 36 cycles at 94 °C for 45 s (denaturation), 35 °C for 45 s (annealing) and 72 °C for 2 min (extension), with final extension at 72 °C for 10 min. PCR products were electrophoresed in a Tris-Asedic Acid-EDTA (TAE) buffer by 2% agarose gel for 1.5 h at 80V. DNAs were stained with ethidium bromide and the bands were photographed under UV light. 100 bp DNA ladder was used as a standard marker.

Primer screening for RAPD-PCR was performed using 10 primers. Five out of 10 primers gave polymorphic bands. The sequences of these oligomers were given in **Table 1**. Polymorphism that observed in RAPD profiles contained disappearance of a control band and appearance of a new band. The amplification reactions were repeated at least three times to get reproducible results.

Genomic template stability (GTS; %) was calculated as following:

$$GTS = (1 - a/n) \times 100$$

where “a” was the average number of RAPD polymorphic profiles detected in each samples treated and “n” the number of total bands found in the control. The polymorphism that observed in RAPD banding profiles included the disappearance of a normal band and appearances of a new band in comparison with the control. The average polymorphism was calculated for each experimental group exposed to different doses of different heavy metals (Cd, Cu and Cr). For comparing the sensitivity of each parameter, changes occurring in these values were calculated as a percentage of its control (set to 100%).

2.2 Plant material, growth conditions and heavy metal estimation

Fresh samples of *E. canadensis* were obtained from ponds in Kayseri, Turkey. Plants were grown in a growth chamber at 25 ± 1 °C during 16/8 light/dark cycle with $350 \mu\text{mol m}^{-2} \text{s}^{-1}$ of irradiance by cold fluorescent lamps. The plants were grown in Hoagland nutrient solution and the solution was renewed every four days. The solution pH was maintained to 5.8 ± 0.1 by titration with NaOH or HCl solutions (0.1 M) when required. On the 7th day, heavy metal treated plants were harvested from containers. The plants were rinsed twice with distilled water and subsequently, biochemical parameters were determined. Dried samples of plant were digested with 10 mL of concentrated HNO₃, using a CEM microwave digestion system. After digestion, the volume of each sample was adjusted to 25 mL using double deionized water^[16]. Determination of the cadmium, chromium and copper concentrations in all samples was carried out by inductively coupled plasma optical emission spectrometry (Varian). The samples were analyzed in triplicate.

2.3 Estimation of lipid peroxidation (MDA)

Lipid peroxidation level was estimated according to the method of Razinger *et al.*^[17], with modifications.

2.4 Antioxidative enzymes

2.4.1 Enzyme extraction

Fresh tissue (0.2 g) was homogenized with 5 mL of 100 mM potassium phosphate buffer (pH 7.0) containing 0.1 mM EDTA and 1% (w/v) polyvinylpyrrolidone in an ice-cooled mortar. Homogenate was centrifuged at 15000 g for 15 min at 4 °C^[18]. The supernatant was used for enzyme determination.

2.4.2 Superoxide dismutase (EC 1.15.1.11)

The SOD activity (EC 1.15.1.11) was analyzed by measuring the inhibition of the photochemical reduction of nitrobluetetrazolium (NBT)^[19]. The assay mixture contained 20 mM phosphate buffer (pH 7.5), 10 mM methionine, 0.1mM NBT, 0.1 mM EDTA, 0.005 riboflavin, $50 \mu\text{g mL}^{-1}$ of enzyme extract and 0.25 mL of

deionized H₂O in a total volume of 3 mL. Riboflavin was added at the end, and the tubes were shaken and then illuminated for 15 min. The absorbance was recorded at 560 nm and the absorbance of the non-irradiated reaction mixture served as a control. Inhibition of 50% of the reaction was defined as one unit of enzyme and the enzyme activity was expressed as nU g⁻¹ FW.

2.4.3 Catalase (EC 1.11.1.6)

CAT (EC 1.11.1.6) activity was measured spectrophotometrically by following the consumption of H₂O₂ at 240 nm, according to Aebi^[20], in potassium phosphate buffer (150 mM, pH 7) containing 15 mM H₂O₂ and enzyme extract (exactly 50 mg of protein) in a final volume of 1 mL. Addition of H₂O₂ started the reaction.

3. Results

3.1 Effects of heavy metals on RAPD profiles

Among the 10 decamer oligonucleotide primers evaluated, only 5 of them presented specific and stable results (**Table 1**). The RAPD fingerprints revealed the occurrence of significant differences between untreated and treated plant materials, with apparent changes in the number, size and the intensity of amplified DNA fragments. The primary observation of RAPD banding patterns generated by the heavy metals exposed plants were the differences in the band intensities, appearance of new bands or absence of normal bands compared with control plants. RAPD banding patterns generated by heavy metal exposed plant materials were different from those obtained control. Different polymorphic bands were determined at each concentration of heavy metals for different primers. GTS did not decrease gradually.

Table 1. Random primers that gave polymorphic bands in RAPD-PCR

RAPD primer	Sequences of primers (5'→3')	GC%
Opc 2	GTG AGG CGT	70
Opc 5	GAT GAC CGC	70
Opc 8	TGG ACC GGT	70
Opc 9	CTC ACC GTC	70
Opc 15	GAC GGA TCA	60

The number of disappearing RAPD bands was greater at 5 ppb and 25 ppb Cd for Opc 5 and Opc 9, respectively. Maximum number of extra bands appeared with Cu application at 500 and 1000 ppb concentrations in total. The decrease in band intensity was only apparent for *Elodea*

exposed to 500 ppb Cu but in Cd treated plant it was observed for different doses. However, the increase in band intensity was clearly obvious for Cd, Cu and Cr treatments especially for Opc 5 primer (Table 2, 3, 4).

Table 2. Changes of total bands in control, and of polymorphic bands and varied bands in *E. canadensis* exposed to different concentrations of Cd

Primers	Cd concentration (ppb)																								
	0				2				5				10				15				25				
	a	b	c	d	a	b	c	d	a	b	c	d	a	b	c	d	a	b	c	d	a	b	c	d	
Opc 2	5	0	0	0	2	0	0	3	0	0	0	0	2	1	0	0	0	1	0	0	0	1	0	0	0
Opc 5	7	2	0	0	2	0	3	3	0	0	0	1	0	0	0	0	3	4	0	0	0	4	0	0	0
Opc 8	3	0	0	0	1	0	2	0	0	0	0	0	1	0	0	0	0	1	1	2	0	1	1	2	0
Opc 9	6	0	0	0	0	0	0	0	0	0	0	0	0	0	0	0	0	0	3	0	0	0	3	0	0
Opc 15	7	0	0	2	2	0	0	0	2	0	0	0	2	0	0	0	1	1	0	2	1	1	0	2	1
Total bands	28	2	0	2	7	0	5	6	2	0	0	1	5	1	0	0	4	7	4	4	1	7	4	4	1
a + b		2				5				0				1				11				11			
a + b + c + d		11				13				6				5				16				16			

Note: a: indicates appearance of new bands; b: disappearance of normal bands; c: decrease in band intensities; and d: increase in band intensities; a + b: denotes polymorphic bands; and a + b + c + d: varied band.

Table 3. Changes of total bands in control, and of polymorphic bands and varied bands in *E. canadensis* exposed to different concentrations of Cu

Primers	Cu concentration (ppb)																								
	0				200				500				1000				1500				2500				
	a	b	c	d	a	b	c	d	a	b	c	d	a	b	c	d	a	b	c	d	a	b	c	d	
Opc 2	5	0	0	0	2	2	0	0	2	2	0	0	2	3	0	0	2	3	0	0	2	3	0	0	2
Opc 5	7	1	0	0	6	2	0	1	1	2	0	0	0	3	0	0	0	3	0	0	0	3	0	0	0
Opc 8	3	2	0	0	1	4	0	0	0	4	0	0	0	1	0	0	1	1	0	0	1	1	0	0	1
Opc 9	6	1	0	0	5	0	0	0	0	0	0	0	0	0	0	0	4	0	0	0	4	0	0	0	4
Opc 15	7	0	0	0	2	0	2	0	2	0	0	0	5	0	0	0	4	0	0	0	3	0	0	0	3
Total bands	28	4	0	0	16	8	2	1	5	8	0	0	7	7	0	0	11	7	0	0	10	7	0	0	10
a + b		4				10				8				7				7				7			
a + b + c + d		20				16				15				18				17				17			

Note: a: indicates appearance of new bands; b: disappearance of normal bands; c: decrease in band intensities; and d: increase in band intensities; a + b: denotes polymorphic bands; and a + b + c + d: varied band.

Table 4. Changes of total bands in control, and of polymorphic bands and varied bands in *E. canadensis* exposed to different concentrations of Cr

Primers	Cr concentration (ppb)																								
	0				1				3				10				25				50				
	a	b	c	d	a	b	c	d	a	b	c	d	a	b	c	d	a	b	c	d	a	b	c	d	
Opc 2	5	0	0	0	1	0	0	0	3	0	0	0	2	0	0	0	3	1	2	1	0	1	2	1	0
Opc 5	7	2	5	0	1	1	0	0	5	1	0	0	2	1	0	0	2	2	4	0	1	2	4	0	1
Opc 8	3	2	0	1	0	2	0	0	1	4	0	0	2	2	0	1	2	3	1	1	1	3	1	1	1
Opc 9	6	0	0	0	3	0	0	0	3	0	3	0	2	0	4	0	0	0	6	0	0	0	6	0	0
Opc 15	7	0	4	0	1	0	4	0	1	0	4	0	1	0	0	1	3	0	4	2	0	0	4	2	0
Total bands	28	4	9	1	6	3	4	0	13	5	7	0	9	3	4	2	10	6	17	4	2	6	17	4	2
a + b		13				7				12				7				23				23			
a + b + c + d		20				20				21				19				29				29			

Note: a: indicates appearance of new bands; b: disappearance of normal bands; c: decrease in band intensities; and d: increase in band intensities; a + b: denotes polymorphic bands; and a + b + c + d: varied band.

Finally, it was defined that maximum number of extra bands appeared with Opc 5 at 25 ppb Cd (four new bands), Opc 8 at 500 and 1000 ppb Cu (four new bands) and Opc 8 at 10 ppb Cr (four new bands). The extra bands that appeared

were determined to be of maximum 1100 bp molecular size (Figure 1). The occurrence of polymorphism was due to the loss and/or gain of the bands in the treated plant with heavy metals in comparison with the control. The highest

polymorphism was obtained from Cr application

with 82% at 50 ppm concentration.

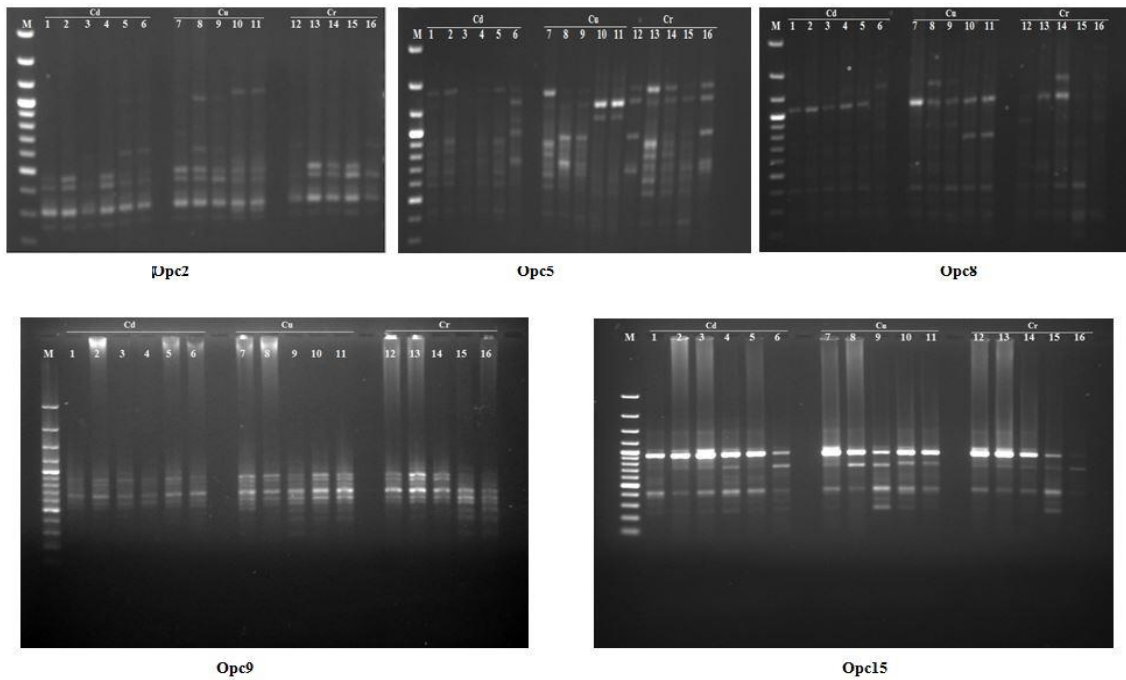


Figure 1. RAPD profiles of genomic DNA from *E. canadensis* exposed to varying heavy metal concentrations with different primers. (M: DNA marker; 1: Control; 2–16: increasing doses of heavy metal treatments).

3.2 Heavy metal contents

The results related to the accumulation of Cd, Cr and Cu in *E. canadensis* are presented in **Figure 2a, 2b** and **2c**. The maximum Cd accumulation was found to be 0.47 ppm DW at 15 ppb Cd. On prolonged exposure to higher concentrations of Cd (25 ppb), there was a significant decline in the Cd accumulation rate. According to **Figure 2b**, the higher Cr accumulation was obtained from 25 ppb Cr application (0.049 ppm) and the differences in all treatments were significant for *E. canadensis*. Similarly, the maximum Cu accumulation was found to be 6.8 ppm at 2500 ppb. The analysis of one-way ANOVA showed that the differences in all the treatments were significant ($P < 0.05$).

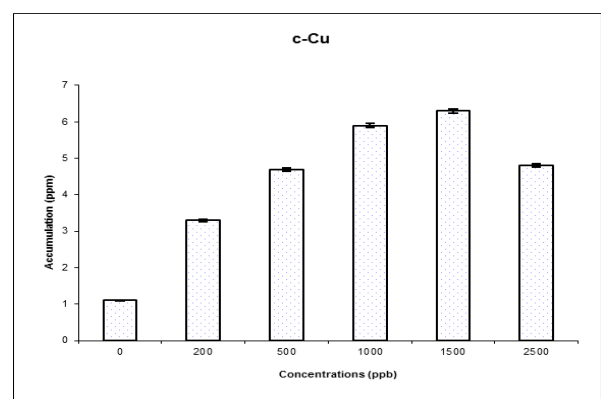
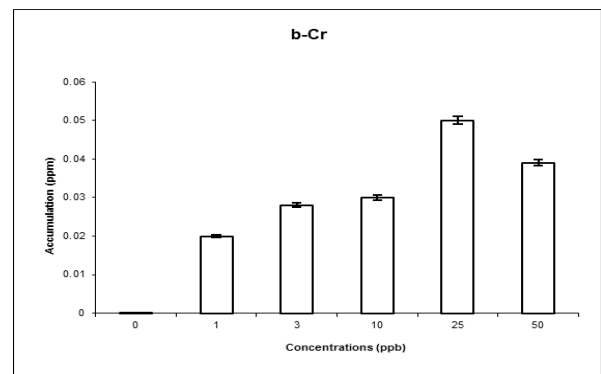
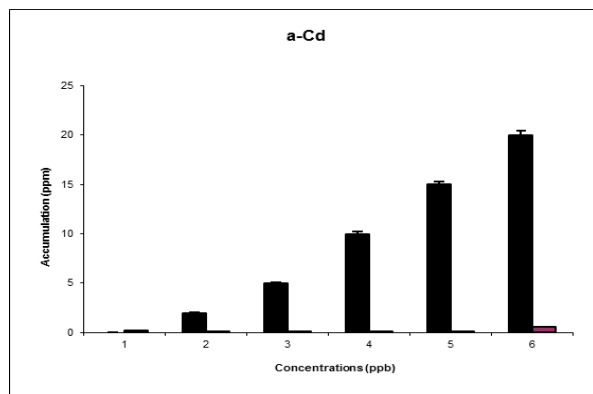


Figure 2. Heavy metal accumulation in *E. canadensis*.

3.3 Effect of heavy metals on the level of MDA

The effect of Cd, Cu and Cr on MDA concentration is presented in **Figure 3a, b** and **c**. In the experiments, increasing in MDA

concentration in *E. canadensis* was observed. MDA concentration was linearly with increased heavy metal levels in the solution. The analysis of one way ANOVA showed that the differences of all treatments were significant ($P < 0.05$) for plant.

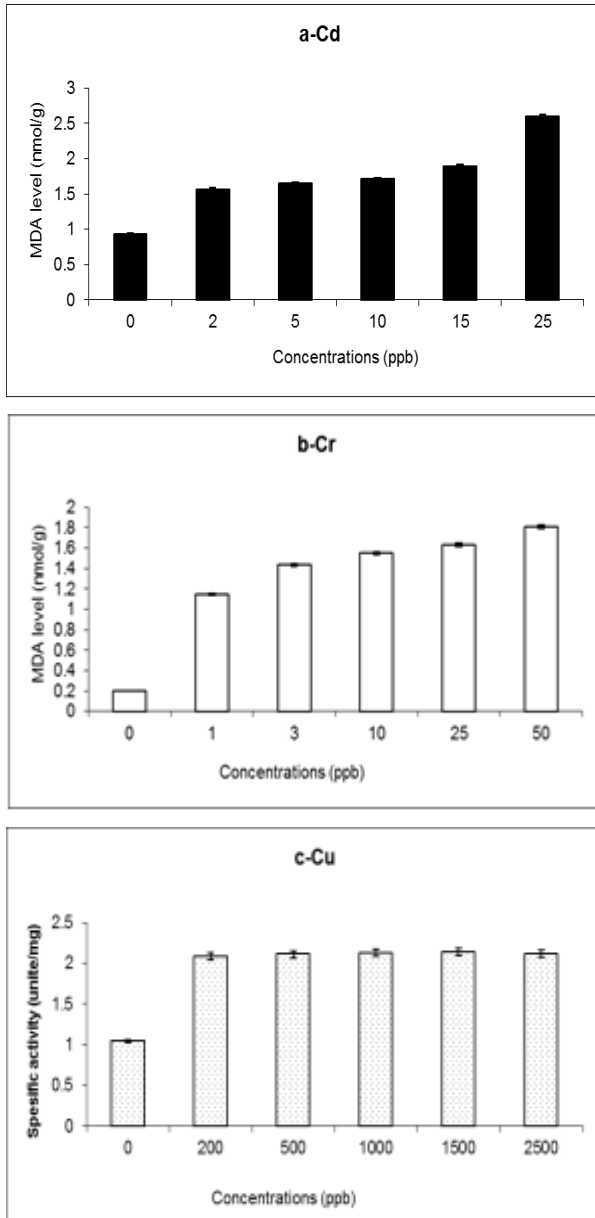


Figure 3. MDA activities in *E.canadensis* upon Cd (a), Cr (b) and Cu (c) exposures. Values represent mean \pm S.E. ($n = 3$). Asterisks indicate significant differences at $P < 0.05$.

3.4 Effects of heavy metals on SOD and CAT activity

In this study, the decline in catalase activity was observed with the increasing concentration of Cd in *E. canadensis*. The highest concentration of Cd (15 ppb) proved to be extremely toxic declining CAT activity (Figure 4a). Plants exposed to Cd present significant differences ($P <$

0.05). Similarly, the highest concentration of Cu (1500–2500 ppb) and Cr (25 and 50 ppb) proved to be toxic declining CAT activity (Figure 4b and c).

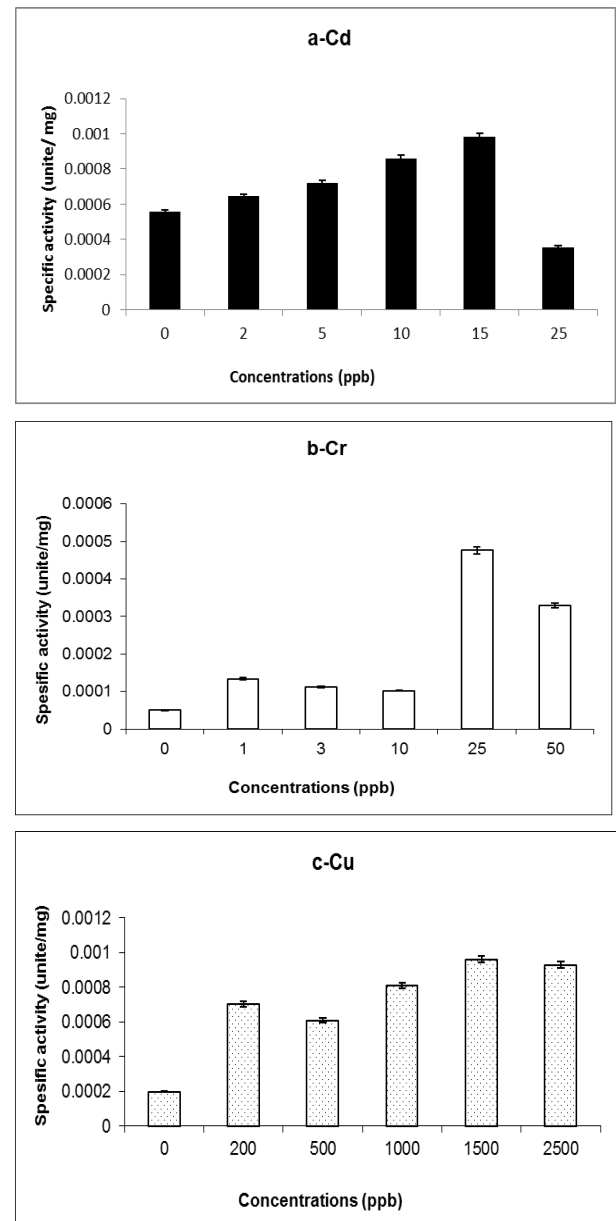


Figure 4. CAT activities in *E.canadensis* upon Cd (a), Cr (b) and Cu (c) exposures. Values represent mean \pm S.E. ($n = 3$). Asterisks indicate significant differences at $P < 0.05$.

Figure 5 a–c indicated that SOD activity increased linearly with increasing heavy metal levels. The maximum SOD activity was recorded at 25 ppb Cd ($1.19 \pm 0.0085 \text{ U mg}^{-1}$). Results showed that, at the highest concentration of Cd, the SOD accumulation increases. Additionally, the significant differences were found in SOD activity among the treatments. At 1500 ppb Cu ($2.261 \pm 0.0075 \text{ U mg}^{-1}$), the maximum SOD

activity was recorded. At the highest concentration of Cu, the SOD accumulation increases. Additionally, the significant differences were found in SOD activity among the treatments. Similarly, SOD activity increased linearly with increasing Cr levels in *E. canadensis*.

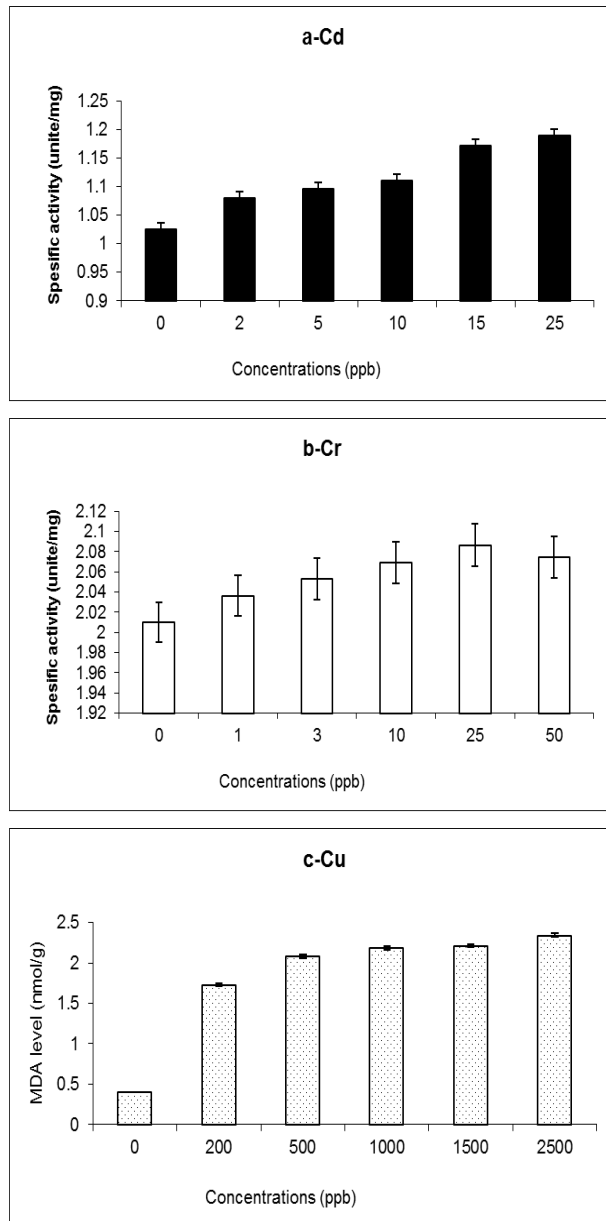


Figure 5. SOD activities in *E. canadensis* upon Cd (a), Cr (b) and Cu (c) exposures. Values represent mean \pm S.E. (n = 3). Asterisks indicate significant differences at $P < 0.05$.

4. Discussion

Heavy metals induce some cellular stress responses and damages of cellular components like DNA, proteins and membranes. RAPD-PCR is a selective and sensitive technique for DNA analysis in ecogenotoxicological studies. DNA

fingerprints can be used to show the differences between samples that exposed and nonexposed to genotoxic agents^[21]. This technique gives evidence about DNA mutation that treated to any genotoxic agents like heavy metals.

Number of bands, product yield and clarity of the banding profiles are used for detection of polymorphism. Appearance or disappearance of bands is probably to be due to the changes in primers sites. This is likely caused by rearrangements, point mutations and DNA damages in the primer binding sites^[22].

Five primers, Opc 2, Opc 5, Opc 8, Opc 9 and Opc 15, produced unique bands in *E. canadensis* that treated with different heavy metals (Cd, Cu, and Cr) in the present study. These bands can be used as a marker for detection of genotoxic effect of heavy metals on *E. canadensis*. The low doses of heavy metals, especially Cd, were tolerable and polymorphism rate was comparatively low. Many researchers have used RAPD-PCR to evaluate metal toxicity changes in genetic patterns between treated and non-treated samples^[21,23,24].

Our results showed that maximum number of polymorphic bands obtained from Cr with the highest concentration of heavy metal. In Cd application, the largest number of new bands was obtained with the highest dose of heavy metal similarly with Cr application. Cd has been reported by many researchers to cause DNA damages, such as single and double-strand breaks, modified bases, a basic site, DNA-protein cross-links, oxidized bases etc., in many organisms^[3,25-27]. These structural changes after heavy metal treatment can significantly affect the PCR events and new PCR products can be occurred because of changing in priming sites.

RAPD technique can be successfully used to determine the DNA damages in living things. Although this technique is a qualitative method, RAPD analysis can be used as a sensitive method for environmental toxicology and useful biomarker system for an early warning. The present results suggest that RAPD-PCR in conjunction with antioxidant enzyme analysis can prove a powerful ecotoxicological tool.

In the present study, *E. canadensis* were grown in hydroponic culture in the presence of increasing Cd, Cu and Cr concentrations to evaluate its possible defense mechanisms. The results obtained indicated that at highest levels Cd, Cu and Cr were toxic to *E. canadensis*. The level of malondialdehyde (MDA) content has been considered as an indicator of oxidative stress that shows that plants are under high-level antioxidant stress.

In the experiments, MDA concentration increased linearly with increased heavy metal levels in the solution. Similar results were obtained with duckweed species by Uruç Parlak and Demirezen Yılmaz^[16]. Gupta *et al.*^[28] stated that higher MDA content shows the oxidative stress and this maybe one of the potential mechanisms by which toxicity due to heavy metals is manifested in plant tissues. Plants under environmental stresses, such as drought and heavy metals, their production of ROS production will increase^[29].

The increased activity of antioxidative enzymes in a plant indicated the formation of ROS and the present study indicated the generation of oxidative stress in *L. gibba* since all studied enzymes activity increased at high heavy metal levels^[30]. In other words, *E. canadensis* analyzed in this work contains high Cd, Cr and Cu concentrations sufficient to activate ROS production and then oxidative stress.

Superoxide dismutase, the first enzyme in the detoxifying process, converts superoxide radicals to H₂O₂ at a very fast rate. The enhanced SOD activity observed in the present study is consistent with studies in which other plant species were treated with heavy metals^[31]. The effect of heavy metal stress on SOD expression is likely to be governed by the tissue and sub cellular sites, at which oxidative stress is generated as supported by the higher activity of SOD in roots than in leaves of metal stressed plants^[18].

Our data showed significant increases in CAT activity were observed between the treatments. The results obtained indicated that CAT activity decreased linearly with increasing Cd, Cu and Cr levels. Contrary to our results, a

decline in the specific activity of catalase with increase in Cr concentration (20–80 ppm, 0.5 mM) has been reported by Shankar *et al.*^[32]. According to Willekens *et al.*^[33], it is likely that excess production of ROS by heavy metals can inactivate CAT probably by inactivating enzyme-bound heme group. These inconsistent results of differences in the plant organs were studied, and the durations and concentrations of metals were utilized.

5. Conclusion

Considering these results, we strongly suggest that higher heavy metal levels may cause oxidative stress in *E. canadensis* cells and may cause membrane damage through production of ROS and interferes with chlorophyll metabolism. Therefore, the data shown here can be used to illustrate how *E. canadensis* responds to its stressful environment. Among the antioxidative enzymes, SOD and CAT appear to play key roles in the plant's antioxidative defense mechanism under heavy metal toxicity. The ability of *E. canadensis* to both accumulate and tolerate moderate heavy metal level used in this study could be partly derived from ROS detoxification through an efficient antioxidant system.

Conflict of interest

The authors declare that they have no conflict of interest.

References

1. Dixit V, Pandey V, Shyam R. Differential antioxidative responses to cadmium in roots and leaves of pea (*Pisum sativum* L. cv. Azad). *Journal of Experimental Botany* 2001; 52(358): 1101–1109.
2. Verma S, Dubey SR. Lead toxicity induces lipid peroxidation and alters the activities of antioxidant enzymes in growing rice plants. *Plant Science* 2003; 164(4): 645–655.
3. Jimi S, Uchiyama M, Takaki A, *et al.* Mechanism of cell death induced by cadmium and arsenic. *Annals of the New York Academy of Sciences* 2004; 1011: 325–331.
4. Mithofer A, Schulze B, Boland W. Biotic and heavy metal stress response in plants: Evidence for common signals. *FEBS Letters* 2004; 566: 1–5.
5. Ganesh KS, Baskaran L, Rajasekaran S, *et al.* Chromium stress induced alterations in

- biochemical and enzyme metabolism in aquatic and terrestrial plants. *Colloids and Surfaces Bointerfaces* 2008; 63: 159–163.
6. Steinkellner H, Kassie F, Knasmueller S. *Tradescantia* micronucleus assay for the assessment of the clastogenicity of Austrian water. *Mutation Research* 1999; 426: 113–116.
 7. Angelis JK, McGuffie M, Menke M, *et al.* Adaptation to alkylation damage in DNA measured by the comet assay. *Environmental and Molecular Mutagenesis* 2000; 36(2):146–150.
 8. Labra M, Grassi F, Imazio S, *et al.* Genetic and DNA-methylation changes induced by potassium dichromate in *Brassica napus* L. *Chemosphere* 2004; 54: 1049–1058.
 9. Atienzar FA, Cordi B, Donkin MB, *et al.* Comparison of ultraviolet-induced genotoxicity detected by random amplified polymorphic DNA with chlorophyll fluorescence and growth in a marine macroalgae, *Palmaria palmate*. *Aquatic Toxicology* 2000; 50(1-2): 1–12.
 10. Savva D. DNA fingerprinting as a biomarker assay in ecotoxicology. *Toxicology and Ecotoxicology News* 1996; 3: 110–114.
 11. Savva D. Use of DNA fingerprinting to detect genotoxic effects. *Ecotoxicology and Environmental Safety* 1998; 41(1): 103–106.
 12. Shikazono N, Zakir HM, Sudo Y. Zinc contamination in river water and sediments at Taisyu Zn–Pb mine area, Tsushima Island, Japan. *Journal of Geochemical Exploration* 2008; 98(3): 80–88.
 13. Pavlikov ĀD, Pavlik M, Staszkov ĀL, *et al.* Glutamate kinase as a potential biomarker of heavy metal stress in plants. *Ecotoxicology and Environmental Safety* 2008; 70(2): 223–230.
 14. Khan NA. Abiotic Stress and Plant Responses. In: Singh S (editor). New Delhi: IK International; 2008.
 15. Rogers SO, Bendich AJ. Extraction of DNA from milligram amounts of fresh, herbarium and mummified plant tissues. *Plant Molecular Biology* 1985; 5: 69–76. Available from: <https://doi.org/10.1007/BF00020088>.
 16. Parlak KU, Yilmaz DD. Response of antioxidant defences to Zn stress in three duckweed species. *Ecotoxicology and Environmental Safety* 2012; 85(1): 52–58.
 17. Razinger J, Dermastia M, Koce JD, *et al.* Oxidative stress in duckweed (*Lemna minor* L.) caused by short-term cadmium exposure. *Environmental Pollution* 2008; 153(3): 687–694.
 18. Hou W, Chen X, Song G, *et al.* Effect of copper and cadmium on heavy metal polluted water body restoration by duckweed (*Lemna minor*). *Plant Physiology and Biochemistry* 2007; 45(1): 62–69.
 19. Beauchamp C, Fridovich I. Superoxide dismutase: Improved assays and an assay applicable to acrylamide gels. *Analytical Biochemistry* 1971; 44(1): 276–287.
 20. Aebi H. Catalase in vitro. *Methods in Enzymology* 1984; 105: 121–176.
 21. Enan MR. Application of random amplified polymorphic DNA (RAPD) to detect the genotoxic effect of heavy metals. *Biotechnology and Applied Biochemistry* 2006; 43(3): 147–154.
 22. Liu W, Yang Y, Li P, *et al.* Risk assessment of cadmium contaminated soil on plant DNA damage using RAPD and physiological indices. *Journal of Hazardous Materials* 2009; 161: 878–883.
 23. Conte C, Mutti I, Puglisi P, *et al.* DNA fingerprinting analysis by a PCR based method for monitoring the genotoxic effects of heavy metals pollution. *Chemosphere* 1998; 37: 2739–2749.
 24. Liu W, Li P, Qi X, *et al.* DNA changes in barley (*Hordeum vulgare*) seedlings induced by cadmium pollution using RAPD analysis. *Chemosphere* 2005; 61: 158–167.
 25. Aust AE, Eveleigh JF. Mechanism of DNA oxidation. *Proceedings of the Society for Experimental Biology and Medicine* 1999; 222(3): 246–252.
 26. Bišová K, Hendrychová J, Cepák V, *et al.* Cell growth and division processes are differentially sensitive to cadmium in *Scenedesmus quadricauda*. *Folia Microbiol* 2003; 48(6): 805–816.
 27. Ates I, Suzen HS, Aydın A, Karakaya A. The oxidative DNA base damage in tests of rats after intraperitoneal cadmium injection. *Biometals* 2004; 17(4): 371–377.
 28. Gupta DK, Nicoloso FT, Schetinger MRC, *et al.* Antioxidant defence mechanism in hydroponically grown *Zea mays* seedlings under moderate lead stress. *Journal of Hazardous Materials*; 172(1): 479–484.
 29. Mittler R. Oxidative stress, antioxidants and stress tolerance. *Trends in Plant Science* 2002; 7(9): 405–410.
 30. Yilmaz DD, Parlak KU. Changes in proline accumulation and antioxidative enzyme activities in *Groenlandia densa* under cadmium stress. *Ecological Indicators* 2011; 11(2): 417–423.
 31. Sharma P, Dubey RS. Involvement of oxidative stress and role of antioxidative defense system in growing rice seedlings exposed to toxic concentrations of aluminum. *Plant Cell Reports* 2007; 26: 2027–2038. Available from: <https://doi.org/10.1007/s00299-007-0416-6>.
 32. Shankar AK, Cervantes C, Loza-Tavera H, *et al.* Chromium toxicity in plants. *Environment International* 2005; 31(5): 739–753.
 33. Willekens H, Chamnongpol S, Davey M, *et al.* Catalase is a sink for H₂O₂ and is indispensable for stress defence in C3 plants. *The EMBO Journal* 1997; 16(16): 4806–4816. doi: 10.1093/emboj/16.16.4806.

ORIGINAL RESEARCH ARTICLE

Iron removal from ground water using Egyptian cost-effective clay minerals

H.M. Abdel-Ghafar^{1*}, E.A. Abdel-Aal¹, B. E. El Anadouli²

¹Central Metallurgical Research and Development Institute (CMRDI), P.O. Box: 87 Cairo, Egypt. E-mail: hamdy.maamoun@yahoo.com

²Faculty of Science, Cairo Universities, Cairo, Egypt.

ABSTRACT

Glaucanite and kaolin are used as adsorbent materials for iron removal from synthetic solutions. Different concentrations of iron solutions have been prepared (10, 20 and 30 mg/L). Different dose of glauconite and kaolin were added (0.1, 0.55 and 1.0 g). Statistical design was used to determine the optimum conditions of iron adsorption on glauconite and kaolin. It is shown that glauconite has high adsorption for iron reaching to 95% while kaolin has lower adsorption for iron. Physical and chemical characterization of glauconite and kaolin was tested. High surface area of glauconite (19.8 m²/g) compared to kaolin (5.4 m²/g) explains its high removal efficiency.

Keywords: Glauconite; Kaolin; Iron; Statistical Design; Box-Behnken

ARTICLE INFO

Received 13 March 2020
Accepted 5 May 2020
Available online 9 May 2020

COPYRIGHT

Copyright © 2020 H.M. Abdel-Ghafar, *et al.*
EnPress Publisher LLC. This work is licensed under the Creative Commons Attribution-NonCommercial 4.0 International License (CC BY-NC 4.0).
<http://creativecommons.org/licenses/by-nc/4.0/>

1. Introduction

Glaucanite and kaolin clays are extremely fine particles exhibiting chemical properties of colloids^[1,2]. The high specific surface area, chemical and mechanical stability, layered structure, and high cation exchange capacity (CEC) made these clays excellent adsorbent materials^[3]. Because of their small particle size, the specific surface area (external and internal) of clays and clay minerals could be increased to few hundreds m²/g. Natural clays like glauconite and kaolin acquire prominence as low-cost adsorbents over the last few decades due to their abundance and its capability to undergo modification to enhance the surface area and adsorption capacity^[4].

Ground water and some water from the bottom anoxic zones of reservoirs often contain iron and manganese ions or their complexes with natural organic matter^[5,6]. In conventional treatment, the oxidation of iron and manganese was carried out using various oxidants such as oxygen, chlorine, ozone, or potassium permanganate. The chemistry of oxidation becomes complicated when background species such as phosphate and fulvic acid are involved, so that the oxidation of ferrous ion, that can be normally readily oxidized, is retarded^[7].

It was reported that, heavy metals such as arsenic, cadmium, copper, cobalt, chromium, nickel, iron, and zinc, exist in variable contents in drinking water as well as in ground water^[8,9]. This makes the removal of these toxic contaminants from water sources, efficiently and within reasonable costs, an important issue. Many adsorption materials have been investigated for the removal of heavy metal ions from water. Sorbents that have been studied include natural and artificial materials such as clay minerals^[10-15], carbon-nanomaterials^[16-19], biosorbents^[20], and micro/nano-structured metal

oxides^[20–28].

In this research, adsorption of iron ions on glauconite and kaolin minerals was studied. In Egypt, ground water of New Valley area contains higher contents of iron ions above the acceptable limit. The concentrations of iron ions in New Valley ground waters are ranged from low to moderate. Baharia oasis area in Egypt is rich with glauconite, and Klabsha, Aswan and Sinai areas in Egypt have a huge amount of kaolin. So, glauconite and kaolin can be used as cost-effective clay minerals for iron removal from ground water.

2. Experimental procedures

2.1 Materials

Glauconite was obtained from New-Vally area, Egypt. Kaolin was obtained from Aswan area, Egypt. Samples were crushed, grounded, sieved to –150+200 mesh size, and dried at 105 °C. Samples of natural glauconite and kaolin analysis are given in **Table 1**. A stock solution of ferrous ions (1000 mg/L Fe²⁺) is prepared by dissolution of ferrous sulfate heptahydrae (Sigma-Aldrich chemicals, Germany) with distilled water. Then, different concentrations ferrous ions were prepared by diluting certain volume of stock solution with distilled water. All chemicals used were of analytical grade.

Table 1. Chemical analysis for natural glauconite and kaolin

Elements		Glauconite	Kaolin
SiO ₂	(%)	39.0	51.6
Al ₂ O ₃	(%)	23.50	29.7
K ₂ O	(%)	3.50	0.48
Fe ₂ O ₃	(%)	23.88	2.48
CaO	(%)	0.04	0.27
TiO ₂	(%)	----	0.14
P ₂ O ₅	(%)	0.37	0.54
MnO	(%)	0.05	0.75
Cl	(%)	0.20	----
SO ₃	(%)	1.52	0.09
L.O.	(%)	7.05	13.54

2.2 Methods

Experimental Statistical Design-Expert 9.0.3, Stat-Ease, Inc., MN, USA, software was used in this paper: 17 runs were carried out by applying the experimental Box-Behnken statistical design with three levels and three variables as shown in **Table 2** and **3**. Each run was done independently while

glauconite and kaolin dose varied according to the design.

Aliquots of Fe (II) solutions of known concentration were put into the glass bottles (100 mL) containing accurately weighted amounts of the adsorbent. After the required adsorption time, iron ions concentration was determined by atomic absorption flame emission spectrophotometer (AA-6200 Shimadzu).

Table 2. Codec factor variables

Variables	Levels		
	0	+1	-1
Time (min)	35	60	10
Concentration (mg/L)	20	30	10
Dose (g)	0.55	1.0	0.1

Table 3. Experimental Box-Behnken design with three levels and three variables applied in adsorption experiments

Run No.	Codec factor levels		
	Time	Concentration	Dose
1	-1	+1	0
2	0	-1	-1
3	+1	0	+1
4	+1	-1	0
5	-1	0	-1
6	-1	-1	0
7	0	0	0
8	0	-1	+1
9	0	0	0
10	0	+1	+1
11	0	0	0
12	0	0	0
13	0	0	0
14	-1	0	+1
15	0	+1	-1
16	+1	0	-1
17	+1	+1	0

2.3 Cation exchange capacity (CEC)^[29]

25.0 g of clay sample was added to a 500 mL Erlenmeyer flask, and then 125 mL of 1 M NH₄OAc was added with shaking thoroughly and allowed standing 16 hours. After standing, filtrate the sample then, wash and rinse with eight separate addition of 95% ethanol to remove excess saturating solution. Extract the adsorbed NH₄ by leaching the sample with eight separate 25 mL additions of 1 M KCl. Discard the clay sample and transfer the leachate to a 250 mL volumetric. Dilute to volume with additional KCl. The concentration of NH₄-N in the KCl extract was determined by spectrophotom-

eter (spectro UV-2650, LABOMED, USA).

2.4 Morphology analysis

In order to know the reason of highly effective removal of iron with glauconite, structure sight should be analyzed. Scanning electron microscope (SEM) was employed to visualize sample morphology. In the present work, the glauconite sample was analyzed by this technique using SEM to study the surface morphology of glauconite sample.

2.5 Statistical analysis

Box-Behnken design was used for statistical experimental design^[30] to study the interactions and analyze the effects of studied parameters on the iron ions adsorption efficiency at glauconite and kaolin.

According to this design, the optimal conditions were estimated using a second order polynomial function by which correlations between studied parameters (time, concentration & dose) and response (adsorption efficiency, %) were established. The general form of this equation is:

$$Y = \beta_0 + \beta_1X_1 + \beta_2X_2 + \beta_3X_3 + \beta_{12}X_1X_2 + \beta_{13}X_1X_3 + \beta_{23}X_2X_3 + \beta_{11}X_1^2 + \beta_{22}X_2^2 + \beta_{33}X_3^2 \quad (1)$$

where Y is the predicted response; X₁, X₂ and X₃ are the studied variables; β₁, β₂, β₃,... are equation constants and coefficients. Software package, Design-Expert 9.0.3, Stat-Ease, Inc., MN, USA, was used for regression analysis of experimental data and to plot response surface contours.

3. Results and discussion

3.1 Characterization of glauconite and kaolin

Some chemical and physical properties of glauconite and kaolin are presented in **Table 1** and **Table 4**. The glauconite sample has a specific surface area of 19.8 m²/g while kaolin of 5.4 m²/g. Also, CEC of glauconite was 28 meq/100 g and kaolin was 11 meq/100 g.

Table 4. Physical properties of glauconite and kaolin

Parameters	Value	
	Glauconite	Kaolin
Specific surface area (m ² /g)	19.8	5.4
CEC (meq/100 g)	28	11
Porous volume (cm ³ /g)	0.264	0.315
Particle size (µm)	80–100	80–100

3.2 Statistical analysis of variance Fe (II) adsorption

Adsorption results of iron ions on glauconite and kaolin are given in **Table 5**. The adsorption efficiency (%) onto glauconite was varied from 14.8% to 95.3% (Run numbers 5 and 8). More than 95% Fe (II) removal with contact time 35 minutes, iron load 10 mg/L and 1.0 g of glauconite. Actually, these results of glauconite are highly promised if it is compared with Electro-coagulation method which gives removal efficiency of Fe (II) 95–99% with high cost (Approx. 6.05 \$/m³)^[31] while clay adsorption of glauconite and kaolin is not expensive because these ores has low price (24–39 \$ per ton of clay)^[32]. In spite of the design conditions of iron ions adsorption efficiency (%) onto kaolin varied from 1.1 to 44% (Run numbers. 16 and 8) where it's noticed the weak adsorption compared to glauconite, it is still more economic in use than other techniques like electro-coagulation method and adsorption with activated carbon^[31].

Table 5. Results of Fe (II) adsorption on the surface of glauconite & kaolin

Run no.	Time (min)	Concentration (mg/L)	Dose (g)	Adsorption (%)	
				Glauconite	Kaolin
1	10	30	0.55	48.7	2.4
2	35	10	0.10	64.6	19.6
3	60	20	1.00	95.2	23.7
4	60	10	0.55	94.0	20.4
5	10	20	0.10	14.8	9.4
6	10	10	0.55	62.0	32.7
7	35	20	0.55	84.5	10.5
8	35	10	1.00	95.3	44.0
9	35	20	0.55	84.5	10.3
10	35	30	1.00	73.0	3.6
11	35	20	0.55	84.5	10.6
12	35	20	0.55	84.8	10.5
13	35	20	0.55	84.5	10.4
14	10	20	1.00	45.3	14.7
15	35	30	0.10	28.6	1.1
16	60	20	0.10	45.8	8.2
17	60	30	0.55	92.2	2.9

Statistical results of analysis of variance of Fe (II) adsorption on the surface of glauconite & kaolin are given in **Table 6**. The time of adsorption and adsorbent dose are the most significant factors while the concentration of adsorbate is less significant. The obtained correlation coefficient (R²) of the models was 0.94, which indicates a good predictability of the models. It is noticed that, for kaolin, the

concentration of adsorption is the most significant while the time of adsorption and adsorption dose are less significant. The obtained correlation coefficient (R^2) of the models was 0.92, which indicates a good predictability of the models.

centration (R^2) of the models was 0.92, which indicates a good predictability of the models.

Table 6. Analysis of variance of Fe (II) adsorption on the surface of glauconite & kaolin

Source	Sum of Squares		Mean Square		F-Value		p-value (Prob > F)	
	Glauconite	Kaolin	Glauconite	Kaolin	Glauconite	Kaolin	Glauconite	Kaolin
Model	9632.7	1896.4	1070.3	316.1	31.1	18.7	< 0.0001	< 0.0001
A (Time)	3059.6	2.0	3059.6	2.0	89.1	0.1	< 0.0001	0.7383
B (Concentration)	673.5	1423.1	673.5	1423.1	19.6	83.9	0.0031	< 0.0001
C (Dose)	3005.1	284.4	3005.1	284.4	87.4	16.8	< 0.0001	0.0022
AB	33.1	40.9	33.1	40.9	0.9	2.4	0.3594	0.1511
AC	89.8	26.0	89.8	26.1	2.6	1.5	0.1501	0.2437
BC	46.9	119.9	46.9	119.9	1.4	7.1	0.2809	0.0239
A²	664.9	---	664.9	---	19.3	---	0.0032	---
B²	27.8	---	27.8	---	0.8	---	0.3981	---
C²	1931.2	---	1931.2	---	56.2	---	0.0001	---

The correlation between adsorption efficiency (%) and process factors (time, concentration and dose) can be shown as a final equations (2) and (3) in terms of the actual factors for glauconite and kaolin, respectively.

$$\text{Adsorption} = +84.22 + 19.56 * A - 9.18 * B + 19.38 * C + 2.88 * AB + 4.74 * AC + 3.42 * BC - 12.75 * A^2 + 12.57 * B^2 - 21.42 * C^2 \quad (2)$$

$$\text{Adsorption} = + 33.85 - 0.4 * A - 1.11 * B + 29.65 * C + 0.01 * AB + 0.23 * AC - 1.22 * BC \quad (3)$$

Where, A is the time of adsorption (min), B is the concentration of ferrous ions (mg/L) and C is the glauconite or kaolin dose (g per 100 mL solution).

These equations are highly significant because they represent the net results of statistical application input data, so by known any adsorption parameters of time, concentration and glauconite or kaolin dose, by applied directly in equation (2) or (3), output results will be adsorption efficiency (%).

3.3 Interaction of the studied parameters

3.3.1 Effects of adsorption time and Fe (II) ions concentrations on adsorption efficiency

Effects of adsorption time and Fe (II) ions concentrations on adsorption efficiency at doses (0.55 g per 100 mL solution) for glauconite and kaolin are given in **Figure 1**.

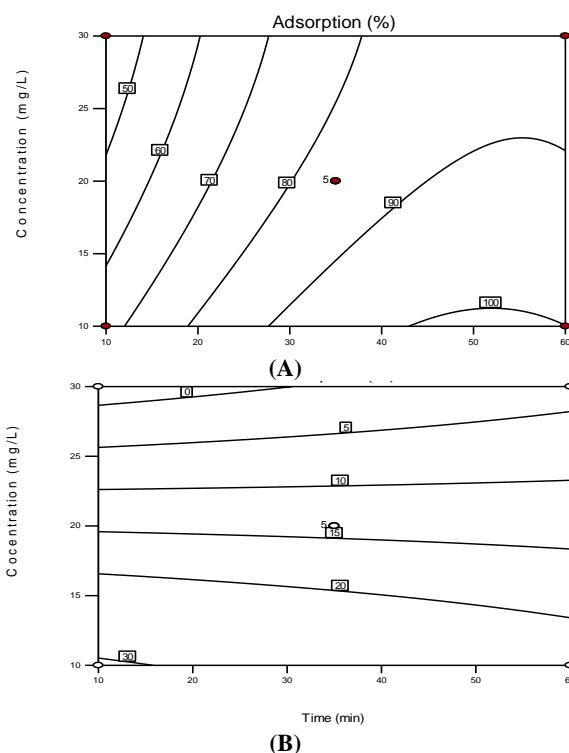


Figure 1. Effect of adsorption time and Fe (II) concentration on adsorption efficiency at dose = 0.55 g of glauconite (A) & kaolin (B).

The adsorption efficiency of Fe (II) onto glauconite and kaolin increased by increasing adsorption time at all the glauconite and kaolin doses studied.

With addition 0.55 g of glauconite dose, the adsorption efficiency increased from 60–70% to 100% with increasing adsorption time from 10 to 60 minutes at low Fe (II) concentration of 10 mg/L (**Figure 1A**). At high Fe (II) concentration of 30

mg/L and also with 0.55 g of glauconite dose, the adsorption efficiency increased from 40–50% to 80–90% with increasing adsorption time from 10 to 60 minutes (**Figure 1A**). While, with addition of 0.55 g of kaolin, the adsorption efficiency increased up to 30% with increasing adsorption time from 10 to 60 minutes and decreasing Fe (II) concentration from 30 to 10 mg/L (**Figure 1B**).

3.3.2 Effects of adsorption time and glauconite dose on adsorption efficiency

Effects of adsorption time and dose of glauconite and kaolin on adsorption efficiency at Fe (II) ions concentration (10 mg/L) are given in **Figure 2**. The adsorption efficiency of Fe (II) onto glauconite increases by increasing adsorption time.

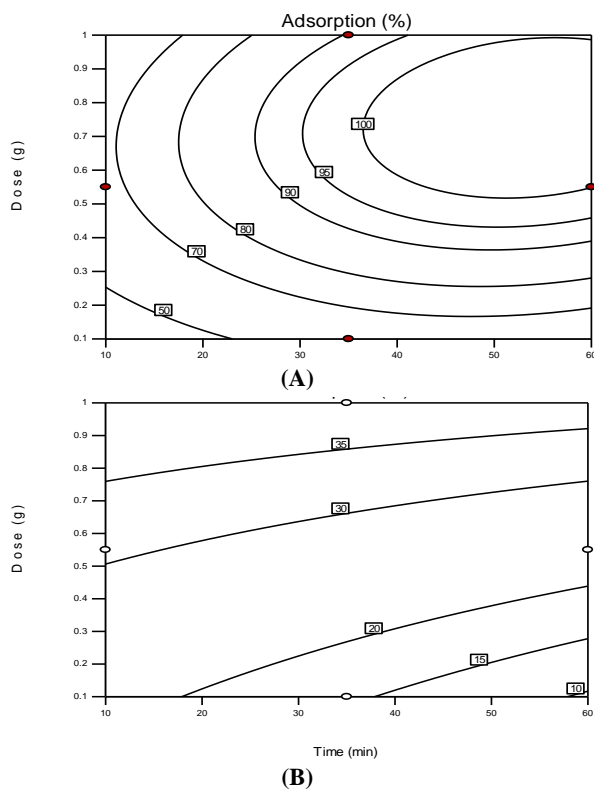


Figure 2. Effect of adsorption time and glauconite (A) & Kaolin (B) dose on adsorption efficiency at 10 mg/L concentration of Fe (II).

The results reveal that with 0.1 g of glauconite dose, the adsorption efficiency increases from 40–50% to 60–70% with increasing adsorption time from 10 to 60 minutes at low Fe (II) concentration of 10 mg/L (**Figure 2A**).

However, at high glauconite dose of 1.0 g and at low Fe (II) concentration of 10 mg/L, the adsorption efficiency increased from 60–70% to about 100% with increasing adsorption time from 10 to 60

minutes (**Figure 2A**).

Whereas, the effect of interaction of two factors, the time of adsorption and kaolin dose on adsorption efficiency at Fe (II) ions concentration (10 mg/L) were shown in **Figure 2B**. It can be observed that beyond the adsorption time of 10 minutes, the adsorption efficiency increased slowly from 10 to 35% with increasing time of adsorption from 10 to 60 minutes and the dose of kaolin increasing from 0.1 to 1.0 g (**Figure 2B**).

3.3.3 Effects of Fe (II) ions concentrations and kaolin doses on adsorption

Effects of Fe (II) ions concentrations and doses of glauconite and kaolin on adsorption efficiency at adsorption time (60 minutes) are given in **Figure 3**.

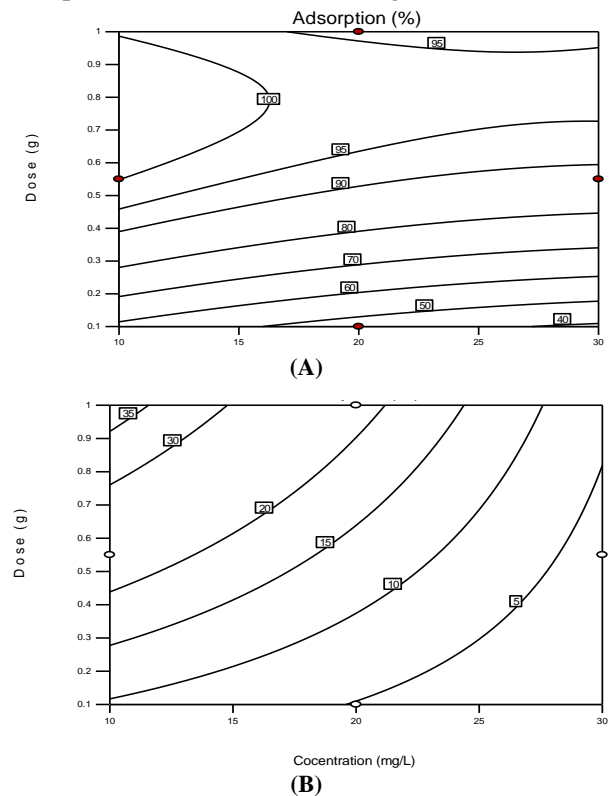


Figure 3. Effect of Fe (II) concentration and glauconite (A) & kaolin (B) dose on adsorption efficiency at the adsorption time of 60 minutes.

These results reveal that, the adsorption efficiency of Fe (II) onto glauconite slightly decreased with increasing ferrous ions concentrations. On the other hand, the adsorption efficiency of Fe (II) onto glauconite increased by increasing glauconite dose. Moreover, at high adsorption time of 60 minutes with 0.1 g of glauconite dose, the adsorption efficiency decreased from 50–60% to about 40% with increasing ferrous ions concentrations from 10 to 30

mg/L (**Figure 3A**). However, at high glauconite dose of 1.0 g and at the same adsorption time of 60 minutes, the adsorption efficiency decreased from about 100% to 95–100% with increasing ferrous ions concentration from 10 to 30 mg/L (**Figure 3A**).

However, the adsorption efficiency of kaolin decreased from 35% to 5% with increasing concentration of Fe (II) ions (**Figure 3B**).

All the experimental results of glauconite have been plotted at the 3-D cube graph as shown in **Figure 4**. From this cube, the highest adsorption efficiency 99.4 % was obtained at high dose of glauconite, low concentration of Fe (II) and high adsorption time. The lowest removal efficiency of about 3.1 % was obtained at the lowest dose of glauconite, the lowest time interval and at the highest concentration of Fe (II).

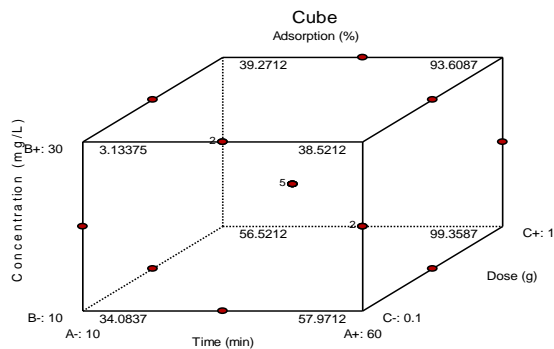


Figure 4. 3-D plot for the results of Fe (II) adsorption on glauconite.

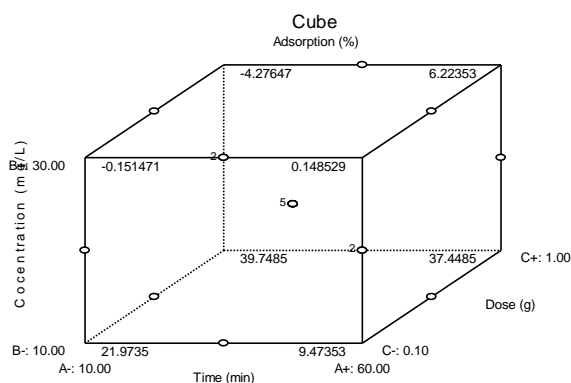


Figure 5. 3-D plot for the results of Fe (II) adsorption on kaolin.

All experimental data of kaolin have been collected at the 3-D cube as shown in **Figure 5**. This cube shows that the highest adsorption efficiency 39.7 % can be obtained at high dose of kaolin, low concentration of ferrous ions and with no significance for adsorption time. At the lowest dose of glauconite, the lowest time interval and at the high-

est concentration of ferrous ions the results show high desorption on the surface of kaolin.

3.4 Surface morphology

SEM images with different levels of magnification factor are taken for glauconite samples in order to show the major features of the structure sight of glauconite surface. **Figures 6** shows the SEM images for glauconite samples with the magnification factor 10,000 and 25,000, respectively. It is obvious that the high surface roughness increases the surface area of adsorption.

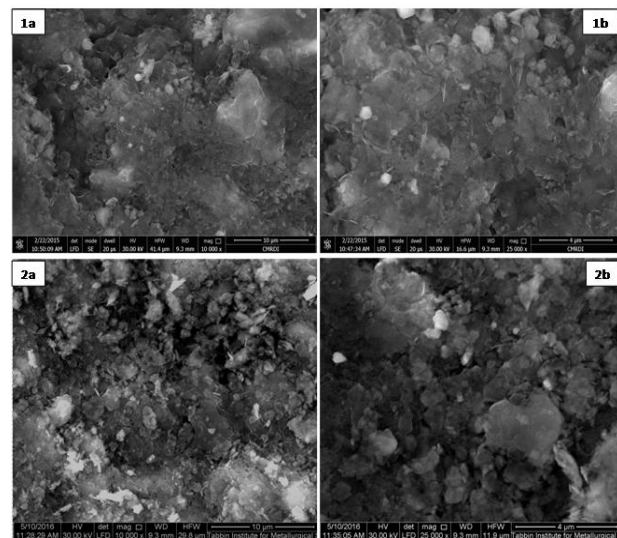


Figure 6. SEM of glauconite with magnification factor (1a x 10000 & 1b x 25000) and kaolin with magnification factor (2a x 10000 & 2b x 25000).

4. Conclusion

Adsorption of ferrous ions on glauconite and kaolin were studied. Statistical experimental design of 3 variables and 3 levels is applied. The interactions of all the adsorption parameters (adsorption time, ferrous ions concentration and adsorbate dose) and their effects on adsorption efficiency were discussed. All the experimental results have been plotted at the 3-D cube graph. For glauconite, the results reveal that, the highest adsorption efficiency of 99.4% is achieved at high dose of glauconite, low concentration of Fe (II) and high adsorption time. The lowest removal efficiency of about 3.1% can be obtained at the lowest dose of glauconite, the lowest adsorption time and at the highest concentration of Fe (II). For kaolin, the results reveal that, the highest adsorption efficiency of 39.7% is achieved at the

high dose of kaolin, low concentration of ferrous ions and with no significance for adsorption time.

From economic point of view, using the lowest glauconite dose and the highest adsorption time with low ferrous ions concentrations gives 50% to 60% adsorption efficiency. So, multi-stage adsorption will be cost-effective. While for kaolin, it gives low adsorption efficiency and there is no high significant effect for iron removal compared to glauconite.

Conflict of interest

The authors declare that they have no conflict of interest.

References

1. Mohan D, Pittman Jr CU. Review activated carbons and low cost adsorbents for remediation of tri- and hexavalent chromium from water. *Journal of Hazardous Materials* 2006; 137: 762–811.
2. Sharma YC, Srivastava V, Singh VK, *et al.* Nano-adsorbents for removal of metallic pollutants from water and wastewater. *Environmental Technology* 2009; 30: 583–609.
3. Bhattacharyya K, Gupta SS. Adsorption of chromium (VI) from water by clays. *Industrial & Engineering Chemistry Research* 2006; 45: 7232–7240.
4. Yuan G, Wu L. Allophanenanoclay for the removal of phosphorus in water and wastewater. *Science and Technology of Advanced Materials* 2007; 8: 60–62.
5. Monvisade P, Siriphannon P. Chitosan intercalated montmorillonite: Preparation, characterization and cationic dye adsorption. *Applied Clay Science* 2009; 42: 427–431.
6. Nasef MM, Yahya AH. Adsorption of some heavy metal ions from aqueous solutions on Nafion 117 membrane. *Desalination* 2009; 249: 677–681.
7. Zaw M, Chiswell B. Iron and manganese dynamics in lake water. *Water Research* 1999; 33: 1900–1910.
8. Wolthoom A, Temminghoff EJM, Weng L, *et al.* Colloid formation in groundwater: Effect of phosphate, manganese, silicate and dissolved organic matter on the dynamic heterogeneous oxidation of ferrous iron. *Applied Geochemistry* 2004; 19: 611–622.
9. Yavuz O, Altunkaynak Y, Guzel F. Removal of copper, nickel, cobalt and manganese from aqueous solution by kaolinite. *Water Research* 2003; 37: 948–952.
10. Acra A, Milki R, Karahagopian Y. Changes in quality of thermal groundwater from unique resources in Lebanon. *International Journal of Environmental Studies* 1981; 19: 63–68.
11. Gu X, Evans LJ, Barabash SJ. Modeling the adsorption of Cd(II), Cu(II), Ni(II), Pb(II) and Zn(II) onto montmorillonite. *Geochimica et Cosmochimica Acta* 2010; 74: 5718–5728.
12. Ossman ME, Abdel-Fatah M, Taha NA. Fe (III) removal by activated carbon produced from Egyptian rice straw by chemical activation. *Desalination and Water Treatment Journal* 2014; 52: 3159–3168.
13. Abollino O, Aceto M, Malandrino M. Adsorption of heavy metals on Na-montmorillonite: Effect of pH and organic substances. *Water Research* 2003; 37: 1619–1627.
14. Li Y, Ding J, Luan Z. Competitive adsorption of Pb²⁺, Cu²⁺ and Cd²⁺ ions from aqueous solutions by multiwalled carbon nanotubes. *Carbon* 2003; 41: 2787–2792.
15. Li Y, Wang S, Wei J. Lead adsorption on carbon nanotubes. *Chemical Physics Letters* 2002; 357: 263–266.
16. Gao Z, Bandosz TJ, Zhao Z. Investigation of factors affecting adsorption of transition metals on oxidized carbon nanotubes. *Journal of Hazardous Materials* 2009; 167: 357–365.
17. Guo X, Zhang S, Shan X. Adsorption of metal ions on lignin. *Journal of Hazardous Materials* 2008; 151: 134–142.
18. Debnath S, Ghosh UC. Nanostructured hydrous titanium (IV) oxide: Synthesis, characterization and Ni (II) adsorption behavior. *Chemical Engineering Journal* 2009; 152: 480–491.
19. O'Reilly SE, Hochella MF. Lead sorption efficiencies of natural and synthetic Mn and Fe-oxides. *Geochimica et Cosmochimica Acta* 2003; 67: 4471–4487.
20. James RO, Healy TW. Adsorption of hydrolyzable metal ions at the oxide—Water interface. I. Co(II) adsorption on SiO₂ and TiO₂ as model systems. *Journal of Colloid and Interface Science* 1972; 40: 42–52.
21. Spark KM, Johnson BB, Wells JD. Characterizing heavy-metal adsorption on oxides and oxyhydroxides. *European Journal of Soil Science* 1995; 46: 621–631.
22. Forbes EA, Posner AM, Quirk JP. The specific adsorption of divalent Cd, Co, Cu, Pb, and Zn on goethite. *European Journal of Soil Science* 1976; 27: 154–166.
23. Benjamin MM, Leckie JO. Competitive adsorption of Cd, Cu, Zn, and Pb on amorphous iron oxyhydroxide. *Journal of Colloid and Interface Science* 1981; 83: 410–419.
24. Nowack B, Sigg L. Adsorption of EDTA and metal-EDTA complexes onto goethite. *Journal of Colloid and Interface Science* 1996; 177: 106–121.
25. Ainsworth CC, Pilon JL, Gassman PL, *et al.* Cobalt, cadmium, and lead sorption to hydrous iron oxide: Residence time effect. *Soil Science Society of America Journal* 1994; 58: 1615–1623.
26. Tewari PH, Campbell AB, Lee W. Adsorption of Co²⁺ by oxides from aqueous solution. *Canadian Journal of Chemistry* 1972; 50: 1642–1648.
27. Johnson BB. Effect of pH, temperature, and concentration on the adsorption of cadmium on goethite. *Environmental Science & Technology* 1990; 24:

- 112–118.
28. Fokkink LGJ, de Keizer A, Lyklema J. Temperature dependence of cadmium adsorption on oxides: I. experimental observations and model analysis. *Journal of Colloid and Interface Science* 1990; 135: 118–131.
 29. Chapman HD. Cation-exchange capacity. In: Black CA (editors). *Methods of soil analysis-chemical and microbiological properties*. Agronomy 1965; 9: 891–901.
 30. Box GEP, Behnken DW. Some new three level designs for the study of quantitative variables. *Technometrics* 1960; 2: 455–475.
 31. Chaturvedi S, Dave PN. Removal of iron for safe drinking water. *Desalination* 2012; 303: 1–11.
 32. Yavuz Ö, Guzel R, Aydin F, *et al.* Removal of cadmium and lead from aqueous solution by calcite. *Polish Journal of Environmental Studies* 2007; 16 (3): 467–471.

ORIGINAL RESEARCH ARTICLE

Photocatalytic oxidation of psychoactive drug Duloxetine: Degradation kinetics, inorganic ions and phytotoxicity evaluation

Sophia Tsoumachidou^{1*}, Maria Valari², Ioannis Poullos¹

¹Laboratory of Physical Chemistry, Department of Chemistry, Aristotle University of Thessaloniki, 54124 Thessaloniki, Greece; E-mail: stsoumac@chem.auth.gr

²InterBalkan Environment Center, 57200, Lagadas, Greece.

ABSTRACT

Pharmaceutically active compounds, emerging extensively in ecosystems as pollutants, have become an important environmental and public health issue, since they can contaminate drinking water and pose threat to wildlife and human health. Therefore, efforts should be made in order to establish proper methods for their inactivation or elimination in the environment. The photocatalytic oxidation of psychoactive drug Duloxetine (DLX) has been investigated. In the case of heterogeneous photocatalytic oxidation, the effect of TiO₂ P25 concentration (0.1–1 g L⁻¹), initial concentration of H₂O₂ (0.25–0.2 g L⁻¹) and Fe³⁺ (0.00175–0.014 g L⁻¹) and pH of the solution (3–10) on initial reaction rates were evaluated, while for homogeneous photocatalytic oxidation the effect of the amount of H₂O₂ (0.25–0.2 g L⁻¹) and Fe³⁺ (0.00175–0.014 g L⁻¹) were investigated. Additionally, the conversion of the heteroatoms in the molecule of DLX to inorganic ions (NO₃⁻, NH₄⁺, SO₄²⁻) during photocatalytic process has been observed, and phytotoxicity testing, using three plant species, was carried out in order to examine the effect of photocatalytic oxidation on the toxicity of DLX. According to the results presented in this study, both heterogeneous and homogeneous photocatalytic oxidation is an efficient methodology for DLX degradation.

Keywords: Duloxetine; Photocatalytic Oxidation; Psychoactive Drug; Urban Wastewater

ARTICLE INFO

Received 27 April 2020
Accepted 29 May 2020
Available online 9 June 2020

COPYRIGHT

Copyright © 2020 Sophia Tsoumachidou, *et al.*
EnPress Publisher LLC. This work is licensed under the Creative Commons Attribution-NonCommercial 4.0 International License (CC BY-NC 4.0).
<http://creativecommons.org/licenses/by-nc/4.0/>

1. Introduction

Pharmaceutical active compounds (PhACs) are turning into an essential ecological and public health issue, because of their expanding use and subsequent release in the aquatic environment and their potential effects on wildlife and humans. Drug residues that have been identified recently in urban surfaces, groundwater and drinking water^[1,2], are mostly introduced in the sewage system through excretion of unmetabolized compounds after medical use or inappropriate disposal^[3]. However, effluents of wastewater treatment plants (WWTPs) are generally recognized as the major emission pathway of pharmaceuticals into the environment^[4], due to the fact that conventional WWTPs are designed to remove solids and nutrients and to reduce the biological oxygen demand of the effluent^[5]. Even though, pharmaceuticals usually do not have toxic impact on aquatic organisms, since they are detected at low or very low concentrations (ng to µg per liter), concerns have been raised for chronic exposure, since their continuous input to the environment exceed their degradation rate, acting, thus, as slightly persistent pollutants^[6].

Psychoactive compounds are a group of drugs used to treat symptoms of neurological disorders such as depression, schizophrenia, bipolar disorder,

or anxiety disorders. According to Global Burden of Disease Study, jointly published by World Health Organization (WHO) and other groups, neuropsychiatric disorders have emerged as priority health problems worldwide, projected to be the second most frequent disease by 2020^[7], while Almeida *et al.* showed that lifetime prevalence of such disorders can reach over 25%^[8]. Moreover, according to WHO, around 10% of fully grown persons suffer from such disorders at any point in their lifetime^[9]. Many previous studies showed that, exposure of aquatic organisms to psychoactive compounds may affect reproduction^[10], endocrine function^[11], or photosynthesis^[12]. Furthermore, recent studies showed that psychoactive drugs may alter fish and benthic invertebrates behavioral responses^[13], and also, induce fish gene expression profiles associated with human idiopathic autism^[14].

During the current economic crisis in Greece, the consumption of psychoactive substances has risen significantly, resulting in an increase in their concentration in urban wastewater^[15]. The presence of psychoactive substances and/or their metabolites is confirmed, not only in urban wastewater, but also in aquatic plants and animal tissues^[16,17], underlining the possible consequences for human health and ecosystems balance. Pollution of European waters by pharmaceuticals is a ubiquitous phenomenon^[18,19] and is receiving great attention, as stated in the EU Directive 2013/39/EU19 on priority substances in the field of water policy^[20]. Notwithstanding, wastewater management remains an open issue for the members of the European Union, since legislations is incomplete and in need of update^[21]. Given the increasing interest about aquatic environment contamination by psychoactive compounds, legislation has recently begun to acknowledge this potential problem in order for environmental regulations to require explicit testing for any PhACs in water bodies.

In order to solve various problems encountered by conventional methods for the degradation of organic species resistant to them, many researchers have turned their attention to a particular group of oxidation techniques called Advanced Oxidation Processes (AOPs). Among AOPs, heterogeneous and homogeneous photocatalytic oxidation has been

studied extensively and it has been demonstrated to be an alternative to conventional methods for the removal of organic pollutants from water and air^[22,23]. Meanwhile, photocatalytic oxidation has the potential to use solar energy, integrating, in this way, mild energy into environment protection.

The aim of this work was the application of the preceding methods at the degradation of psychoactive drug Duloxetine (DLX), a serotonin norepinephrine reuptake inhibitor (SNRI) widely used for patients with depression and neuropathic pain. The study provides a further insight to oxidation kinetics (i.e. determination of factors affecting oxidation rate) and estimates mineralization degree towards the corresponding oxidation process. In addition, the conversion of the heteroatoms in the molecule of DLX to inorganic ions (NO_3^- , NH_4^+ , SO_4^{2-}) during photocatalytic process has been observed, and phytotoxicity testing, using three plant species, was carried out in order to examine the effect of photocatalytic oxidation on the toxicity of DLX.

2. Material and methods

2.1 Reagents

Duloxetine hydrochloride was the product of Sigma-Aldrich and was used as received. NaOH and HCl were used to adjust the pH when necessary. Commercially available TiO_2 catalyst from Evonik, Aeroxide TiO_2 P25 (TiO_2 P25, 70% anatase and 30% rutile with BET surface area of $55 \pm 15 \text{ m}^2 \text{ g}^{-1}$) was employed in this study. Iron chloride ($\text{FeCl}_3 \cdot 6\text{H}_2\text{O}$) and hydrogen peroxide (H_2O_2 , 30% w/v) were purchased from Alfa Aesar and Panreac Química, respectively, and they were used without further purification. Double distilled water was used throughout the experimental processes.

2.2 Experimental set-up and procedures

A thermostated pyrex cell of 0.25 L capacity used as the reaction vessel, was fitted centrally with UV-A or visible light of identical dimensions and geometry, and covered with a black cloth to avoid interactions with ambient light. An Osram Dulux® S blue UV-A lamp (9W/78, 350–400 nm) and an Osram Dulux® S blue lamp (9W/71, 400–550 nm) were used as artificial light sources. The photon flux emitted from the lamps was determined acti-

nometrically using the potassium ferrioxalate [$K_3Fe(C_2O_4)_3 \cdot 3H_2O$] method^[24]. The radiation intensities obtained for the UV-A and the visible lamp were $1.268 \cdot 10^{-4} \text{ E min}^{-1} \text{ L}^{-1}$ and $0.724 \cdot 10^{-4} \text{ E min}^{-1} \text{ L}^{-1}$, respectively.

In order to check reproducibility of the results, all photocatalytic experiments were performed in duplicate and, in some cases, in triplicate, with the standard deviation never to exceed 5% for degradation experiments and 10% for DOC and inorganic ions analysis.

It must be mentioned that DLX concentration employed in all experiments was substantially higher than the typically one found in environmental samples, in order to assess treatment efficiency within a measurable time scale and accurate determine residual concentrations with the analytical techniques employed in this work.

2.3 Analytical methods

Sample absorbance was scanned in the 200–400 nm wavelength region on a Shimadzu UV-1700 spectrophotometer and changes in the concentration of DLX were monitored via its characteristic absorption band at 289 nm. A Shimadzu V_{CSH} Total Organic Carbon Analyzer was used for following mineralization by measuring the dissolved organic carbon (DOC), while pH was determined with a Mettler Toledo S20 SevenEasy pH meter. Colorimetric determination with spectrophotometric detection with titanium (IV) oxysulfate-sulfuric acid solution according to DIN 38409 H15, a method based on the formation of a yellow complex from the reaction of titanium (IV) oxysulfate with H₂O₂, was used for residual hydrogen determination.

A Shimadzu system, comprising of an LC-10 AD pump, a CTO-10A column oven and a CDD-6A conductivity detector (0.25 μL flow-cell), was used for inorganic anions determination. Anions separation was performed on an Alltech Allsep column preceded by a guard column of the same material, using a mixture of phthalic acid and lithium hydroxide at 1.5 mL min^{-1} constant flow. Temperature of column and conductivity cell was constantly held at 35 °C and 38 °C, respectively. Before LC analysis mobile phases were degassed with helium stream.

An ion chromatography (IC) unit LC 20 AD (Shimadzu), consisted of an LC-20 pump, a ADsp degasser, a DGU-20A5, a CDD-10 A VP conductivity detector and a CTO-20A oven, was used for inorganic cations identification. Cations separation was held on an IC YK-421 analytical column, with a mobile phase of boric acid, tartaric acid and dipicolinic acid, through adsorption and desorption processes and detected based on their elution time. Before their injection in the column, samples were filtered through a 0.45 mm membrane filter.

2.4 Phytotoxicity evaluation

Phytotoxicity measurements was performed in order to determine photocatalytic efficacy to decrease DLX toxicity, using the standard Phytotoxkit microbiotest, a bioassay based on three species of higher plants: the monocotyl Sorgho (*Sorghum saccharatum*), the dicotyl garden cress (*Lepidium sativum*) and the dicotyl mustard (*Sinapis alba*).

This article measures both the decrease/absence of seed germination and the decrease of roots and/or shoots after 3 days of exposure of the seeds to toxicants or contaminated soils. For this purpose, reference soil (an OECD analogous artificial soil composed of sand, kaolin, peat and pH adjusted with CaCO₃) was added in the lower compartment of the test plates and hydrated with the samples, while control tests were prepared using distilled water. The soil surface was flattened and covered by paper filter. Tests were carried out in three replicates for each sample and for each type of plant. The seeds were left in a dark incubator at 25 °C for 3 days prior to recording and interpretation of results. Digital pictures of the plates were analyzed using Image J v1.49 software (Wayne Rasband, national Institutes of Health, USA). The test results were evaluated comparing the mean number of germinated seeds and the mean root/shoot length for the three replicates in the control and in each examined sample. The percentage effect of the tested effluents on seed germination inhibition (GI), root growth inhibition (RGI) and shoot growth inhibition (SGI) was calculated applying the following formula.

$$\%effect = \frac{A-B}{A} \times 100 \quad (1)$$

where A represents the average number of germinated seeds or the average root length in the control water and B represents the same parameters for the tested solution.

3. Results and discussion

3.1 Heterogeneous photocatalytic oxidation of DLX

3.1.1 Effect of catalyst's loading

The degradation of an organic compound may be influenced strongly by TiO_2 dosage, since this parameter is an important factor in slurry photocatalytic processes. **Figure 1** depicted the effect of varying the quantity of TiO_2 P25 on the observed initial reaction rate r_o of DLX degradation and mineralization degree. The proper catalyst amounts were added to 0.01 g L^{-1} DLX solutions in natural pH (~ 5.5) and then irradiated with UV-A light. The pH value falls about 1.5 unit after the photocatalytic process. Preliminary experiments with DLX solution containing TiO_2 in the dark or illuminated DLX solution without the presence of catalyst showed that both illumination and catalyst are essential for the degradation of the drug (data not shown).

The values of the initial degradation rate and mineralization degree in relation to catalyst dosage are depicted in **Figure 1**. The initial reaction rates were calculated by a linear fit of C-t data obtained during the first minutes of illumination, in order to minimize variations resulting in the competitive effects of the intermediate products and pH changes. As it can be seen, the increase of TiO_2 loading from 0.1 to 0.75 g L^{-1} led to an increase in the initial reaction rate. Moreover, DOC was 95.9% reduced after 120 min of illumination, when heterogeneous photocatalytic oxidation was conducted in the presence of 1 g L^{-1} TiO_2 P25. The observed trend can be attributed to the evidence that a catalyst dose increase can provide larger surface area for DLX oxidation and, additionally, may increase the active sites amount that can also provide an enhancement to the photocatalytic efficiency^[25]. Nonetheless, above a certain value a slightly decrease in the reaction rate is observed, a behavior similar to our previous studies^[26,27], which may be due to a possible aggregation of the catalyst (particle-particle interac-

tions) which result in a loss of surface area available for light-harvesting^[28]. Furthermore, there may be an increase in the opacity of the solution leading to a decrease of the light penetration causing the lesser activation of the catalyst resulting in marginal change or even reduced degradation due to the negative contributions of aggregation or reduced energy^[25,29].

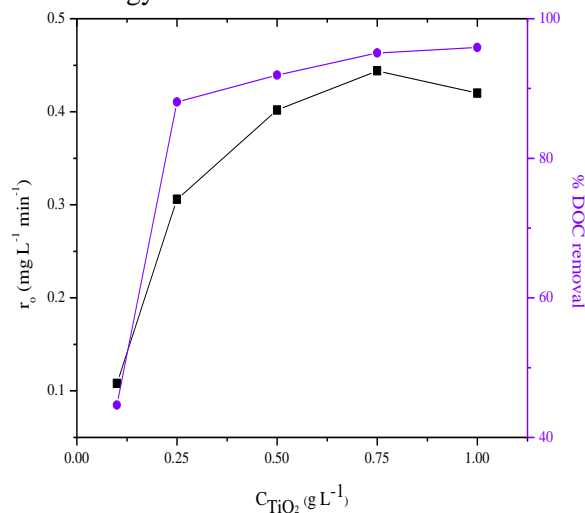


Figure 1. Dependence of the initial reaction rate for constant DLX concentration, r_o , (■) on the concentration of the TiO_2 P25 and DLX mineralization degree (●) at 120 min of photocatalytic process (initial conditions: 0.01 g L^{-1} DLX, $\text{pH} \approx 5.5$, $T = 25^\circ\text{C}$, UV-A illumination).

Considering the above, in order to ensure total absorption of efficient photons and avoid excess catalyst, the optimum catalyst dosage must be determined^[30]. As shown in **Figure 1**, the optimum value is approximately 0.75 g L^{-1} . Observing that with lower catalyst concentration a good efficiency was obtained and considering the necessity of a good balance between process efficiency and experimental costs, in the following experimental runs, the catalyst dosage was chosen to be 0.25 g L^{-1} .

3.1.2 Effect of electron scavengers

The acceleration of the photocatalytic oxidation by the addition of oxidizing species (e.g. H_2O_2) with the potential to capture the photogenerated electrons is an extensively studied procedure^[31]; due to various individual phenomena that are taking place, such as increment of trapped e^- , avoiding, thus, the e^-/h^+ recombination, enhanced HO^\bullet and secondary oxidizing species generation, intermediate compounds oxidation rate increment and reduction of potential problems caused by low O_2 con-

centration decrease^[32]. It is established that, H₂O₂ gets a photogenerated electron from the conduction band, promoting, therefore, the charge separation, while, it can also produce HO[•] via superoxide. However, too high peroxide dosage can promote a negative effect on organic pollutants oxidation, since H₂O₂ is also a semiconductor valence band holes and HO[•] scavenger. Therefore, as observed in previous studies, the effect of oxidant additives, such as hydrogen peroxide, can be conflicting depending on the amount and the particular experimental conditions^[33].

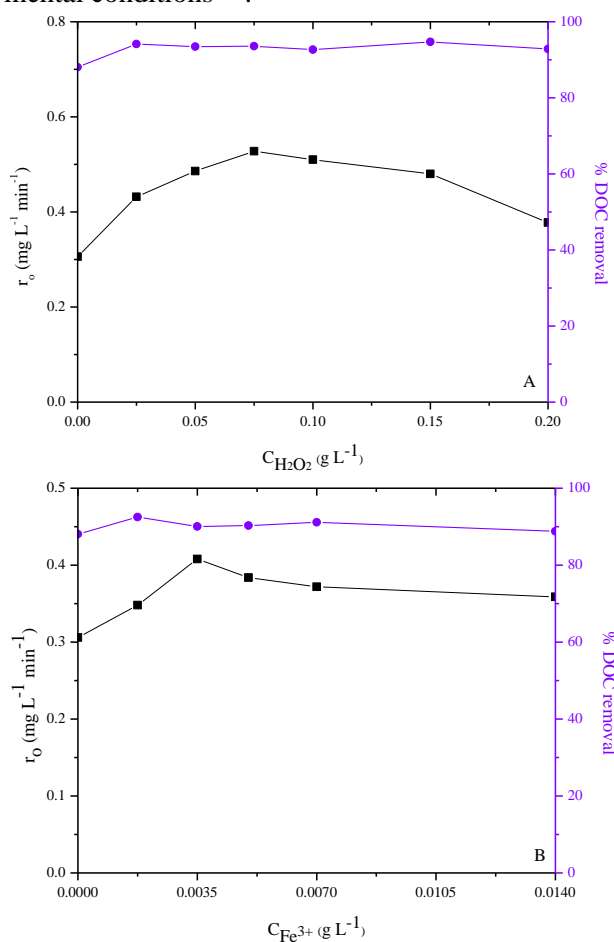


Figure 2. Effect of H₂O₂ (A) and ferric ions (B) concentration on the initial reaction rate of DLX degradation (■) and DLX mineralization degree (●) at 120 min and 90 min, respectively, of photocatalytic process (initial conditions: 0.01 g L⁻¹ DLX, 0.25 g L⁻¹ TiO₂ P25, pH ≈ 5.5, T = 25 °C, UV-A illumination).

In order to investigate H₂O₂ role, photocatalytic experimental runs for the oxidation of 0.01 g L⁻¹ DLX in the presence of 0.25 g L⁻¹ TiO₂ P25, were performed with different H₂O₂ dosage and at the natural pH value of drug solutions. **Figure 2A** depicted the effect of H₂O₂ addition on TiO₂-mediated photocatalytic mineralization of

DLX. In all H₂O₂-induced experiments presented in **Figure 2A**, over 80% of DLX was eliminated within 20 minutes of reaction. An increase in the concentration of H₂O₂ from 0.025 to 0.075 g L⁻¹ led to a small increase in the oxidation rate from 0.31 to 0.53 g L⁻¹ min⁻¹, while higher H₂O₂ dosage resulted to a slightly r_o reduction down to 0.38 g L⁻¹ min⁻¹, a behavior that has been also obtained in similar studies. Furthermore, mineralization experimental runs showed that DLX dissolved organic carbon was almost 95% reduced after 120 min of illumination for all H₂O₂ concentrations studied.

Metal ions addition has also been proven to increase photocatalytic effectiveness, since they are able to trap, separate and transfer the photogenerated electrons and holes in semiconductors^[34]. In an attempt to enhance the efficiency of the TiO₂-induced photocatalytic process, iron in the form of Fe³⁺ was introduced in the reaction vessel prior the beginning of the reaction. The facilitation by Fe³⁺ at DLX degradation and mineralization is shown in **Figure 2B**. The observed enhancing effect could be attributed to interactions between iron species and TiO₂^[35], the efficient electron-hole pair separation, since the addition of suitable scavengers can suppress the photocatalytic process efficiency limitation occurred by the recombination of photogenerated electrons and holes. Ferric ions act as a photo-generated e⁻ or h⁺ trap, inhibiting, thus, their recombination and enhancing their lifetimes^[25]. Furthermore, Fe³⁺ reduction to Fe²⁺ by a photo-generated e⁻ in TiO₂ particles can also conduce to the suppression of electron-hole recombination^[36].

3.1.3 Effect of solution's pH

The pH of the solution seems to have a significant role in the heterogeneous photocatalytic process efficiency^[37,38], since surface charge state and flat band potential, among other catalyst's properties, appear to have a high pH dependence. Additionally, the degradation rate may be enhanced or inhibited by catalyst's surface and organic molecule electrostatic attraction or repulsion^[39]. Moreover, the size of TiO₂ particles, the catalyst's interaction with solvent molecules and the type of radicals or intermediates formed during photocatalytic process, may be pH-affected. All aforementioned factors can

affect organic molecules adsorption onto catalyst and, consequently, influence the observed degradation rates^[40].

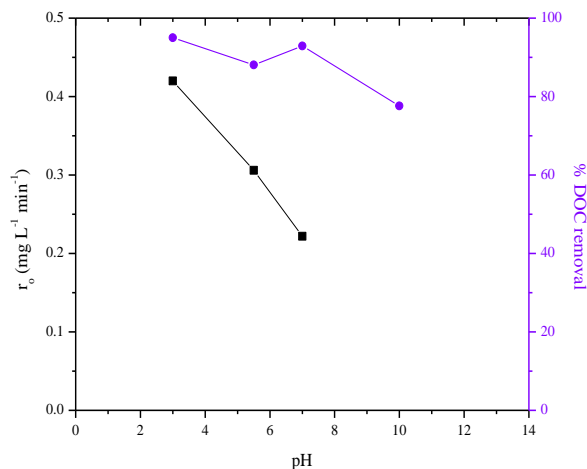


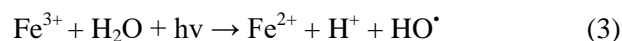
Figure 3. Effect of pH on the initial reaction rate of DLX degradation (■) and DLX mineralization degree (●) at 120 min of photocatalytic process (initial conditions: 0.01 g L⁻¹ DLX, 0.25 g L⁻¹ TiO₂ P25, pH ≈ 5.5, T = 25 °C, UV-A illumination).

Solution's initial pH impact on photocatalytic oxidation was studied by performing the experiments with 0.25 g L⁻¹ TiO₂ P25 in 0.01 g L⁻¹ DLX solution, under UV-A illumination and adjusting the solution pH from acidic values to alkaline ones; the results on degradation rate of DLX and its DOC reduction after 120 min of illumination are demonstrated in **Figure 3**. Usually, at pH values below its pK_a, an organic compound exists as neutral species or in a cationic form, whereas above this value, gets a negative charge. For that reason and considering that at this area the catalyst's surface is positively charged, it is not likely to achieve great electrostatic attractions between the surface of the catalyst and the organic molecules. With pH increment, substance's negative charging is getting stronger and, therefore, the electrostatic interactions are getting more remarkable, causing, this way, an enhancement in the photocatalytic efficiency^[41]. In this case, as it can be seen from **Figure 3**, when the pH value decreases from 7 to 3 an increase of the DLX degradation rate is observed. Although opposite to the expected, this phenomena can be explained by the fact that DLX has been found in previous studies to be unstable in acidic media^[42,43].

3.2 Homogeneous photocatalytic oxidation of DLX

Fenton reagent is a drawing attention oxidative

system, since hydrogen peroxide is widely and environmentally safe and iron is a very abundant and non-toxic material^[44]. Considering its high ability to generate HO[•] in a very simple way, as a result of H₂O₂ decomposition by Fe²⁺ in acidic medium, Fenton method has been widely applied for organic compounds oxidation^[45]. The advantages of photo-Fenton process are the safe and environmentally-benign nature of reagents and relatively simple operating principles as well as short reaction time and the absence of mass transfer limitations^[46]. In addition, with the use of light (UV-A or visible, artificial or natural) the process can be catalytic, since the photo-reduction of Fe³⁺ to Fe²⁺ produces additional hydroxyl radicals and leads to the catalyst regeneration (Equation (3))^[45].



One of the main parameters that influence the Fenton and photo-Fenton processes is the iron amount. In the majority of cases, the photocatalytic effect is enhanced when the iron concentration is increased, since more hydroxyl radicals' production is obtained^[47-49].

As the iron concentration increases, the regeneration of Fe²⁺ from Fe³⁺ results in the rapid production of additional HO[•]^[47]. However, with too high ferric amount in the solution, dark zones can be generated in the photoreactor, since the incident ray is attenuated too strongly along the optical pathlength, reducing, for that reason, the process effectiveness. Moreover, although more radicals can be produced (Equation (3)), they can be scavenged by reacting with other ferrous ions, which lead to the reduction of their amount^[50].

As it can be seen in **Figure 4A**, the increment of ferric ions from 0.00175 to 0.014 g L⁻¹ led to an increase on the photo-Fenton induced mineralization percentage of DLX, from 78.7 to 94.8% when the solution was illuminated for 120 min with UV-A light and from 70.8 to 94% under visible illumination. In all homogeneous photocatalytic experimental runs the pH was low enough (pH = 3.2–3.3), since iron precipitates at higher pH.

Iron concentration has proven to be a signifi-

cant parameter, not only because it can affect the capital costs, but also the operating costs, since shorter reaction times are required^[51]. In the presence of high iron amount, the issue of the iron-separation step at the end of the photocatalytic process appears. Consequently, it is considered critical to choose the proper iron concentration in order to achieve as short reaction time as possible, and at the same time not to exceed the limits defined by the direct discharge to biological municipal WWTPs regulations (different amounts are permitted in the EU, USA, Switzerland, etc.)^[52].

It should be mentioned that DLX organic load reduction was found to be always faster in the early stages of the reaction than in the later ones, maybe due to the fact that iron ions catalyses H_2O_2 to produce HO^\bullet quickly, in the first stages of the photocatalytic oxidation^[52].

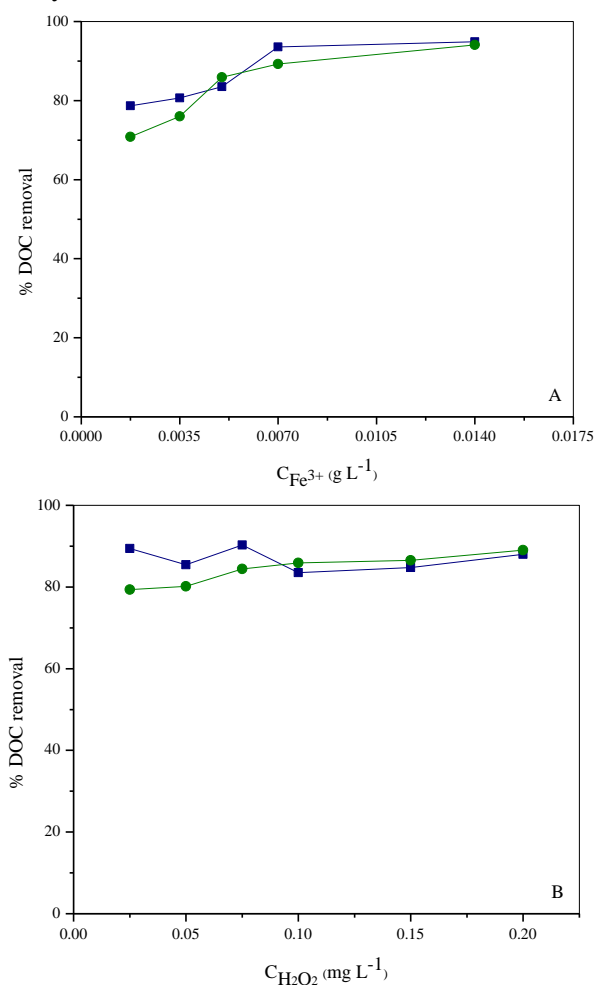
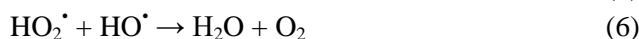
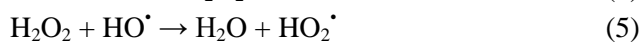


Figure 4. Influence of ferric ions (A) and H_2O_2 (B) concentration on the degree of mineralization of DLX under UV-A (■) and visible (●) irradiation after 120 min (initial conditions: (A) 0.01 g L^{-1} DLX, 0.1 g L^{-1} H_2O_2 , $\text{pH} \approx 3.3$, $T = 25^\circ\text{C}$; (B) 0.01 g L^{-1} DLX, 0.005 g L^{-1} Fe^{3+} , $\text{pH} \approx 3.3$, $T = 25^\circ\text{C}$).

The influence of H_2O_2 concentration was investigated by several previous studies^[47,54], with the main findings to be that neither too low H_2O_2 amount nor too high may be applied, since in the first case a Fenton reaction rate reduction is occurred, while, in the second H_2O_2 competes successfully for HO^\bullet and becomes decomposed into molecular oxygen and water, while oxidizing the pollutant. However, in general, there is a ther broad concentration interval between both extremes, where none of those two phenomena occurs^[49].

As shown in **Figure 4B**, the use of extra H_2O_2 dosage did not result to any remarkable improvement in both UV-A and visible-irradiated process efficiency of DLX photo-Fenton mineralization. Even though, with the oxidant decomposition to be enhanced, a higher amount of HO^\bullet is expected, its increment can provide an adverse effect by slowing down the oxidation process, since the competition interactions are enhanced in the case of H_2O_2 excess^[55]; mainly the recombination of the produced HO^\bullet , as well as their recombination with H_2O_2 , contributing to the HO^\bullet scavenging capacity (Equations (4)–(6))^[47,54].



3.3 Inorganic Ions

Temporal profiles of sulfur (released as sulfate ions) and inorganic nitrogen (i.e. nitrates, nitrites and ammonium ions) released during heterogeneous and homogeneous photocatalytic mineralization of DLX are shown in **Figure 5**. Profiles do not show actual concentrations but they correspond to the percentage of the theoretical amount of sulfur or nitrogen initially present in the molecule.

The heteroatoms contained in the organic compounds are readily converted to inorganic ions that remain in the liquid phase. In some cases, photooxidation of nitrogen is relatively slow and the mineralization of organic pollutants containing nitrogen seems to be complex, since nitrate, nitrite, ammonium ions and free nitrogen are formed^[56]. As it can be seen in **Figure 5A**, in the first 30 min of

heterogeneous photocatalytic oxidation only 25% of organic nitrogen has converted into inorganic, while total conversion occurred after 120 min of process. In the case of homogeneous photocatalytic mineralization, a complete conversion has not achieved, but almost 70% of organic nitrogen was converted after 120 min (**Figure 5B**).

On the other hand, high percentage of organic sulfur is converted to inorganic, for both processes, while with photo-Fenton-induced oxidation almost total amount of sulfur is converted to inorganic within the first 30 min of reaction. The decrease of S^- amount, in the case of homogeneous photocatalytic oxidation, may be due to the fact that iron forms a mixture of $FeSO_4^+$ and $Fe(SO_4)_2^-$ complexes in the presence of sulfur^[57].

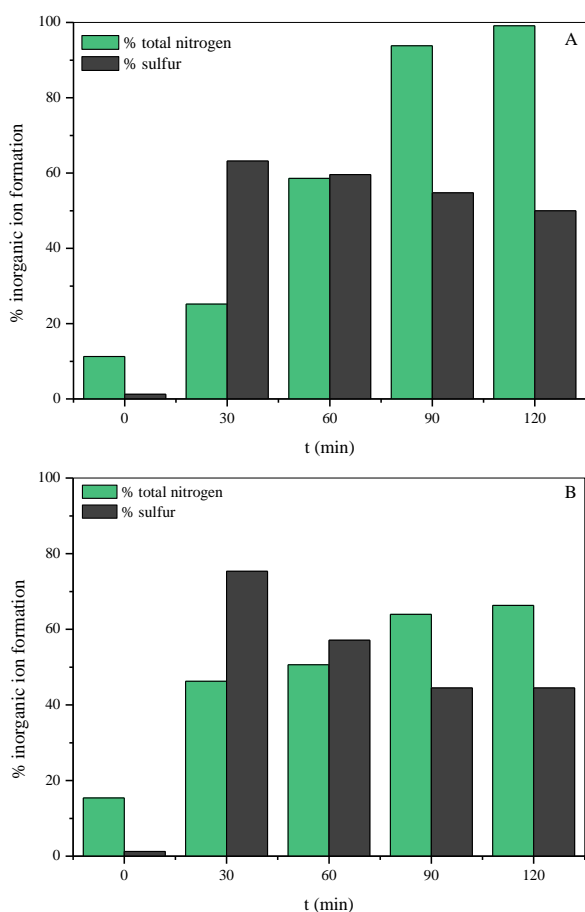


Figure 5. Release of inorganic anions during heterogeneous (A) and homogeneous (B) photocatalytic mineralization of DLX (initial conditions: (A) 0.01 g L⁻¹ DLX, 0.25 g L⁻¹ TiO₂ P25, 0.1 g L⁻¹ H₂O₂, pH ≈ 5.5, T = 25 °C, UV-A illumination; (B) 0.01 g L⁻¹ DLX, 0.007 g L⁻¹ Fe³⁺, 0.1 g L⁻¹ H₂O₂, pH ≈ 3.3, T = 25 °C, UV-A illumination).

3.4 Phytotoxicity evaluation

For the investigation of the effect of the TiO₂ photocatalytic process on DLX phytotoxicity,

samples of the initial drug solution (raw DLX) and at the end of the process (treated DLX) were selected. It should be noted that there were not any inhibition effects by the H₂O₂, since residual hydrogen peroxide was measured during photocatalytic oxidation and found to be totally eliminated after the reaction. The effects of DLX samples on the plants are depicted in **Figure 6** and they are expressed as root growth inhibition (RGI), shoot growth inhibition (SGI) and seed germination inhibition (GI).

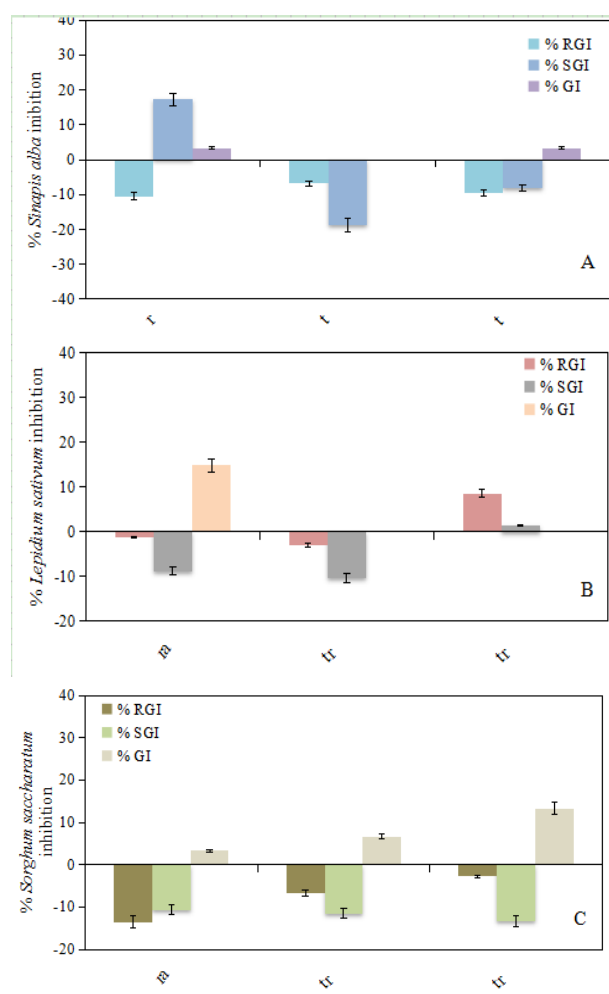


Figure 6. Inhibition effect (%) of DLX before and after treatment with heterogeneous (initial conditions: 0.01 g L⁻¹ DLX, 0.25 g L⁻¹ TiO₂ P25, 0.1 g L⁻¹ H₂O₂, pH ≈ 5.5, T = 25 °C) and homogeneous (initial conditions: 0.01 g L⁻¹ DLX, 0.007 g L⁻¹ Fe³⁺, 0.1 g L⁻¹ H₂O₂, pH ≈ 3.3, T = 25 °C) photocatalytic oxidation on *Sinapis alba* (A), *Lepidium sativum* (B), *Sorghum saccharatum* (C), under 120 min of UV-A illumination.

As it can be seen from **Figure 6A**, both TiO₂ and photo-Fenton-induced photocatalytic processes improved the phyto-compatibility of DLX, since exposure to the treated solutions affected the root length of *Sinapis alba*. The raw DLX solution ex-

erted higher toxicity to the above species as it brought on 17.3% shoot growth inhibition. Furthermore, the seed germination of *Lepidium sativum* was affected, reaching 14.8% after incubation with raw DLX and total toxicity elimination with both treated solutions (**Figure 6B**).

On the contrary, root and shoot growth germination of *Lepidium sativum* was negatively affected to photo-Fenton-treated solution exposure, since raw DLX exerted no toxicity to the above parameters, while the treated solution brought a toxic effect of 8.6 and 1.5%, respectively. This observation indicates the need for further photocatalytic processing of DLX, since, apparently, the metabolites that are formed during drug's degradation are more toxic than the parent compound. The same conclusion is derived from **Figure 6C**, where it can be seen that the toxic effect at seed germination of *Sorghum saccharatum* increased from 3.3%, that was after the exposure to raw DLW, to 6.7 and 13.3% after incubation with treated DLX (heterogeneous and homogeneous photocatalytic oxidation, respectively).

4. Conclusions

In the present work the photocatalytic oxidative degradation of DLX, a psychoactive drug detected in urban wastewater, has been demonstrated.

With the use of TiO₂ P25 as photocatalyst under UV-A illumination, quantitative mineralization of the organic molecule occur after 2 hours, while as the catalyst dosage increased the initial reaction rate of the drug degradation increased.

In all experimental runs that H₂O₂ was added in the drug solution over 80% of DLX was eliminated within 20 minutes of reaction. An increase in the concentration of H₂O₂ led to a small increase in the reaction rate of oxidation, while a higher concentration of H₂O₂ resulted to a slightly reaction rate reduction. Moreover, mineralization experiments showed that DOC of DLX was almost 95% reduced after 120 min of illumination for all H₂O₂ concentrations studied.

No remarkable enhancement was obtained by the attempt to enhance the efficiency of the TiO₂-induced heterogeneous photocatalytic process by introducing Fe³⁺ in the reaction solution.

The study of the effect of drug solution's pH showed that the higher degradation rate occurred at pH 3.

In the case of homogeneous photocatalytic oxidation, the increment of ferric ions led to an increase of DLX mineralization percentage in both UV-A and visible-irradiated process efficiency. On the other hand, the use of extra H₂O₂ dosage did not result to any remarkable improvement in DLX photo-Fenton-induced mineralization.

Inorganic ions formation analysis showed that total organic nitrogen was converted into inorganic after 120 min of heterogeneous photocatalytic oxidation, while in the case of homogeneous process, almost 70% of organic nitrogen was converted after the same illumination time. On the other hand, high percentage of organic sulfur was converted to inorganic, for both processes, while with photo-Fenton-induced oxidation almost total amount of sulfur is converted to inorganic within the first 30 min of reaction.

Phytotoxicity evaluation showed that both TiO₂ and photo-Fenton-induced photocatalytic processes improved the phyto-compatibility of DLX, since exposure to the treated DLX solutions affected the root length of *Sinapis alba*. Moreover, the seed germination of *Lepidium sativum* was affected, achieving total toxicity elimination with both treated solutions. On the other hand, root and shoot growth germination was negatively affected to photo-Fenton-treated solution exposure, since raw DLX exerted no toxicity to the above parameters, while the treated solution brought a toxic effect of 8.6 and 1.5%, respectively. Additionally, the toxic effect at seed germination of *Sorghum saccharatum* increased after incubation with treated DLX. According to the above, the need for further photocatalytic processing of DLX is required, since, apparently, the metabolites that are formed during drug's degradation are more toxic than the parent compound.

Conflict of interest

The authors declare that they have no conflict of interest.

Acknowledgements

This research project was funded by State Scholarships Foundation (IKY), through IKY Fellowships of Excellence for Postgraduate Studies in Greece-Siemens Program.

References

1. Hofman-Caris CHM, Siegers WG, Van de Merlen K, *et al.* Removal of pharmaceuticals from WWTP effluent: Removal of EFOM followed by advanced oxidation. *Chemical Engineering Journal* 2017; 327 (Supplement C): 514–521. doi: <https://doi.org/10.1016/j.cej.2017.06.154>.
2. Pereira AMPT, Silva LJG, Laranjeiro CSM, *et al.* Human pharmaceuticals in Portuguese rivers: The impact of water scarcity in the environmental risk. *Science of the Total Environment* 2017; 609 (Supplement C): 1182–1191. doi: <https://doi.org/10.1016/j.scitotenv.2017.07.200>.
3. Xekoukoulotakis NP, Xinidis N, Chroni M, *et al.* UV-A/TiO₂ photocatalytic decomposition of erythromycin in water: Factors affecting mineralization and antibiotic activity. *Catalysis Today* 2010; 151(1): 29–33. doi: <http://dx.doi.org/10.1016/j.cattod.2010.01.040>.
4. Ramirez AJ, Brain RA, Usenko S, *et al.* Occurrence of pharmaceuticals and personal care products in fish: Results of a national pilot study in the United States. *Environmental Toxicology and Chemistry* 2009; 28 (12): 2587–2597. doi: 10.1897/08-561.1.
5. Bu Q, Shi X, Yu G, *et al.* Pay attention to non-wastewater emission pathways of pharmaceuticals into environments. *Chemosphere* 2016; 165 (Supplement C): 515–518. doi: <https://doi.org/10.1016/j.chemosphere.2016.09.078>.
6. Puckowski A, Mioduszezowska K, Łukaszewicz P, *et al.* Bioaccumulation and analytics of pharmaceutical residues in the environment: A review. *Journal of Pharmaceutical and Biomedical Analysis* 2016; 127 (Supplement C): 232–255. doi: <https://doi.org/10.1016/j.jpba.2016.02.049>.
7. Menken M, Munsat TL, Toole JF. The global burden of disease study: Implications for neurology. *Archives of Neurology* 2000; 57(3): 418–420. doi: 10.1001/archneur.57.3.418.
8. Almeida N, Mari JD, Coutinho E, *et al.* Brazilian multicentric study of psychiatric morbidity — Methodological features and prevalence estimates. *British Journal of Psychiatry* 1997; 171: 524–529. doi: 10.1192/bjp.171.6.524.
9. Saraceno B. The WHO World Health Report 2001 on mental health. *Epidemiologia e Psichiatria Sociale* 2002; 11(2): 83–87. doi: 10.1017/s1121189x00005546.
10. Brooks BW, Turner PK, Stanley JK, *et al.* Waterborne and sediment toxicity of fluoxetine to select organisms. *Chemosphere* 2003; 52(1): 135–142. doi: [https://doi.org/10.1016/S0045-6535\(03\)00103-6](https://doi.org/10.1016/S0045-6535(03)00103-6).
11. Van der Ven K, Keil D, Moens LN, *et al.* Effects of the antidepressant mianserin in zebrafish: Molecular markers of endocrine disruption. *Chemosphere* 2006; 65(10): 1836–1845. doi: <https://doi.org/10.1016/j.chemosphere.2006.03.079>.
12. Escher BI, Bramaz N, Richter M, *et al.* Comparative ecotoxicological hazard assessment of beta-blockers and their human metabolites using a mode-of-action-based test battery and a QSAR approach. *Environmental Science & Technology* 2006; 40(23): 7402–7408. doi: 10.1021/es052572v.
13. Rosi-Marshall EJ, Snow D, Bartelt-Hunt SL, *et al.* A review of ecological effects and environmental fate of illicit drugs in aquatic ecosystems. *Journal of Hazardous Materials* 2015; 282: 18–25. doi: <https://doi.org/10.1016/j.jhazmat.2014.06.062>.
14. Thomas MA, Klaper RD. Psychoactive pharmaceuticals induce fish gene expression profiles associated with human idiopathic autism. *PLoS ONE* 2012; 7(6): e32917. doi: 10.1371/journal.pone.0032917.
15. Thomaidis NS, Gago-Ferrero P, Ort C, *et al.* Reflection of socioeconomic changes in wastewater: Licit and illicit drug use patterns. *Environmental Science & Technology* 2016; 50(18): 10065–10072. doi: 10.1021/acs.est.6b02417.
16. Rodayan A, Afana S, Segura PA, *et al.* Linking drugs of abuse in wastewater to contamination of surface and drinking water. *Environmental Toxicology and Chemistry* 2016; 35(4): 843–849. doi: 10.1002/etc.3085.
17. Chu S, Metcalfe CD. Analysis of paroxetine, fluoxetine and norfluoxetine in fish tissues using pressurized liquid extraction, mixed mode solid phase extraction cleanup and liquid chromatography — tandem mass spectrometry. *Journal of Chromatography A* 2007; 1163(1): 112–118. doi: <http://dx.doi.org/10.1016/j.chroma.2007.06.014>.
18. Tiedeken EJ, Tahar A, McHugh B, *et al.* Monitoring, sources, receptors, and control measures for three European Union watch list substances of emerging concern in receiving waters — A 20 year systematic review. *Science of the Total Environment* 2017; 574 (Supplement C): 1140–1163. doi: <https://doi.org/10.1016/j.scitotenv.2016.09.084>.
19. Barbosa MO, Moreira NFF, Ribeiro AR, *et al.* Occurrence and removal of organic micropollutants: An overview of the watch list of EU Decision 2015/495. *Water Research* 2016; 94 (Supplement C): 257–279. doi: <https://doi.org/10.1016/j.watres.2016.02.047>.
20. EU. European Union: Directive 2013/39/EU of the European Parliament and of the Council of 12 August 2013 amending Directives 2000/60/EC and 2008/105/EC as regards priority substances in the field of water policy. *Official Journal of the European Union* 2013; L226: 1–17.
21. Kelessidis A, Stasinakis AS. Comparative study of the methods used for treatment and final disposal of sewage sludge in European countries. *Waste Management* 2012; 32(6): 1186–1195. doi:

- <https://doi.org/10.1016/j.wasman.2012.01.012>.
22. Thakur M, Sharma G, Ahamad T, *et al.* Efficient photocatalytic degradation of toxic dyes from aqueous environment using gelatin-Zr(IV) phosphate nanocomposite and its antimicrobial activity. *Colloids and Surfaces B: Biointerfaces* 2017; 157 (Supplement C): 456–463. doi: <https://doi.org/10.1016/j.colsurfb.2017.06.018>.
 23. Bogatu C, Perniu D, Sau C, *et al.* Ultrasound assisted sol-gel TiO₂ powders and thin films for photocatalytic removal of toxic pollutants. *Ceramics International* 2017; 43(11): 7963–7969. doi: <https://doi.org/10.1016/j.ceramint.2017.03.054>.
 24. Braun AM, Maurette MT, Oliveros E. *Photochemical Technology*. Chichester: John Wiley & Sons Wiley; 1991.
 25. Sriwichai S, Ranwongsa H, Wetchakun K, *et al.* Effect of iron loading on the photocatalytic performance of Bi₂WO₆ photocatalyst. *Superlattices and Microstructures* 2014; 76 (Supplement C): 362–375. doi: <https://doi.org/10.1016/j.spmi.2014.10.014>.
 26. Tsoumachidou S, Velegraki T, Antoniadis A, *et al.* Greywater as a sustainable water source: A photocatalytic treatment technology under artificial and solar illumination. *Journal of Environmental Management* 2017; 195: 232–241. doi: [10.1016/j.jenvman.2016.08.025](https://doi.org/10.1016/j.jenvman.2016.08.025).
 27. Tsoumachidou S, Velegraki T, Poulivos I. TiO₂ photocatalytic degradation of UV filter para-aminobenzoic acid under artificial and solar illumination. *Journal of Chemical Technology and Biotechnology* 2016; 91 (6): 1773–1781. doi: [10.1002/jctb.4768](https://doi.org/10.1002/jctb.4768).
 28. Sakthivel S, Neppolian B, Shankar MV, *et al.* Solar photocatalytic degradation of azo dye: comparison of photocatalytic efficiency of ZnO and TiO₂. *Solar Energy Materials and Solar Cells* 2003; 77(1): 65–82. doi: [10.1016/S0927-0248\(02\)00255-6](https://doi.org/10.1016/S0927-0248(02)00255-6).
 29. Babuponnusami A, Muthukumar K. A review on Fenton and improvements to the Fenton process for wastewater treatment. *Journal of Environmental Chemical Engineering* 2014; 2 (1): 557–572. doi: <https://doi.org/10.1016/j.jece.2013.10.011>.
 30. Gaya UI, Abdullah AH. Heterogeneous photocatalytic degradation of organic contaminants over titanium dioxide: A review of fundamentals, progress and problems. *Journal of Photochemistry and Photobiology C: Photochemistry Reviews* 2008; 9(1): 1–12. doi: <https://doi.org/10.1016/j.jphotochemrev.2007.12.003>.
 31. Liu T, Li X, Yuan X, *et al.* Enhanced visible-light photocatalytic activity of a TiO₂ hydrosol mediated by H₂O₂: Surface complexation and kinetic modeling. *Journal of Molecular Catalysis A: Chemical* 2016; 414 (Supplement C): 122–129. doi: <https://doi.org/10.1016/j.molcata.2016.01.011>.
 32. Boroski M, Rodrigues AC, Garcia JC, *et al.* Combined electrocoagulation and TiO₂ photoassisted treatment applied to wastewater effluents from pharmaceutical and cosmetic industries. *Journal of Hazardous Materials* 2009; 162(1): 448–454. doi: <https://doi.org/10.1016/j.jhazmat.2008.05.062>.
 33. Rajeshwar K, Osugi ME, Chanmanee W, *et al.* Heterogeneous photocatalytic treatment of organic dyes in air and aqueous media. *Journal of Photochemistry and Photobiology C: Photochemistry Reviews* 2008; 9(4): 171–192. doi: <https://doi.org/10.1016/j.jphotochemrev.2008.09.001>.
 34. Rincón AG, Pulgarin C. Absence of E. coli regrowth after Fe³⁺ and TiO₂ solar photoassisted disinfection of water in CPC solar photoreactor. *Catalysis Today* 2007; 124(3): 204–214. doi: <http://dx.doi.org/10.1016/j.cattod.2007.03.039>.
 35. Nahar MS, Hasegawa K, Kagaya S, *et al.* Adsorption and aggregation of Fe(III)–hydroxy complexes during the photodegradation of phenol using the iron-added-TiO₂ combined system. *Journal of Hazardous Materials* 2009; 162(1): 351–355. doi: <http://dx.doi.org/10.1016/j.jhazmat.2008.05.046>.
 36. Měánková H, Maillhot G, Jirkovský J, *et al.* Effect of iron speciation on the photodegradation of Monuron in combined photocatalytic systems with immobilized or suspended TiO₂. *Environmental Chemistry Letters* 2009; 7(2): 127–132. doi: [10.1007/s10311-008-0145-2](https://doi.org/10.1007/s10311-008-0145-2).
 37. Mir NA, Haque MM, Khan A, *et al.* Photocatalytic degradation of herbicide Bentazone in aqueous suspension of TiO₂: Mineralization, identification of intermediates and reaction pathways. *Environmental Technology* 2014; 35(4): 407–415. doi: [10.1080/09593330.2013.829872](https://doi.org/10.1080/09593330.2013.829872).
 38. Lin Y, Ferronato C, Deng N, *et al.* Study of benzylparaben photocatalytic degradation by TiO₂. *Applied Catalysis B: Environmental* 2011; 104(3): 353–360. doi: <https://doi.org/10.1016/j.apcatb.2011.03.006>.
 39. Helali S, Dappozze F, Horikoshi S, *et al.* Kinetics of the photocatalytic degradation of methylamine: Influence of pH and UV-A/UV-B radiant fluxes. *Journal of Photochemistry and Photobiology A: Chemistry* 2013; 255 (Supplement C): 50–57. doi: <https://doi.org/10.1016/j.jphotochem.2012.12.022>.
 40. Tizaoui C, Mezughi K, Bickley R. Heterogeneous photocatalytic removal of the herbicide clopyralid and its comparison with UV/H₂O₂ and ozone oxidation techniques. *Desalination* 2011; 273(1): 197–204. doi: <https://doi.org/10.1016/j.desal.2010.11.036>.
 41. Ahmed S, Rasul MG, Martens WN, *et al.* Heterogeneous photocatalytic degradation of phenols in wastewater: A review on current status and developments. *Desalination* 2010; 261(1-2): 3–18. doi: [10.1016/j.desal.2010.04.062](https://doi.org/10.1016/j.desal.2010.04.062).
 42. Datar PA, Waghmare RU. Development and validation of an analytical method for the stability of duloxetine hydrochloride. *Journal of Taibah University for Science* 2014; 8(4): 357–63. doi: <https://doi.org/10.1016/j.jtusc.2014.06.001>.
 43. Sinha VR, Kumria AR, Bhinge JR. Stress Degradation Studies on Duloxetine Hydrochloride and De-

- velopment of an RP-HPLC Method for its Determination in Capsule Formulation. *Journal of Chromatographic Science* 2009; 47(7): 589–593.
44. Carneiro PA, Nogueira RFP, Zanoni MVB. Homogeneous photodegradation of CI Reactive Blue 4 using a photo-Fenton process under artificial and solar irradiation. *Dyes and Pigments* 2007; 74(1): 127–132. doi: 10.1016/j.dyepig.2006.01.022.
 45. Baba Y, Yatagai T, Harada T, *et al.* Hydroxyl radical generation in the photo-Fenton process: Effects of carboxylic acids on iron redox cycling. *Chemical Engineering Journal* 2015; 277: 229–241. doi: 10.1016/j.cej.2015.04.103.
 46. Mirzaei A, Chen Z, Haghghat F, *et al.* Removal of pharmaceuticals from water by homo/heterogenous Fenton-type processes — A review. *Chemosphere* 2017; 174 (Supplement C): 665–688. doi: <https://doi.org/10.1016/j.chemosphere.2017.02.019>.
 47. Abdessalem AK, Bellakhal N, Oturan N, *et al.* Treatment of a mixture of three pesticides by photo- and electro-Fenton processes. *Desalination* 2010; 250 (1): 450–455. doi: 10.1016/j.desal.2009.09.072.
 48. Tsoumachidou S, Lambropoulou D, Poullos I. Homogeneous photocatalytic oxidation of UV filter para-aminobenzoic acid in aqueous solutions. *Environmental Science and Pollution Research* 2017; 24 (2): 1113–1121. doi: 10.1007/s11356-016-7434-2.
 49. Malato S, Fernandez-Ibanez P, Maldonado MI, *et al.* Decontamination and disinfection of water by solar photocatalysis: Recent overview and trends. *Catalysis Today* 2009; 147(1): 1–59. doi: 10.1016/j.cattod.2009.06.018.
 50. Xu X, Li X, Li X, *et al.* Degradation of melatonin by UV, UV/H₂O₂, Fe²⁺/H₂O₂ and UV/Fe²⁺/H₂O₂ processes. *Separation and Purification Technology* 2009; 68(2): 261–266. doi: 10.1016/j.seppur.2009.05.013.
 51. Ioannou LA, Fatta-Kassinos D. Solar photo-Fenton oxidation against the bioresistant fractions of winery wastewater. *Journal of Environmental Chemical Engineering* 2013; (1): 703–712.
 52. Gernjak W, Krutzler T, Glaser A, *et al.* Photo-Fenton treatment of water containing natural-phenolic pollutants. *Chemosphere* 2003; 50(1): 71–78. doi: 10.1016/S0045-6535(02)00403-4.
 53. Yang M, Hu J, Ito K. Characteristics of Fe²⁺/H₂O₂/UV oxidization process. *Environmental Technology* 1998; 19(2): 183–191. doi: 10.1080/09593331908616670.
 54. Navarro S, Fenoll J, Vela N, *et al.* Removal of ten pesticides from leaching water at pilot plant scale by photo-Fenton treatment. *Chemical Engineering Journal* 2011; 167(1): 42–49. doi: 10.1016/j.cej.2010.11.105.
 55. Doumic LI, Soares PA, Ayude MA, *et al.* Enhancement of a solar photo-Fenton reaction by using ferrioxalate complexes for the treatment of a synthetic cotton-textile dyeing wastewater. *Chemical Engineering Journal* 2015; 277: 86–96. doi: 10.1016/j.cej.2015.04.074.
 56. Nohara K, Hidaka H, Pelizzetti Z, *et al.* Processes of formation of NH₄⁺ and NO₃⁻ ions during the photocatalyzed oxidation of N-containing compounds at the titania/water interface. *Journal of Photochemistry and Photobiology A: Chemistry* 1997; 102(2): 265–272. doi: [https://doi.org/10.1016/S1010-6030\(96\)04478-4](https://doi.org/10.1016/S1010-6030(96)04478-4).
 57. Pignatello JJ, Oliveros E, MacKay A. Advanced oxidation processes for organic contaminant destruction based on the Fenton reaction and related chemistry. *Critical Reviews in Environmental Science and Technology* 2006; 36(1): 1–84. doi: 10.1080/10643380500326564.

ORIGINAL RESEARCH ARTICLE

Copper and lead ions removal from aqueous solution using MgO, nanostructured MgO

Salah N. Farhan*, Anees Abdullah Khadom, Abdul Mun'em Abbas Karim

University of Daiyla, Iraq. E-mail: drsalahchem@gmail.com

ABSTRACT

This study investigated elimination of Cu^{+2} and Pb_2^{+2} from prepared stock solutions using MgO, nanostructured MgO sorbents. The maximum cumulative values for copper and lead were 410, 200, 494.9, and 214.6 $\text{mg}\cdot\text{g}^{-1}$, for Nanostructured MgO, MgO, respectively. Freundlich and Langmuir models describe the sorption equilibrium isotherms. Freundlich model gives the best interpretation for experiment data for these ions.

The most adequate model describing the kinetic with the experimental data using MgO, Nanostructured MgO was a first-order kinetic model. Nanostructured MgO probably has an efficient way to remove metal ions due to its high capability to adsorb these ions.

Keywords: Heavy Metals; Nanoparticles; Peanut Peels

ARTICLE INFO

Received 1 April 2020
Accepted 21 May 2020
Available online 28 May 2020

COPYRIGHT

Copyright © 2020 Salah N. Farhan, *et al.*
EnPress Publisher LLC. This work is
licensed under the Creative Commons
Attribution-NonCommercial 4.0
International License (CC BY-NC 4.0).
<https://creativecommons.org/licenses/by-nc/4.0/>

1. Introduction

Uncontrolled release of metal particles turns into a noteworthy issue. These metal ions tend to accumulate either by bioconcentration, bioaccumulation, or biomagnifications through soil, and water, constant exposure of human to these metals leads to a significant risk^[1-3]. Heavy metals in wastewater can have detrimental effects on all forms of life when discharged directly into the environment^[4].

As a result, the way to correctly and effectively remove unwanted metals from eco structures is still essential but nonetheless challenging assignment for environmental safety engineers. In recent times, several strategies had been suggested for elimination of heavy metal from wastewaters, inclusive of however no longer limited to membrane filtration, precipitation, and other known techniques^[5-8].

Amongst heavy metals, Pb^{+2} , Cu^{+2} , are most of the fundamental pollutants for environment, which might be leaked to soil and eco systems via fertilizers, insecticides, biosolids, metallic mining and milling procedures, consumed commercial wastes, and airborne resources^[9].

The high surface area provided by nanoparticles in addition to the amount of pores present, and diversity of surface active groups, making nanoparticles have large capacity with selective metal in elimination of these ions^[10,11].

(NMOs) show high ability to selective adsorb with high potential, as a result of that, adequate elimination of poisonous ions might be expected to fulfill more and more strict policies^[12]. Size of NMOs in the range of nano scale causing negative stability.

Eventually, NMOs are liable to aggregation and tendency to take different interactions under the effect of some forces such as Van der Waals^[13], causing decreasing in potential of NMOs and selectivity or even vanished. In addition, aggregation of NMOs in any type of flow causes pressure drop consequently unstability. To enhance efficiency had been then spread through supports of high porosity to get composite absorbing materials^[14]. Activated carbon, natural materials, artificial polymeric hosts are widely used for porous supports.

Those sorbents were tested in batch manner for elimination of Pb⁺², and Cu⁺² existing in prepared solutions. Experimental facts received during batch equilibrium runs were analysed using Langmuir and Freundlich isotherm models. Kinetic investigations were done by two kinetic models, pseudo-first-order, and pseudo-second order. Alternatively, the outcomes of numerous parameters along with solution pH, contact time, and adsorption isotherm, at the sorbents have been studied.

2. Material and methods

2.1 Chemicals

Solutions of metal ions were prepared from their (Merck, Germany). Structure, nanostructured MgO were purchased (purity, 99.5%) from Nabond (China). Varian Spectra AA 220 atomic absorption spectrophotometer was used to conduct analysis.

2.2 Peanut peels preparation

Peanut Peels was rinsed in distilled deionized water then heated at 100 °C for one day in order to get low moisture content. They have been then grinding by home mill and sieved. To leach out active functional groups from Peanut Peels with diameters less than 100 mesh (passed through 100 standard sieves) rinsed in 0.1 N HNO₃ in the ratio of 1 tog to 10 mL for 20 h at 80 °C then, centrifuged with adjusting its pH to 5. After that use a 0.45 μm filter membrane (Sartorius Company) to filtered solution, cooled and stored at 4 °C prior to use.

2.3 Adsorption analysis

Adsorption capacity and Kinetic experiments were carried out in conical flasks 100 mL with 0.05 g (2 g/L) of MgO, and nanostructured MgO with 50

mL of 50 mg/L metal ion solutions without changing pH value. The mixtures were shaken (1000 rpm) at 25 °C. Separation of solid from liquid were done using centrifugal working at (2000 rpm) After that the used samples have been filtered by 0.42 μm filter membrane (Sartorius, Germany). Atomic absorption spectroscopy was used to analyze concentration of metal ions. It was documented that the ratio of removal metal ions has been calculated as:

$$\% \text{removal} = \left(\frac{C_0 - C_e}{C_0} \right) * 100 \quad (1)$$

where C₀ and C_e denotes to primary and final concentrations of metals in the liquid phase. Each experiment was repeated twice and the mean value was taken as a final result used.

2.4 pH effect

By adding 0.1 N NaOH or 0.1 N HNO₃ to the solution, pH was adjusted in a range from 2 to 7, and all other variables are fixed.

2.5 Contact time

Batch mode experiments were done for flasks with different times of 10, 20, 40, 60, 90, 120, 180, and 1440 min, with no change of other variables.

In order to investigate the kinetic model has been used here in this study.

2.6 Kinetics study

In order to investigate the mechanism and rate of the metal adsorption process, kinetic models has been in this study, linearization of first order equations^[15], pseudo-first order^[11-18] and pseudo-second order^[16,19].

The first-order model is:

$$\ln(q_0 - q_t) = a - b \quad (2)$$

where q_t is the cumulative amount of the metal ions adsorbed at time t, q₀ is the maximum of the metal ions adsorbed, and a (mg·g⁻¹ min⁻¹) and b (mg·g⁻¹)⁻¹ are constants. An important term in these equations is the constant b, which indicates the metal adsorption rate.

The model of pseudo-first-order kinetic is given as:

$$\log(q_e - q_t) = \log q_e - b \left(\frac{k_1}{2.303} \right) t \quad (3)$$

where q_e denotes to the amounts of the ions adsorbed on the adsorbent in $\text{mg}\cdot\text{g}^{-1}$ at equilibrium and q_t denote the same manner at any time, t , while K_1 is first-order equation constant .

The pseudo-second-order kinetic model of is given as:

$$\frac{1}{q_t} = \frac{1}{K_2 q_e^2} + \frac{t}{q_e} \quad (4)$$

where K_2 is the rate constant in $\text{g}\cdot\text{mg}^{-1}\cdot\text{min}^{-1}$.

2.7 Adsorbent dosage

Experiments were conducted in a batch mode by mixing different adsorbents weight of 0.05, 0.1, 1, 2, 3, and 4 $\text{g}\cdot\text{L}^{-1}$, with no change of other variables.

2.8 Adsorption isotherms

To conduct adsorption isotherm, experiments were carried out with 0.05 g nano structured materials with different initial concentrations of Cu^{+2} , and Pb^{+2} in solutions at (0, 10, 20, 30, 60, 100, and 200, $\text{mg}\cdot\text{L}^{-1}$) at 25 °C.

Freundlich equation is used to describe the heterogeneity of the surface of the absorbent material and it is represented by:

$$\log q_e = \log K_F + \frac{1}{n} \log C_e \quad (5)$$

The adsorption capacity ($\text{mg}\cdot\text{g}^{-1}$) represent by k_f which is also known as Freundlich constant, while adsorption intensity represent by a constant n (dimensionless). If n within the domain $n \leq 1$, that's indicates unfavorably adsorption , and if $1 < n < 10$ that will gives favorable adsorption. If we assumed that the adsorbent medium is a structurally homogeneous, the Langmuir equation is based, as:

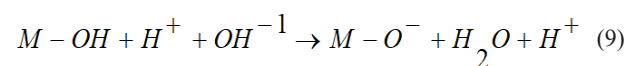
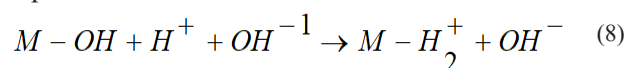
$$\frac{C_e}{q_e} = \frac{C_e}{q_0} + \frac{1}{q_0 b} \quad (6)$$

Weight of adsorbed over weight of adsorbent equilibrium is q_e ($\text{mg}\cdot\text{g}^{-1}$), while C_e is solution concentration at equilibrium ($\text{mg}\cdot\text{L}^{-1}$), q_0 (q_{max}) is the maximum adsorption when monolayer coverage ($\text{mg}\cdot\text{g}^{-1}$) is assumed, and b (K_L) is a constant correlates adsorption energy that quantitatively reflects affinity bonding sites ($\text{L}\cdot\text{mg}^{-1}$).

3. Results and discussion

3.1 Initial pH effect

Figure 1 shows the effect of the acidic scale pH on the adsorption process. Acidic conditions are associated with the lowering of adsorption of metal. The reason for that is attributed to the protonation of functional groups. In general, chemical adsorption occurs easily on the surface of oxides. Were hydroxyl groups is finally covered the surface layer, but, in the case of MgO , the chemical adsorption of OH extends to the inside of the solid. These hydroxyls (functional groups) can receive and release protons to the water, accordingly, surface charge will be positive or negative, as shown in the following equations^[20]:



Acidity of particle surface is strong while solvent is basic. Therefore the surface will carry a negative charge by giving its proton to solvent. On the contrary, basicity of the particle surface is strong, acidic solvent, due to particles received proton from solvent^[20].

MgO has high pH of zero point charge (pH_{zpc}), high basic nature, and acidic stock solution (pH between 4.5–6.0 before equilibrium), therefore, Equation (8) is the dominant mechanism.

Thus, OH^- can precipitate some heavy metals in hydroxide forms while increasing pH up to 10–10.4 (equilibrium pH after 1440 min) can increase negative pH-dependent charge in MgO and increase electrostatic sorption.

At low pH, nanostructured MgO binding sites

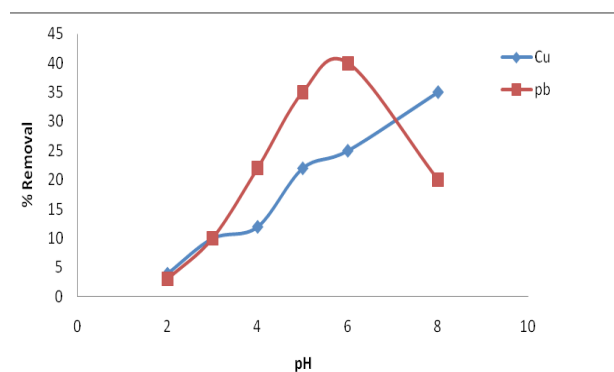


Figure 1. Effect of pH on sorption of metal ions, reaction volume = 50 mL, adsorbent weight = 0.1 g, $C_0 = 10 \text{ mg/L}$.

were dominated by H ions leading to protonate functional groups. Active sites decreased with increasing the protonated metal-binding adsorbent groups. Competing effect of H ions decreased as pH increased, giving an increasing of heavy metal ion adsorption onto the adsorbent^[21].

However, in both of these adsorbents the adsorption suddenly increased at pH > 6 in some cases. This rapid increase may be attributed to metal complexes formation or precipitation^[22].

The amount of removal was always high (removal of tow metals >90%). Therefore, the native pH of all solutions (pH = 5) was considered to be the optimum value for all adsorbents and metals.

3.2 Effects of dosage of adsorbent

Figure 2 shows the effect of nanoparticle dose. Adsorption of heavy metals was studied after a 24 h contact time with an initial heavy metal concentration of 100 mg L⁻¹. Dosage increase starting at 0.5 to 3 gL⁻¹ resulting an increase in the removal capacity of Cu²⁺ and Pb²⁺.

However, this was not always the case, over-

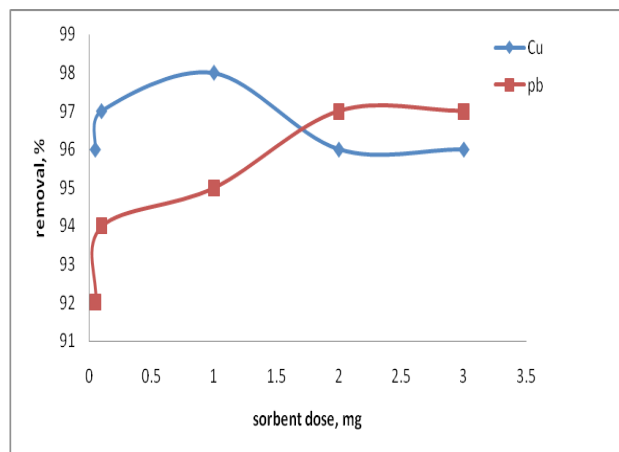


Figure 2. Effect of sorbent dose on biosorption of metal ions, reaction volume = 50 mL, pH = 5.5, C₀ = 50 mg/L.

lapping active sites at higher dosages could decrease heavy metal adsorption. Decreased effective surface area results from conglomeration of exchange particles^[19]. Maximum removal efficiency of Cu⁺² and Pb⁺², is 90 %, and 95%, respectively.

3.3 Contact time effect

Removal of heavy metal increased with time at native pH, Figure 3 indicates that adsorption reached a maximum value after 40 to 80 min. After that period there is no change in the efficiency of the removal process. Table 1 shows rate equations and related constants.

3.4 Kinetic and isotherme

Table 2 and Table 3 give the Langmuir and Freundlich parameters which indicates that Langmuir give best fitting with experimental data. Figures 4, 5 show the Lagergren first order and Hoes second order models, it can be seen that Lagergren model give best fitting.

4. Conclusion

Here, in the current study the results showed

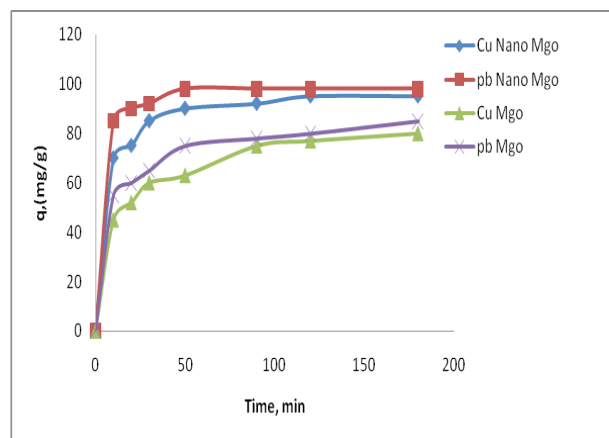


Figure 3. Effect of contact time on sorption of metal ions, reaction volume = 100 mL, adsorbent weight = 0.1 g.

Table 1. First-order kinetics model constants (at concentration of 50 mg/L)

C ₀ = 100 mg/L	MgO			Nanostructured MgO		
	a (mg·g ⁻¹ ·min ⁻¹)	b (mg·g ⁻¹) ⁻¹	R ²	a	b	R ²
Ions						
Cu ²	-0.0041	1.492	0.979	-0.27	3.53	0.981
Pb ²	-0.0048	1.282	0.978	-0.28	6.25	0.995

that the process of adsorption affected by several factors, such as pH, contact time, and concentration, the most important results suggest that the process of adsorption depends heavily on the scale of acidity and showed the study of kinetics that adsorption follows the interaction of the second order equation and the best model simulates the results is Langmuir model. Nanoparticles can be used after being restricted with a certain medium to conduct adsorption of heavy metals from water.

Conflict of interest

The authors declare that they have no conflict of interest.

Acknowledgements

Financial support from the laboratories of Chemical Engineering Department, College of Engineering, University of Diyala to this project is highly appreciated.

References

1. Xin X, Wei Q, Yang J, *et al.* Highly efficient removal of heavy metal ion by amine functionalized mesoporous Fe₃O₄ nanoparticles. *Chemical Engineering Journal* 2012; 184: 132–140.
2. Farhan SN. Biosorption of Hg and Ni ions on Bakers Yeast. *Diyala Journal of Pure Science* 2010; 6(1): 157–173.

Table 2. Langmuir and Freundlich parameters of lead ions at different initial concentrations

Lead Ions conce. (mg/L)	Langmuir parameters			Freundlich parameters		
	q _m (mg/g)	b (l/mg)	R ²	K (l/mg)	n	R ²
98	105.69	8.2	0.8605	51.11	32.05	0.8455
57.67	62.24	17.44	0.8862	41.81	53.47	0.8522
20.34	21.32	6.54	0.9591	8.92	26.738	0.9263

Table 3. Langmuir and Freundlich parameters of copper ions at different initial concentrations

Copper Ions conce. (mg/L)	Langmuir parameters			Freundlich parameters		
	q _m (mg/g)	b (l/mg)	R ²	K (l/mg)	n	R ²
93.59	42.32	7.72	0.7833	16.46	28.7	0.778
59.37	23.1	11.17	0.8833	20.00	24.71	0.7915
19.62	9.88	22.90	0.967	7.41	65.22	0.9069

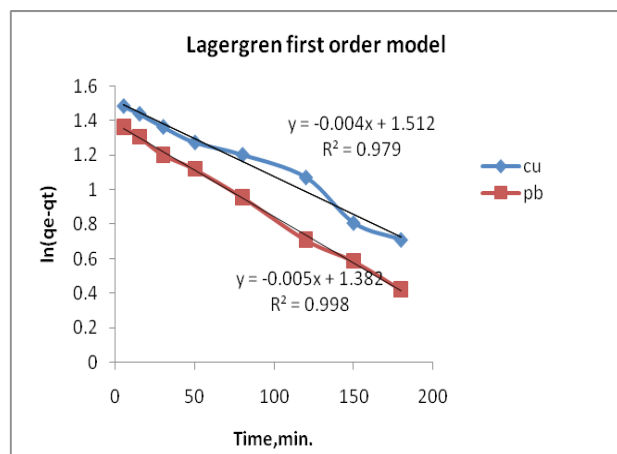


Figure 4. Lagergren first order model for copper and lead.

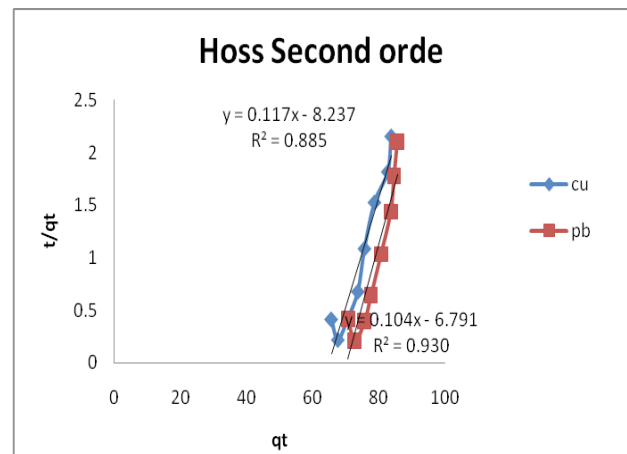


Figure 5. Hoss second order model for copper and lead.

3. Farhan SN, Khadom AA. Biosorption of heavy metals from aqueous solutions by *Saccharomyces Cerevisiae*. *International Journal of Industrial Chemistry* 2015; 6: 119–130.
4. Heidari A, Younesi H, Mehraban Z. Removal of Ni (II), Cd (II), and Pb (II) from a ternary aqueous solution by amino functionalized mesoporous and nano mesoporous silica. *Chemical Engineering Journal* 2009; 153: 70–79.
5. Xing S, Meiqing, Zhao Z. Removal of heavy metal ions from aqueous solution using red loess as an adsorbent. *Journal of Environmental Sciences* 2011; 23(9): 1497–1502.
6. Lee BG, Roger M. Rowell Removal of heavy metal ions from aqueous solutions using lignocellulosic fibers. *Journal of Natural Fibers* 2004; 1(1).
7. Pawlowski L. *Physicochemical methods for water and waste water treatment*. 1982 Volume 19 1st Edition, eBook ISBN: 9780080874784.
8. Fu FL, Wang Q. Removal of heavy metal ions from wastewaters: A review. *Journal of Environmental Management* 2011; 92: 407–418.
9. Ali I, Asim M, Khan TA. Low cost adsorbents for the removal of organic pollutants from wastewater. *Journal of Environmental Management* 2012; 113: 170–183.
10. Chen Q, Yin D, Zhu S, *et al.* Adsorption of cadmium (II) on humic acid coated titanium dioxide. *Journal of Colloid and Interface Science* 2012; 367: 241–248.
11. Hua M, Zhang S, Pan B, *et al.* Heavy metal removal from water/wastewater by nanosized metal oxides: A review. *Journal of Hazardous Materials* 2012; 211–212: 317–331.
12. Limousin G, Gaudet JP, Charlet L, *et al.* Sorption isotherms: A review on physical bases, modeling and measurement. *Applied Geochemistry* 2007; 22(2): 249–275.
13. Pradeep T, Anshup. Noble metal nanoparticles for water purification: A critical review. *Thin Solid Films* 2009; 517: 6441–6478.
14. Pan BJ, Pan BC, Zhang WM, *et al.* Development of polymeric and polymer-based hybrid adsorbents for pollutants removal from waters. *Chemical Engineering Journal* 2009; 151: 19–29.
15. Jalali M. Effect of sodium and magnesium on kinetics of potassium release in some calcareous soils of Western Iran. *Geoderma* 2008; 145: 207–215.
16. Ho YS. Review of second-order models for adsorption systems. *Journal of Hazardous Materials* 2006; 136: 681–689.
17. Zhou YT, White CB, Nie HL, *et al.* Adsorption mechanism of Cu²⁺ from solution by chitosan-coated magnetic nanoparticles modified with α -ketoglutaric acid. *Colloids and Surfaces B: Biointerfaces* 2009; 74: 244–252.
18. Yang W, Kan AT, Chen W, *et al.* pH-dependent effect of zinc on arsenic adsorption to magnetite nanoparticles. *Water Research* 2010; 44: 5693–5701.
19. Rahmani A, Mosavi HZ, Fazli M. Effect of nanostructure alumina on adsorption of heavy metals. *Desalination* 2010; 253L: 94–100.
20. Hosokawa M, Nogi K, Naito MT, *et al.* *Nanoparticle technology handbook*. Oxford, UK: Elsevier; 2007.
21. Afkhami A, Moosavi R. Adsorptive removal of Congo red, a carcinogenic textile dye, from aqueous solutions by maghemite nanoparticles. *Journal of Hazardous Materials* 2010; 174: 398–403.
22. Rashidi F, Sarabi RS, Ghasemi Z, *et al.* Kinetic, equilibrium and thermodynamic studies for the removal of lead (II) and copper (II) ions from aqueous solutions by nanocrystalline TiO₂. *Superlattices and Microstructures* 2010; 48: 577–591.

ORIGINAL RESEARCH ARTICLE

Kinetics of dechlorination of atrazine using tin (SnII) at neutral pH conditions

Vijay Kumar¹, Simranjeet Singh²

¹Regional Ayurveda Research Institute for Drug Development, Gwalior, India. E-mail: vijaychem99@gmail.com

²Department of Biotechnology, Lovely Professional University, Punjab, India.

ABSTRACT

Atrazine is a broad spectrum herbicide of triazine family. It is a chlorine-containing molecule and it can persist in environment. Chemical and biochemical techniques are the main techniques used to decompose the chemicals. In pre-sent study, the dechlorination of atrazine (Atr) via reaction with Sn(II) ion under aqueous media at neutral pH conditions was studied. The observed dechlorinated metabolite was 4-Ethylamino-6-isopropylamino-[1,3,5]triazin-2-ol. Identification of dechlorinated product of Atr was performed by using spectroscopic (FTIR) and mass (ESI-MS) spectrometric analysis. The kinetics of the dechlorination of Atr was measured by using pseudo-first order kinetics. The observed reaction constants was, $k_{obs} = 6.11 \times 10^{-2}$ (at 430 mg/L of Atr), and $k_{obs} = 6.14 \times 10^{-2}$ (at 215 mg/L of Atr). The calculated half-life ($t_{1/2}$) period was, $t_{1/2} = 0.204$ d (at 430 mg/L of Atr), and $t_{1/2} = 0.205$ d (at 215 mg/L of Atr).

Keywords: Atrazine; Dechlorination; Decomposition; IR Analysis; Mass Analysis

ARTICLE INFO

Received 4 April 2020
Accepted 17 May 2020
Available online 23 May 2020

COPYRIGHT

Copyright © 2020 Vijay Kumar, *et al.*
EnPress Publisher LLC. This work is
licensed under the Creative Commons
Attribution-NonCommercial 4.0
International License (CC BY-NC 4.0).
<https://creativecommons.org/licenses/by-nc/4.0/>

1. Introduction

2-chloro-N⁴-N⁶-isopropyl-1,3,5-triazine-4,6-diamine or atrazine (Atr) is a broad spectrum herbicide^[1-8]. It inhibits photosynthesis and interferes with other enzymatic processes of weeds. It is the member of triazine family, and it is still used in about 90 countries all over the world^[5-12]. Annual use of atrazine was estimated to be 80,000 tons worldwide. As a chlorinated molecule, Atr is the big concern for environmental studies. Atr has low volatility, low solubility in water (33 mg/L) and low half life of 244 d through hydrolysis^[17]. Transport of pesticides in environment depends upon their electrical potentials, adsorption and complex-formation abilities^[13-22]. Atr previously has been the theme of dechlorination by using of zero valent metal ions and theoretical metal complex studies^[16-24].

In literature, extensive analysis on dechlorination of chlorinated compounds through zero valent metals has been reported^[21-28]. All the studies have demonstrated that dechlorination process enhanced at low pH values from 2 to 5, where, zero-valent metal ions get oxidized^[24-29]. In the literature, there are detailed studies about the dechlorination of various organic compounds and atrazine have been reported^[5-15]. In recent studies, the reported degradation products of atrazine were 2-ethylamino-4-isopropylamino-1,3,5-triazine, hydroxyatrazine (2-ethylamino-4-isopropylamino-6-hydroxy-s-triazine) and 2,4-bis(ethylamine)-6-methyl-s-triazine^[11-28]. None of the above mentioned degradation

product was identified prominently in current study. In current study, dechlorination of Atr was achieved by using least toxic Sn(II) metal ion. As per our best information, no study on current topic is reported in literature. Current study is more important because of its environmental acceptability, as it was performed in aqueous media and at neutral pH conditions.

2. Experimental

All the chemicals used were of analytical reagent grade. The dechlorination/decomposition reactions were performed as per the procedure described below. The FTIR spectrums of dechlorinated product and Atr were taken in potassium bromide (KBr) discs. All spectrums were recorded on a Shimadzu-8400s FTIR spectrophotometer. Mass (ESI-MS) analyses of all the samples (dechlorinated product and Atr) were performed on mass spectrophotometer (Wa-ters, Q-TOF Micromass).

Aqueous solution (100 mL) of metal salts (1 mM; 225 mg/L) was added to ethanolic solution (100 mL) of atrazine (2 mM; 430 mg/L). The pH of reaction mixture was adjusted at 7 ± 0.5 using NaOH solution. Similarly 1:1 reaction was performed by adding the aqueous solution (100 mL) of metal salts (1 mM; 225 mg/L) being added to ethanolic solution (100 mL) of atrazine (1 mM; 215 mg/L). The resulting solution was stirred for 10 h at 150 rpm on a magnetic stirrer at temperature of 25 ± 0.5 °C.

At regular time intervals (0 h, 1 h, 2 h, 3 h, 4 h, 6 h, 8 h and 10 h) 20 mL of reaction mixture was taken off and organic material was extracted by using ethyl-acetate as extracting solvent. Excess ethyl-acetate was evaporated on vacuumed Rotavapor. To analyze the changes w.r.t. parent molecule (Atr), FTIR and mass analyses of well dried extracted organic material were performed.

The rate of dechlorination of atrazine by Sn(II) was analyzed according to pseudo-first order kinetics. Equations (1)–(3) correspond to the equations of the concentration variation with time was plotted on the basis of the linear regression results obtained by plotting Time (in h) Vs Log C_t (in mg/L).

$$d[C]/dt = -k_{\text{obs}}[C] \quad (1)$$

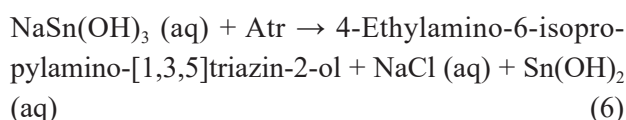
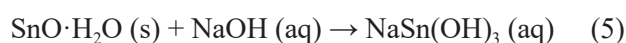
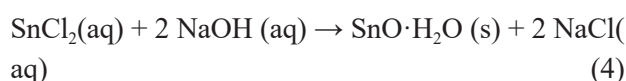
$$\log[C]/[C]_0 = k_{\text{obs}}t \quad (2)$$

$$t_{1/2} = (1/k_{\text{obs}}) \times \log 2 \quad (3)$$

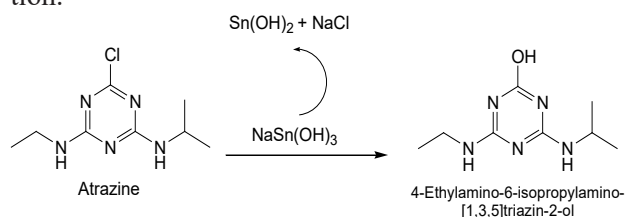
Where, $[C]$ is the atrazine concentration at time t (mg/L); $[C]_0$ the initial atrazine concentration (mg/L); k_{obs} is the pseudo-first order constant (h^{-1}).

3. Result and discussion

In current study, the mode/mechanism of dechlorinated is explained through following reactions from equations (4)–(6) and under Scheme-1. In equation (6), one mole of each, 4-Ethylamino-6-isopropylamino-[1,3,5]triazin-2-ol, NaCl and $\text{Sn}(\text{OH})_2$ was produced via the interactions of one mole of each, Atr and $\text{NaSn}(\text{OH})_3$. Equations (4)–(6) have revealed that under neutral to basic pH conditions, dechlorination reaction rate of Atr is independent of concentration of Atr, but linearly dependent of concentration of SnCl_2 ^[14,22].



The reaction kinetics of dechlorination of was measured by using pseudo-first order kinetic as mentioned in literature^[12–17]. The concentration of SnCl_2 was kept constant and concentration of Atr was varied. Mass analysis revealed that at molar ratios 1:2 or 1:1 of Sn(II) to Atr, approximately 70–75% decomposition was achieved after 10 h reaction.



Scheme 1. Schematic representation of dechlorination of atrazine in the presence of Sn under aqueous medium at pH 7.

The observed reaction constants was, $k_{\text{obs}} = 6.11 \times 10^{-2}$ with $R^2 = 0.99$ (at 430 mg/L of Atr), and $k_{\text{obs}} = 6.14 \times 10^{-2}$ with $R^2 = 0.99$ (at 215 mg/L of Atr) (**Figure 1** and **Figure 2**). The calculated half-life ($t_{1/2}$) period was, $t_{1/2} = 0.204$ d (at 430 mg/L of Atr), and $t_{1/2} = 0.205$ d (at 215 mg/L of Atr). The observed reaction rates were similar at both ratios (**Figure 2** and **Figure 3**). These values were considerably smaller than the value reported in the litera-

ture^[12,17]. Dombek *et al.* have performed dechlorination via using zero valent metallic iron under acidic conditions (pH values of 2.0, 3.0, and 3.8), the observed half-lives of atrazine were 0.06 d at pH value of 2.0, 5.12 d at pH value of 3.0, and 10.36 d at pH value of 3.8^[12]. Similarly, Kim *et al.* have performed dechlorination via using zero valent metallic iron under neutral pH conditions, the observed half-lives of atrazine were 8.91 d at 10 mg/L, 9.32 d at 30 mg/L, and 10.00 d at 50 mg/L^[17].

Mass (ESI-MS) and FTIR analyses were used to identify the dechlorination of atrazine (**Figure 3**). In current study, the parent ion of degradation product has a mass/charge ratio of 198, corresponding to 4-Ethylamino-6-isopropylamino-[1,3,5]triazin-2-ol (**Figure 3**). It is possible only due to replacement of Cl with OH ($215 - 35 + 18$ or $215 - 17 = 198$) (**Figure 1**). The lack of isotopic ratio as like mass/charge ratio of 216, no isotopic ratio was observed at 198, confirming the absence of chlorine with molecule^[28-32].

The comparative IR spectrums of Atr and its dechlorinated products have shown the sharp appearance in the stretching band of the $\nu(\text{OH})$ at 3450 cm^{-1} , and sharp disappearance of C-Cl band 660 cm^{-1} ^[37-39]. FTIR and mass analysis have revealed that the dechlorinated product of atrazine was 4-Ethylamino-6-isopropylamino-[1,3,5]triazin-2-ol having m/z 198 with 100% intensity (Figure

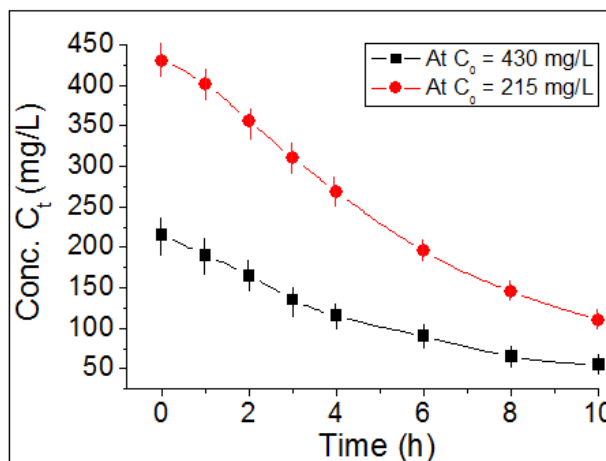


Figure 1. Dechlorination of Atr w.r.t. initial concentrations (C_0 at 430 and 215 mg/L) with time.

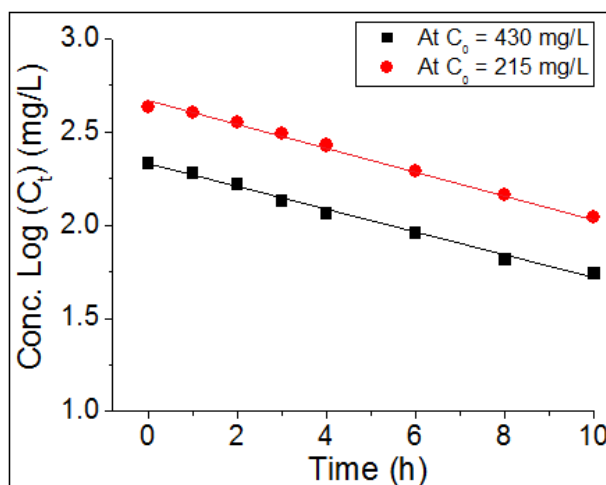


Figure 2. Pseudo-first order kinetics of dechlorination of Atr w.r.t. initial concentrations ($\text{Log } C_t$ at 430 and 215 mg/L).

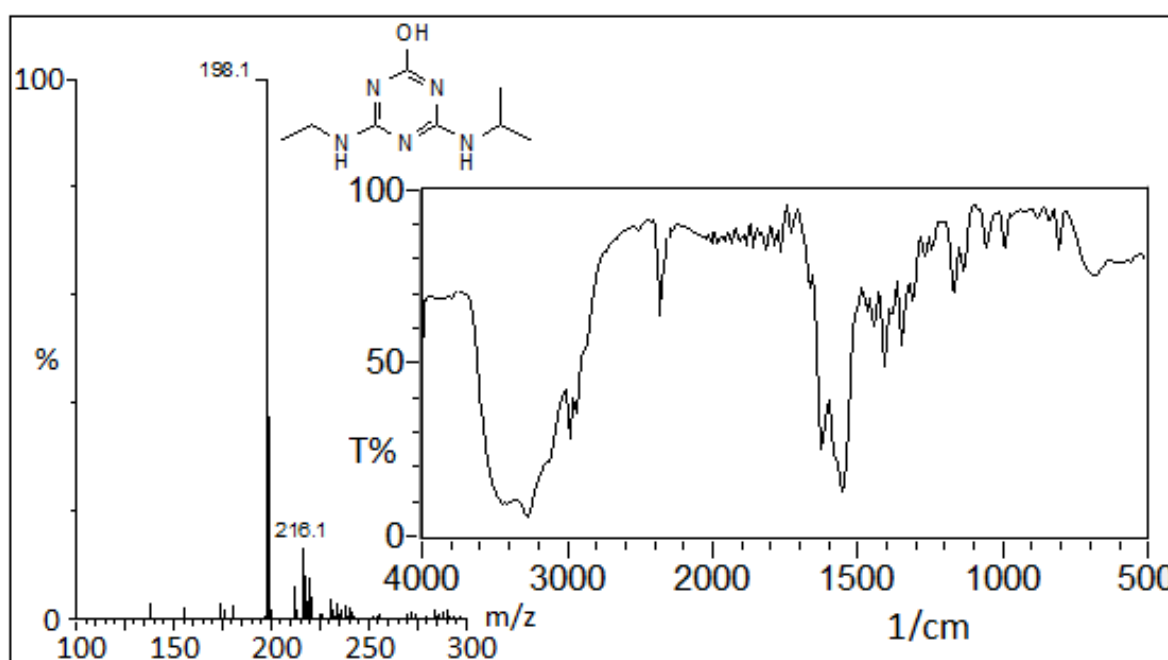


Figure 3. Mass (ESI-MS) and FTIR analysis of dechlorinated product of Atr after 10 h at 430 mg/L of Atr.

3). The observed dechlorinated product of atrazine was quite differ than the reported metabolites^[33–42].

4. Conclusion

In summary, large number of aquatic, soil, agricultural and geological material/organisms survive under neutral to basic conditions. In current study the objective of dechlorination of toxic Atr at neutral conditions was achieved successfully. Dechlorination followed pseudo-first order kinetics with reaction constant $k_{\text{obs}} = 6.12 \pm 2 \times 10^{-2}$, and half-life period, $t_{1/2} = 0.204 \pm 0.001$ d. In future, we will use agricultural and geological material to check the dechlorination kinetics of Atr at neutral pH with the addition of variable concentrations of SnCl_2 .

Conflict of interest

The authors declare that they have no conflict of interest.

Acknowledgements

We are thankful to UGC, India, for its financial support. Also, authors are extremely thankful to Gautmi Ltd Hyderabad (India) for providing OPs, Lovely Professional University for infrastructural as well as instrumental support and SAIF Punjab University Chandigarh, SAIF IIT Madras as well as SAIF Kerala University Kochi for providing the instrumental support.

References

1. Chan KH, Chu W. Model applications and mechanism study on the degradation of atrazine by Fenton's system. *Journal of Hazardous Materials Journal of Hazardous Materials* 2005; 118: 227–237.
2. Chen H, Bramanti E, Longo I, *et al.* Oxidative decomposition of atrazine in water in the presence of hydrogen peroxide using an innovative microwave photochemical reactor. *Journal of Hazardous Materials Journal of Hazardous Materials* 2011; 186: 1808–1815.
3. Chen C, Yang S, Guo Y, *et al.* Photolytic destruction of endocrine disruptor atrazine in aqueous solution under UV irradiation: Products and pathways. *Journal of Hazardous Materials Journal of Hazardous Materials* 2009; 172: 675–684.
4. Kaur S, Kumar V, Chawla M, *et al.* Pesticides curbing soil fertility: Effect of complexation of free metal ions. *Frontiers in Chemistry* 2017; 5: 1–9.
5. Singh S, Kumar V, Chauhan A, *et al.* Toxicity, degradation and analysis of the herbicide atrazine. *Environmental Chemistry Letters* 2017; 16: 1–27.
6. Chen IM, Wanitchapichat W, Jirakittayakorn T, *et al.* Hexachlorobenzene dechlorination by indigenous sediment microorganisms. *Journal of Hazardous Materials Journal of Hazardous Materials* 2010; 177: 244–250.
7. Chandra R, Bharagava RN, Yadav S, *et al.* Accumulation and distribution of toxic metals in wheat (*Triticum aestivum* L.) and Indian mustard (*Brassica campestris* L.) irrigated with distillery and tannery effluents. *Journal of Hazardous Materials Journal of Hazardous Materials* 2009; 162: 1514–1521.
8. Singh S, Singh N, Kumar V, *et al.* Toxicity, monitoring and biodegradation of the fungicide carbendazim. *Environmental Chemistry Letters* 2016; 14: 317–329.
9. Du Y, Zhao L, Chang Y, *et al.* Tantalum (oxy) nitrides nanotube arrays for the degradation of atrazine in vis-Fenton-like process. *Journal of Hazardous Materials* 2012; 226: 21–27.
10. Environmental Protection Agency (EPA). Interim reregistration eligibility decision for atrazine, pp 2005 (EPA-HQ-OPP-2003-0072-0002), U.S. Environmental Protection Agency, Washington, DC, 2003.
11. Kumar V, Kaur S, Singh S, *et al.* Unexpected formation of N-phenyl-thiophosphorohydrazidic acid O,S-dimethyl ester from acephate: Chemical, biotechnical and computational study. *3Biotech*. 2016; 6(1): 1–11.
12. Dombek T, Dolan E, Schultz J, *et al.* Rapid reductive dechlorination of atrazine by zero-valent iron under acidic conditions. *Environmental Pollution*, 2001; 111: 21–27.
13. Gillham RW, O'Hannesin SF. Enhanced degradation of halogenated aliphatics by zero-valent iron. *Ground Water* 1994; 32(6): 958–967.

14. Herwig U, Klumpp E, Narres HD, *et al.* Physicochemical interactions between atrazine and clay minerals. *Applied Clay Science* 2001; 18: 211–222.
15. Kumar V, Upadhyay N, Manhas A. Designing, syntheses, characterization, computational study and biological activities of silver-phenothiazine metal complex. *Journal of Molecular Structure* 2015; 1099: 135–140.
16. Johnson TL, Scherer MM, Tratnyek PG. Kinetics of halogenated organic compound degradation by iron metal. *Environmental Science and Technology* 1996; 30: 634–2640.
17. Kim G, Woohyeok JW, Choe S. Dechlorination of atrazine using zero-valent iron (Fe^0) under neutral pH conditions. *Journal of Hazardous Materials* 2008; 155: 502–506.
18. Kumar V, Upadhyay N, Kumar V, *et al.* A review on sample preparation and chromatographic determination of acephate and methamidophos in different samples. *Arabian Journal of Chemistry* 2015; 08: 624–631.
19. Kumar V, Upadhyay N, Kumar V, *et al.* Interactions of atrazine with transition metal ions in aqueous media: Experimental and computational approach. *3 Biotech* 2015; 5: 791–798
20. Kumar V, Upadhyay N, Wasit AB, *et al.* Spectroscopic methods for the detection of organophosphate pesticides—A preview. *Current World Environment* 2013; 8(2): 313–318.
21. Kumar V, Upadhyay N, Singh S, *et al.* Thin-layer chromatography: comparative estimation of soil's atrazine. *Current World Environment* 2013; 8: 469–473.
22. Martin M, Hagege AA, Brunette JP, *et al.* Use of synergistic extraction for the study of atrazine/metal interactions. *Analytica Chimica Acta* 1998; 373: 161–165.
23. Kumar V, Singh S, Singh R, *et al.* Spectral, structural and energetic study of acephate, glyphosate, monocrotophos and phorate: An experimental and computational approach. *Journal of Taibah University for Science* 2018; 12 (1): 69–78.
24. Matheson LJ, Tratnyek PG. Reductive dehalogenation of chlorinated methanes by iron metal. *Environmental Science and Technology* 1994; 28 (12): 2045–2053.
25. Nelkenbaum E, Dror I, Berkowitz B. Reductive dechlorination of atrazine catalyzed by metalloporphyrins. *Chemosphere* 2009; 75: 48–55.
26. Palma LD, Ferrantelli P, Petrucci E. Experimental study of the remediation of atrazine contaminated soils through soil extraction and subsequent peroxidation. *Journal of Hazardous Materials* 2003; 99: 265–276.
27. Kumar V, Singh S, Singh R, *et al.* Design, synthesis, and characterization of 2,2-bis(2,4-dinitrophenyl)-2-(phosphonomethylamino)acetate as a herbicidal and biological active agent. *Journal of Chemical Biology* 2017; 10(4): 179–190.
28. Kumar V, Chawla M, Cavallo L, *et al.* Complexation of trichlorosalicylic acid with alkaline and first row transition metals as a switch for their antibacterial activity. *Inorganica Chimica Acta* 2018; 469: 379–386.
29. Patel UD, Suresh S. Effects of solvent, pH, salts and resin fatty acids on the dechlorination of pentachlorophenol using magnesium–silver and magnesium–palladium bimetallic systems. *Journal of Hazardous Materials* 2008; 156: 308–316.
30. Poonam, Kumari P, Ahmad S, *et al.* Reductive dechlorination of atrazine using sodium-borohydride catalysed by cobalt(II) phthalocyanines. *Tetrahedron Letters* 2011; 52: 7083–7086.
31. Prasad R, Upadhyay N, Kumar V. Simultaneous determination of seven carbamate pesticide residues in gram, wheat, lentil, soybean, fenugreek leaves and apple matrices. *Microchemical Journal* 2013; 111: 91–97.
32. Singh KP, Malik A, Mohan D, *et al.* Distribution of persistent organochlorine pesticide residues in Gomti River, India. *Bulletin of Environmental Contamination and Toxicology* 2005; 74(1): 146–154.
33. Singh KP, Mohan D, Sinha S, *et al.* Impact assessment of treated/untreated wastewater toxicants discharged by sewage treatment plants on health, agricultural, and environmental quality in the wastewater disposal area. *Chemosphere* 2004; 55: 227–255.
34. Ta N, Hong J, Liu T, *et al.* Degradation of atrazine by microwave-assisted electrodeless discharge mercury lamp in aqueous solution.

- Journal of Hazardous Materials 2006; 138: 187–197.
35. Tewari BB, Mohan D. Interaction of 2, 4-dinitrophenol and 2, 4, 6-trinitrophenol with copper, zinc, molybdenum and chromium ferrocyanides. *Colloids and Surfaces A* 1998; 131: 89–93.
 36. Wang X, Chen C, Chang Y, *et al.* Dechlorination of chlorinated methanes by Pd/Fe bimetallic nanoparticles. *Journal of Hazardous Materials* 2009; 161: 815–823.
 37. Xu J, Lv X, Li J, *et al.* Simultaneous adsorption and dechlorination of 2,4-dichlorophenol by Pd/Fe nanoparticles with multi-walled carbon nanotube support. *Journal of Hazardous Materials* 2012; 226: 36–45.
 38. Kumar V, Singh S, Singh A, *et al.* Phytochemical analysis and comprehensive evaluation of antimicrobial, protein binding and antioxidant properties of *Tinospora cordifolia*. *Journal of Biologically Active Products from Nature* 2018; 8(3): 192–200.
 39. Xu LJ, Chu W, Graham N. Atrazine degradation using chemical-free process of USUV: Analysis of the micro-heterogeneous environments and the degradation mechanisms. *Journal of Hazardous Materials*; 2014; 275: 166–174.
 40. Kumar V, Singh S, Singh J, *et al.* Potential of plant growth promoting traits by bacteria isolated from heavy metal contaminated soils. *Bulletin of Environmental Contamination and Toxicology* 2015; 94: 807–814.
 41. Zhang Y, Meng D, Wang Z, *et al.* Oxidative stress response in atrazine-degrading bacteria exposed to atrazine. *Journal of Hazardous Materials* 2012; 238: 44–438.
 42. Zhou H, Han J, Baig SA, *et al.* Dechlorination of 2,4-dichlorophenoxyacetic acid by sodium carboxymethyl cellulose-stabilized Pd/Fe nanoparticles. *Journal of Hazardous Materials* 2011; 198: 7–12.

REVIEW ARTICLE

Carbon nanomaterials for metal-free electrocatalysis

Ana M.B. Honorato^{1*}, Mohd. Khalid²

¹ Center of Advanced Science and Engineering for Carbon (Case4carbon), Department of Macromolecular Science and Engineering, Case Western Reserve University, 10900 Euclid Avenue, Cleveland, OH 44106, USA. E-mail: abh70@case.edu

² Institute of Chemistry of São Carlos, University of São Paulo, POBox 780, 13560-970, São Carlos, SP, Brazil. E-mail: mkansarister@gmail.com

ABSTRACT

Carbon materials are continuing in progress to accomplish the requirements of energy conversion and energy storage technologies because of their plenty in nature, high surface area, outstanding electrical properties, and readily obtained from varieties of chemical and natural sources. Recently, carbon-based electrocatalysts have been developed in the quest to replacement of noble metal based catalysts for low cost energy conversion technologies, such as fuel cell, water splitting, and metal-air batteries. Herein, we will present our short overview on recently developed carbon-based electrocatalysts for energy conversion reactions such as oxygen reduction, oxygen evolution, and hydrogen evolution reactions, along with challenges and perspectives in the emerging field of metal-free electrocatalysts.

Keywords: Carbon Nanomaterials; Graphene; Metal-Free Electrocatalyst; Hydrogen Evolution Reaction

ARTICLE INFO

Received 12 April 2020
Accepted 20 May 2020
Available online 25 May 2020

COPYRIGHT

Copyright © 2020 Ana M.B. Honorato, et al.
EnPress Publisher LLC. This work is licensed under the Creative Commons Attribution-NonCommercial 4.0 International License (CC BY-NC 4.0).
<https://creativecommons.org/licenses/by-nc/4.0/>

1. Background

Energy requirement is one of the most important issues of our time, because of the continue depletion of fossil fuels and associated increasing air pollution. Hydrogen is considered totally non-polluting fuel but unlike fossil fuels it does not typically occurs by itself in nature, despite being a most abundant element on the earth, therefore, it must be generated from chemical source, that contain hydrogen molecules. It is observed that the world produces more than 50 billion kilograms of hydrogen each year and more than 95 percent generated from fossil fuels through steam reformation of natural gas. This process inherent additional costs to manufacturers, consumers, and it is environmentally unsafe. To avoid future devastation caused by energy collapse, the need for renewable energy has engrossed tremendously. In order to make effective use of renewable energy, it is imperative to develop high-performance, low-cost, and environmentally friendly energy conversion systems. In this regard, water is an ultimate option because it is sustainable and readily available. Catalytic water splitting to produce hydrogen is an advanced electrochemical technique but water splitting needs expensive novel metal based catalysts (e.g., Pt) to accelerate the rate of hydrogen production and to lower the energy loss in the process.

Electrocatalysis is the heart of the electrochemical energy conversion. Renewable energy technologies, such as fuel cells, water splitting,

and metal-air batteries, are the promising means of the increasing global need of energy, offering clean and sustainable energy resources. But the key to success is the development of non-noble metal, robust, cost effective, and earth-abundant material based electrocatalysts that catalyze the reactions which take place in renewable energy systems such as oxygen reduction reaction (ORR), oxygen evolution reaction (OER), and hydrogen evolution reaction (HER) with high efficiency and stability. Benchmark Pt, Ir, Pd-based and RuO₂-based catalysts are generally needed to promote the HER for the generation hydrogen fuel from the electrochemical water splitting, the ORR in fuel cells for energy conversion and the OER in metal-air batteries for energy storage^[1]. Nevertheless, their widespread adoption is constricted due to the high cost, low stability, scarcity, and environmental unfriendly nature. In the search of earth abundant and benign catalysts materials, impressive advances have been made towards the development of nonprecious metal based electrocatalysts and their recent results prospect the increase of the performance by taking advantage of the synergy of carbon nanomaterials and non-precious metals with the aim of completely or partially replacing the precious metal based catalysts (Pt-based). Basically, the performance of electrocatalyst directly depends to the materials properties. Therefore, materials technologies play a vital role in the development of electrochemical energy conversion and energy storage systems.

2. The recent development of nonprecious metal-based electrocatalysts

The various transition metals, in particular Fe, Co, and Ni, and their compounds such as transition-metal sulfides, selenides, nitrides, carbides, phosphides, and borides as well as their alloys have been shown to be promising catalysts for the hydrogen evolution reaction^[2]. Recently, some coordination compounds, such as a Ni bisdiphosphine based mimic of hydrogenase enzymes^[3], Cu^{II} ethylenediamine (Cu-EA), polyoxometalate (POM) based metal-organic frameworks^[4], have also been developed as potential for hydrogen evolution. Substantial research effort has been devoted to the

development of OER catalysts based on relatively inexpensive transition metals and their compounds, including transition-metal oxides, multimetal oxides, metal oxide based hybrids, substituted cobaltites (M_xCo_{3-x}O₄), hydro(oxy)oxides, phosphates, diselenide, metal oxide/diselenide hybrids, and chalcogenides^[5-33], because OER is the half (2H₂O → O₂ + 4H⁺ + 4e⁻) conjunction reaction of HER (2H⁺ + 2e⁻ → H₂). In general, the overall water splitting process can be represented as follows, with molecular hydrogen and oxygen generated individually at the cathode and anode, respectively.

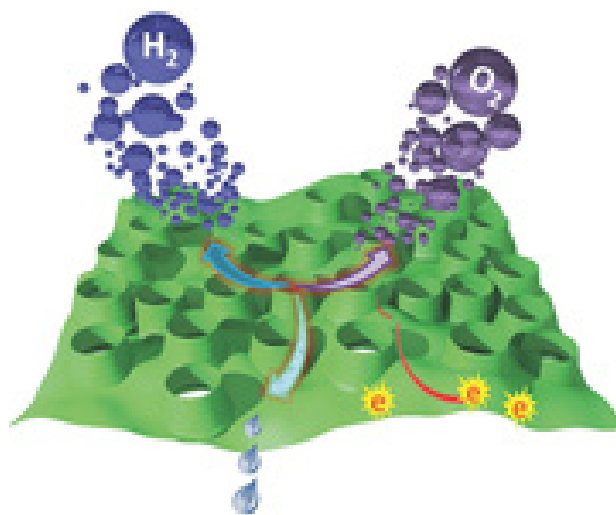


In addition, ordered Ni₃P₄ nanoarchitectures with a “sheetlike” morphology on a Ni foil were synthesized and found to be bifunctional catalysts for both the HER and the OER^[34]. However, the transition-metal-based catalysts are prone to gradual oxidation, undesirable changes in the morphology/crystalline structure, and uncontrolled agglomeration/dissolution when exposed to air or aerated electrolytes^[35]. For example, the HER activity of MoS₂ in alkaline electrolytes often deteriorates in just a few cycles^[36]. Most of the nonprecious-metal catalysts have a poor electronic conductivity, and hence a limited electrocatalysis performance. To overcome this limitation, conductive support of carbon nanomaterials such as graphene and carbon nanotubes have been used to improve the activities of these catalysts^[37-39]. Examples include Ni/rGO, Ni/Fe hydroxide nanoplates on CNTs, FeNi hydroxide/rGO, NiO/rGO, Co₃O₄/rGO, Co-CoO/N-rGO and Ni-NiO/N-rGO composites, metal carbides M₃C/graphene nanoribbons (M: Fe, Co, Ni), Fe@C, MoS₂-graphene/carbon nanofiber, MoS₂/N doped graphene, WS₂/CNTs, and Co@N-doped carbon catalysts^[40-46]. Accordingly, a wide range of oxide based catalysts have emerged as the materials of choice for catalyzing energy conversion reactions ORR, OER, and HER, since, their low stability and complex preparation process renders widespread adoption.

3. The recent development of carbon-based metal-free electrocatalysts

Among the various non-precious metal-based

electrocatalysts have been investigated, carbon materials are of great interest owing to their abundance, stability even in harsh acidic and basic medium, and relative environmental-friendliness. However, carbon nanomaterials are also not free from disadvantages, for example carbon nanomaterials itself do not show catalytic activities unless they are incorporated with guest noble or transition metals as above has been discussed. In the pioneer work of Dai and co-worker discovered that vertically-aligned nitrogendoped carbon nanotube arrays can act as a catalyst for ORR without using metals, and this metal-free catalyst shows almost three-times higher electrocatalytic activity, much smaller crossover effect, and better long-term operational stability than those of commercially available platinum/C electrodes^[47]. Since, the discovery of graphene by Novoselov and Geim in 2004, the research on this flattish material has received enormous attention. This flat sheet is a one-tom-thick layer of sp^2 -bonded, 2D honeycomb lattice of carbon with a fully conjugated structure of alternating C-C and C=C bonds. Its unique physicochemical properties make this material a promising candidate for a large variety of applications. However, the use of graphene for most of the electronic applications often requires the precise functionalization of individual graphene sheets into various device elements at the molecular level. Therefore, surface functionalization of graphene sheets is essential, and researchers have devised various covalent and noncovalent chemistries for making graphene materials with the bulk and surface properties needed for many potential applications including energy conversion and storage. Thus, graphene-based catalysts can hold great promise to replace precious-metal catalysts for clean energy technologies. However, graphene also like other carbon nanomaterials does not show catalytic activities, doped graphene with heteroatoms play a crucial role to tune their electronic structure and chemical properties which develop the catalytic active sites in graphene network, hence, demonstrate catalytic performance. Doping of graphene nanomaterials with heteroatoms, such as N, B, O, P, S, Cl, I, Se, and Br, has been performed to be a feasible way to tune their electronic structures and chemical and electrochemical properties^[48–53]. As



Graph shows the trifunctional activities (ORR, OER, and HER) of the porous carbon, adopted from Ref^[36].

the size and electronegativity of the heteroatoms are different from the carbon atoms, the introduction of heteroatoms could cause electronic modulation to change the charge distribution and electronic properties of carbon skeletons, which in turn affects their interaction with hydrogen or oxygen intermediates and ultimately their electrocatalytic activities for the OER, HER and ORR^[54–56].

It is also recently, verified that the carbon nanostructure (3D) with tunable defects and porous structure like micro, meso, and macro possess extraordinary mass transport capability to facilitate metal-free electrocatalysis in energy conversion and energy storage applications^[57–59]. Metal-free, nitrogen and phosphorus co-doped 3D graphitic carbon networks have recently been developed by using a scalable, one-step process involving the pyrolysis of a polyaniline aerogel synthesized in the presence of phytic acid, which were demonstrated to show remarkably high bifunctional electrocatalytic activities for ORR and OER simultaneously, and in primary and rechargeable Zn-air batteries as an air cathode as depicted in **Figure 1**^[60]. Further, the same group generate tri-doped graphene materials with nitrogen, phosphorus, and fluorine doping agents, followed by the thermal pyrolysis of polyaniline pre-coated graphene oxide in presence of ammonium hexafluorophosphate, and used as an efficient tri-functional electrocatalyst for OER and HER for electrochemical water splitting, powered by a Zn-air battery based on an air electrode with

the same electrocatalyst for ORR, to generate oxygen and hydrogen gases^[61].

On the other hand, the construction of an ideal electrocatalyst which works for ORR, OER, and HER simultaneously is also a crucial. Usually, the activities of catalysts vary with pH values^[62]. This makes the development of integrated energy system difficult. A rationally-designed N, S co-doped graphitic sheets with stereoscopic holes, trifunctional metal-free electrocatalysts was developed for overall water-splitting. In this case, the multifunctional electrocatalytic activities for simultaneous ORR, OER and HER were ascribed to a synergistic effect of the N, S heteroatom co-doping and its unique

stereoscopic holes structure, which provided a large surface area and efficient pathways for electron and electrolyte transports^[63]. Therefore, these low-cost, metal-free, tri-functional electrocatalysts based on either tri-doped or co-doped carbon electrocatalysts hold great promise for a wide range of applications, particularly in integrated energy systems. Despite the progress that has been made in carbon based electrocatalysts in water splitting technologies in recent years, however, these techniques are still in nascent stage and facing several challenges to commercial utilization, including high capital costs related to expensive preparation process of materials and a high material consumption insufficient endur-

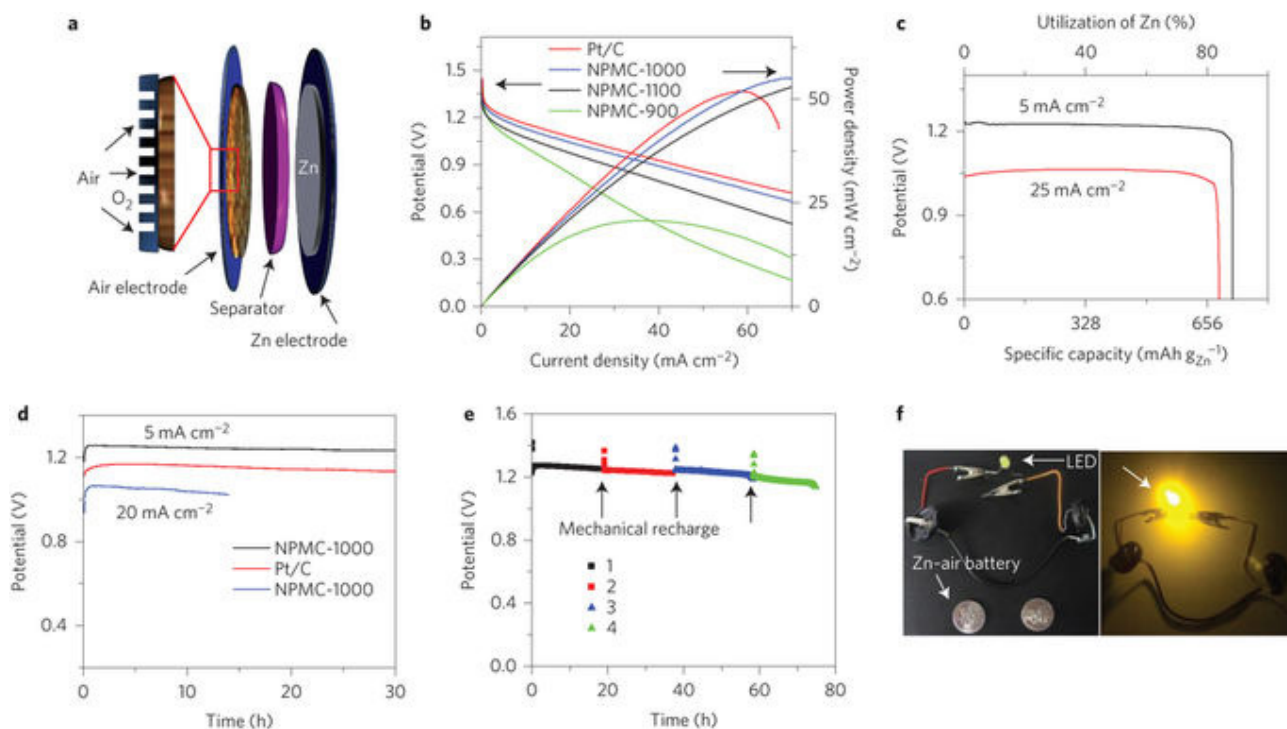


Figure 1. **a)** Schematic illustration for the basic configuration of a primary Zn-air battery, in which a carbon paper pre-coated with NPMC is used as an air cathode and is coupled with a Zn anode, and a glassy fiber membrane soaked with aqueous KOH electrolyte as separator. The enlarged part illustrates the porous air electrode loaded with electrocatalyst, which is permeable to air and oxygen; **b)** Polarization and power density curves of primary Zn-air batteries using Pt/C, NPMC-900, NPMC-1000, NPMC-1100 as ORR catalyst (mass loading of $0.5 \text{ mg} \cdot \text{cm}^{-2}$) and 6 M KOH electrolyte (scan rate, $5 \text{ mV} \cdot \text{s}^{-1}$); **c)** Specific capacities of the Zn-air batteries using NPMC-1000 as ORR catalyst are normalized to the mass of the consumed Zn; **d)** Discharge curves of the primary Zn-air batteries using Pt/C and NPMC-1000 as ORR catalyst and KOH electrolyte at various current densities (5 and $20 \text{ mA} \cdot \text{cm}^{-2}$). The observed sudden drop in voltage at 0 h was caused by a sudden increase in current density after resting the battery at the open-circuit potential without current loading for the testing; **e)** Long-time durability of the primary Zn-air battery using NPMC-1000 catalyst at a current density of $2 \text{ mA} \cdot \text{cm}^{-2}$. The battery is mechanically rechargeable. The Zn and electrolyte were mechanically replaced at the point where the color of the curve changes (the numbers represent the first, second, third and fourth charge cycles). Colored symbols above the curve are taken from the open-circuit potential by opening the battery for each mechanical recharge; **f)** Optical images of an LED (2.2 V) before and after being driven by two Zn-air batteries in series. Reproduced with permission from Ref^[60]. Copyright (2015) by Nature Publishing Group.

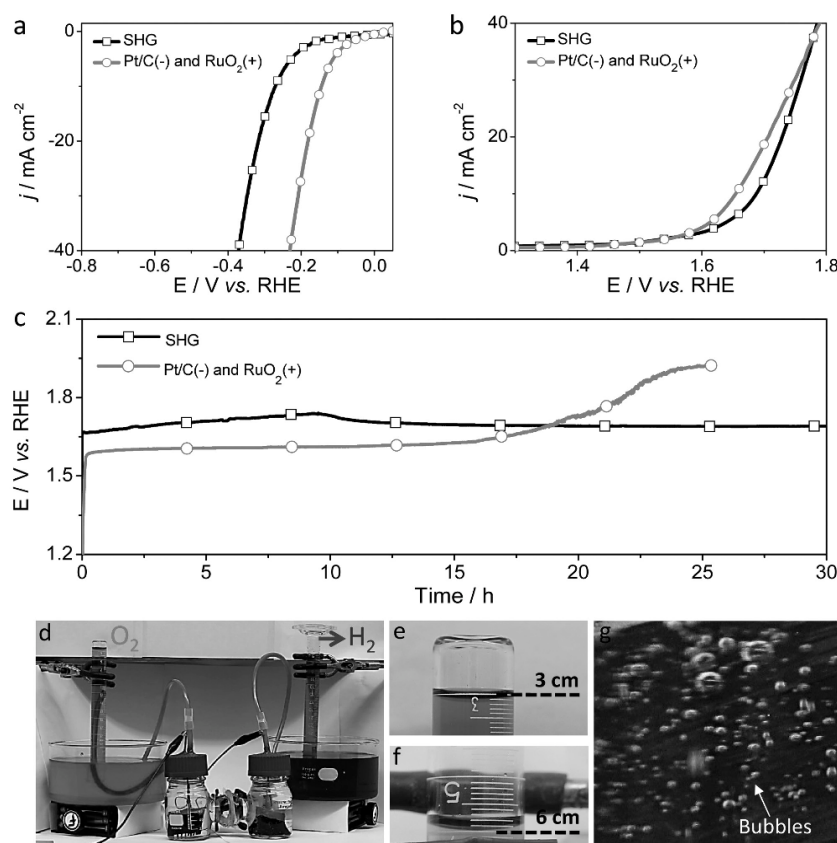


Figure 2. **a)** HER and **b)** OER activities of SHG(-)/SHG(+) and Pt/C(-)/RuO₂(+) two-electrode setup with the scan rate of 10 mV·s⁻¹; the electrolyte: 1.0 m KOH; **c)** Chronopotentiometric curve of water electrolysis for SHG(-)/SHG(+) and Pt/C(-)/RuO₂(+) with constant current density of 10 mA·cm⁻² in 1.0 m KOH; **d)** The demonstration of SHG in a homemade two-electrode water splitting device by chronopotentiometry at a given potential of 2 V. The carbon fiber woven mesh (3 × 2 cm) was used as an all-carbon electrode for deposition the SHG catalyst; **e)** Oxygen and **f)** hydrogen collection process with displacement of water; **g)** Bubbles generated from the electrode (e.g., H₂ electrode) during the water splitting process. Reproduced with permission from Ref^[36]. Copyright (2017) by John Wiley and Sons.

ance of its main components, complex system design and time-consuming production technologies. However, there are still big rooms in metal-free electrocatalysts for further improvement in terms of combined experimental and theoretical approaches to understand the location and structure of active sites and their work functions. We hope this mini review will offer valuable insight to gain further knowledge in this area.

Conflict of interest

The authors declare that they have no conflict of interest.

References

1. Caban-Acevedo M, Stone ML, Schmidt JR, *et al.* Efficient hydrogen evolution catalysis using ternary pyrite-type cobalt phosphosulphide. *Nature Materials* 2015; 14: 1245–1251.
2. Bates MK, Jia QY, Ramaswamy N, *et al.* Composite Ni/NiO-Cr₂O₃ catalyst for alkaline hydrogen evolution reaction. *The Journal of Physical Chemistry C* 2015; 119: 5467–5477.
3. Goff AL, Artero V, Josselme B, *et al.* From hydrogenases to noble metal-free catalytic nanomaterials for H₂ production and uptake. *Science* 2009; 326: 1384–1387.
4. Liu X, Cui S, Sun Z, *et al.* Robust and highly active copper-based electrocatalyst for hydrogen production at low overpotential in neutral water. *Chemical Communication* 2015; 51: 12954–12957.
5. Liang Y, Li Y, Wang H, *et al.* Co₃O₄ nanocrystals on graphene as a synergistic catalyst for oxygen reduction reaction. *Nature Materials*

- 2011; 10: 780–786.
6. Sun Y, Gao S, Lei F, *et al.* Atomically-thin non-layered cobalt oxide porous sheets for highly efficient oxygen-evolving electrocatalysts. *Chemical Science* 2014; 5: 3976–3982.
 7. Smith RD, Prvot MS, Fagan RD, *et al.* Photochemical route for accessing amorphous metal oxide materials for water oxidation catalysis. *Science* 2013; 340: 60–63.
 8. Grimaud A, May KJ, Carlton CE, *et al.* Double perovskites as a family of highly active catalysts for oxygen evolution in alkaline solution. *Nature Communication* 2013; 4: 2439.
 9. Peng Z, Jia D, Al-Enizi A, *et al.* Electrocatalysts: From water oxidation to reduction: homologous ni-co based nanowires as complementary water splitting electrocatalysts. *Advanced Energy Materials* 2015; 5: 1402031.
 10. Subbaraman R, Tripkovic D, Chang KC, *et al.* Trends in activity for the water electrolyser reactions on 3d M(Ni,Co,Fe,Mn) hydr(oxy)oxide catalysts. *Nature Materials* 2012; 11: 550–557.
 11. Wee TL, Sherman BD, Gust D, *et al.* Photochemical synthesis of a water oxidation catalyst based on cobalt nanostructures. *Journal of the American Chemical Society* 2011; 133: 16742–16745.
 12. Rosen J, Hutchings GS, Jiao F. Ordered mesoporous cobalt oxide as highly efficient oxygen evolution catalyst. *Journal of the American Chemical Society* 2013; 135: 4516–4521.
 13. Ryu J, Jung N, Jang JH, *et al.* In situ transformation of hydrogen-evolving cop nanoparticles: toward efficient oxygen evolution catalysts bearing dispersed morphologies with co-oxo/hydroxo molecular units. *ACS Catalysis* 2015; 5: 4066–4074.
 14. Zheng YR, Gao MR, Gao Q, *et al.* An efficient CeO₂/CoSe₂ nanobelt composite for electrochemical water oxidation. *Small* 2015; 11: 182–188.
 15. Wu L, Li Q, Wu C, *et al.* Stable cobalt nanoparticles and their monolayer array as an efficient electrocatalyst for oxygen evolution reaction. *Journal of the American Chemical Society* 2015; 137: 7071–7074.
 16. Koza JA, He Z, Miller A, *et al.* Electrodeposition of crystalline Co₃O₄—A catalyst for the oxygen evolution reaction. *Chem. Mater.* 2012; 24: 3567–3573.
 17. Hutchings GS, Zhang Y, Li J, *et al.* In situ formation of cobalt oxide nanocubanes as efficient oxygen evolution catalysts. *Journal of the American Chemical Society* 2015; 137: 4223–4229.
 18. Hamdani M, Singh R, Chartier P. Co₃O₄ and Co-based spinel oxides bifunctional oxygen electrodes. *International Journal of Electrochemical Science* 2010; 5: 556–577.
 19. Lu X, Zhao C. Highly efficient and robust oxygen evolution catalysts achieved by anchoring nanocrystalline cobalt oxides onto mildly oxidized multiwalled carbon nanotubes. *Journal of Materials Chemistry A* 2013; 1: 12053–12059.
 20. Zhu C, Wen D, Leubner S, *et al.* Nickel cobalt oxide hollow nanosponges as advanced electrocatalysts for the oxygen evolution reaction. *Chemical Communication* 2015; 51: 851–7854.
 21. Li Y, Hasin P, Wu Y. Ni_xCo_{3-x}O₄ nanowire arrays for electrocatalytic oxygen evolution. *Advanced Materials* 2010; 22: 1926–1929.
 22. Chen S, Duan JJ, Jaroniec M, *et al.* Three-dimensional N-doped graphene hydrogel/NiCo double hydroxide electrocatalysts for highly efficient oxygen evolution. *Angewandte Chemie International Edition* 2013; 52: 13567–13570.
 23. Wang J, Qiu T, Chen X, *et al.* Hierarchical hollow urchin-like NiCo₂O₄ nanomaterial as electrocatalyst for oxygen evolution reaction in alkaline medium. *Journal of Power Sources* 2014; 268: 341–348.
 24. Trotochaud L, Ranney JK, Williams KN, *et al.* Solution-cast metal oxide thin film electrocatalysts for oxygen evolution. *Journal of the American Chemical Society* 2012; 134: 17253–17261.
 25. McCrory CCL, Jung SH, Peters JC, *et al.* Benchmarking heterogeneous electrocatalysts for the oxygen evolution reaction. *Journal of the American Chemical Society* 2013; 135: 16977–16987.
 26. Kanan MW, Nocera DG. In situ formation of an oxygen-evolving catalyst in neutral water containing phosphate and Co₂⁺. *Science* 2008; 321:

- 1072–1075.
27. Wang YC, Jiang K, Zhang H, *et al.* Bio-inspired leaf-mimicking nanosheet/nanotube heterostructure as a highly efficient oxygen evolution catalyst. *Advanced Science* 2015; 2: 1500003.
 28. Nikolov I, Darkaoui R, Zhecheva E, *et al.* Electrocatalytic activity of spinel related cobalties $MxCo_{3-x}O_4$ ($M = Li, Ni, Cu$) in the oxygen evolution reaction. *Journal of Electroanalytical Chemistry* 1997; 429: 157–168.
 29. Zhuang Z, Sheng W, Yan Y. Synthesis of monodisperse $Au@Co_3O_4$ core-shell nanocrystals and their enhanced catalytic activity for oxygen evolution reaction. *Advanced Materials* 2014; 26: 3950–3955.
 30. Gong M, Zhou W, Tsai MC, *et al.* Nanoscale nickel oxide/nickel heterostructures for active hydrogen evolution electrocatalysis. *Nature Communication*. 2014; 5: 4695.
 31. Suntivich J, May KJ, GasteigerHA, *et al.* A perovskite oxide optimized for oxygen evolution catalysis from molecular orbital principles. *Science* 2011; 334: 1383–1385.
 32. Smith RDL, Prevot MS, Fagan RD, *et al.* Water oxidation catalysis: electrocatalytic response to metal stoichiometry in amorphous metal oxide films containing iron, cobalt, and nickel. *Journal of the American Chemical Society* 2013; 135: 11580–11586.
 33. Zhou W, Wu X, Cao X, *et al.* Ni_3S_2 nanorods/ Ni foam composite electrode with low overpotential for electrocatalytic oxygen evolution. *Energy & Environmental Science* 2013; 6: 2921–2924.
 34. Ledendecker M, Krick Calder S, Papp C, *et al.* The synthesis of nanostructured Ni_5P_4 films and their use as a non-noble bifunctional electrocatalyst for full water splitting. *Angewandte Chemie International Edition* 2015; 54: 12361–12365.
 35. Gao MR, Cao X, Gao Q, *et al.* Nitrogen-doped graphene supported $CoSe_2$ nanobelt composite catalyst for efficient water oxidation. *ACS Nano* 2014; 8: 3970–3978.
 36. Merki D, Fierro S, Vrabel H, *et al.* Amorphous molybdenum sulfide films as catalysts for electrochemical hydrogen production in water. *Chemical Science* 2011; 2: 1262–1267.
 37. Li Q, Xu P, Zhang B, *et al.* One-step synthesis of Mn_3O_4 /reduced graphene oxide nanocomposites for oxygen reduction in nonaqueous $Li-O_2$ batteries. *Chemical Communication* 2013; 49: 10838–10840.
 38. He QG., Li Q, Khene S, *et al.* High-loading cobalt oxide coupled with nitrogen-doped graphene for oxygen reduction in anion-exchange-membrane alkaline fuel cells. *The Journal of Physical Chemistry C* 2013; 117: 8697–8707.
 39. Li Q, Xu P, Gao W, *et al.* One-step synthesis of Mn_3O_4 /reduced graphene oxide nanocomposites for oxygen reduction in nonaqueous $Li-O_2$ batteries. *Advanced Materials* 2014; 26: 1378–386.
 40. Chen S, Duan J, Ran J, *et al.* N-doped graphene film-confined nickel nanoparticles as a highly efficient three-dimensional oxygen evolution electrocatalyst. *Energy & Environmental Science* 2013; 6: 3693–3699.
 41. Gong M, Li YG, Wang H, *et al.* An advanced Ni-Fe layered double hydroxide electrocatalyst for water oxidation. *Journal of the American Chemical Society* 2013; 135: 8452–8455.
 42. Long X, Li J, Xiao S, *et al.* A strongly coupled graphene and FeNi double hydroxide hybrid as an excellent electrocatalyst for the oxygen evolution reaction. *Angewandte Chemie International Edition* 2014; 53: 7584–7588.
 43. Liu X, Liu W, Ko M, *et al.* Metal (Ni, Co)-metal oxides/graphene nanocomposites as multifunctional electrocatalysts. *Advanced Functional Materials* 2015; 25: 5799–5808.
 44. Fan X, Peng Z, Ye R, *et al.* M_3C ($M: Fe, Co, Ni$) nanocrystals encased in graphene nanoribbons: An active and stable bifunctional electrocatalyst for oxygen reduction and hydrogen evolution reactions. *ACS Nano* 2015; 9: 7407–7418.
 45. Tavakkoli M, Kallio T, Reynaud O, *et al.* Single-shell carbon-encapsulated iron nanoparticles: synthesis and high electrocatalytic activity for hydrogen evolution reaction. *Angewandte Chemie International Edition* 2015; 54: 4535–4538.
 46. Ye TN, Lv LB, Xu M, *et al.* Hierarchical car-

- bon nanopapers coupled with ultrathin MoS₂ nanosheets: Highly efficient large-area electrodes for hydrogen evolution. *Nano Energy* 2015; 15: 335–342.
47. Gong K, Du F, Xia Z, *et al.* Nitrogen-doped carbon nanotube arrays with high electrocatalytic activity for oxygen reduction. *Science* 2009; 323: 760–764.
 48. Yang HB., Miao J, Hung SF, *et al.* Identification of catalytic sites for oxygen reduction and oxygen evolution in N-doped graphene materials: Development of highly efficient metal-free bifunctional electrocatalyst. *Science Advances* 2016; 22: e1501122.
 49. Dai L. Functionalization of graphene for efficient energy conversion and storage. *Accounts of Chemical Research* 2013; 46: 31–42.
 50. Zhang J, Dai L. Heteroatom-doped graphitic carbon catalysts for efficient electrocatalysis of oxygen reduction reaction. *ACS Catalysis* 2015; 5: 7244–7253.
 51. Sun X, Song P, Zhang Y, *et al.* A class of high performance metal-free oxygen reduction electrocatalysts based on cheap carbon blacks. *Scientific Reports* 2013; 3: 2505.
 52. Liu Z, Peng F, Wang H, *et al.* Novel phosphorus-doped multiwalled nanotubes with high electrocatalytic activity for O₂ reduction in alkaline medium. *Catalysis Communications* 2011; 1: 35–38.
 53. Geng D, Chen Y, Li Y, *et al.* High oxygen-reduction activity and durability of nitrogen-doped graphene. *Energy & Environment Science* 2011; 4: 760–764.
 54. Lee RS, Kim HJ, Fischer JE, *et al.* Conductivity enhancement in single-walled carbon nanotube bundles doped with K and Br. *Nature* 1997; 388: 255–257.
 55. Avouris P, Chen Z, Perebeinos V. Carbon-based electronics. *Nature Nanotechnology* 2007; 2: 605–615.
 56. Duan JJ, Chen S, Jaroniec M, *et al.* Heteroatom-doped graphene-based materials for energy-relevant electrocatalytic processes. *ACS Catalysis* 2015; 5: 5207–5234.
 57. Xue Y, Yu D, Dai L, *et al.* Three-dimensional B, N-doped graphene foam as a metal-free catalyst for oxygen reduction reaction. *Physical Chemistry Chemical Physics* 2013; 15: 12220–12226.
 58. Yu DS, Goh K, Wang H, *et al.* Scalable synthesis of hierarchically structured carbon nanotube-graphene fibres for capacitive energy storage. *Nature Nanotechnology* 2014; 9: 555–562.
 59. Xue Y, Ding Y, Niu J, *et al.* Rationally designed graphene-nanotube 3D architectures with a seamless nodal junction for efficient energy conversion and storage. *Science Advances* 2015; e1400198.
 60. Zhang J, Zhao Z, Xia Z, *et al.* A metal-free bifunctional electrocatalyst for oxygen reduction and oxygen evolution reactions. *Nature Nanotechnology* 2015; 10: 444–452.
 61. Zhang J, Dai L. N,P-codoped carbon networks as efficient metal-free bifunctional catalysts for oxygen reduction and hydrogen evolution reactions. *Angewandte Chemie International Edition* 2016; 55: 2230–2234.
 62. Dai L, Xue Y, Qu L, *et al.* Metal-free catalysts for oxygen reduction reaction. *Chemical Reviews* 2015; 115: 4823.
 63. Hu C, Dai L. Multifunctional carbon-based metal-free electrocatalysts for simultaneous oxygen reduction, oxygen evolution, and hydrogen evolution. *Advanced Materials* 2017; 29: 1604942.



Applied Chemical Engineering

Focus and Scope

Applied Chemical Engineering (ACE) is an international open-access academic journal dedicated to publishing highly professional research in all fields related to chemical engineering. All manuscripts are subjected to a rigorous double-blind peer review process, to ensure quality and originality. We are interested in original research discoveries. This journal also features a wide range of research in ancillary areas relevant to chemistry.

ACE publishes original research articles, review articles, editorials, case reports, letters, brief commentaries, perspectives, methods, etc.

The research topics of ACE include but are not limited to:

1. Analytical chemistry
2. Chemical engineering
3. Materials chemistry
4. Material synthesis
5. Catalysis
6. Process chemistry and technology
7. Quantum chemistry method
8. Environmental chemical engineering
9. Bio-energy, resources, pollution
10. Reaction kinetics
11. Nanotechnology and bioreactors
12. Surface, coating and film

EnPress Publisher, LLC

EnPress Publisher, LLC, is a scholastic conduit for an assembly of professionals in the domains of science, technology, medicine, engineering, education, social sciences, and many more, as a round table for their intellectual discourse and presentation, and as an instrument to galvanize research designs, policy implementation, and commercial interests, to facilitate the prevailing over their challenges and to encourage to the full advantage of their resources and true potential.

We are the intellectual and academic home for academics, educators, scholars, clinicians, corporate researchers, who all play important roles in a wide range of national and international research organizations, and whose interests, expertise, research approaches, and industry objectives from around the world coalesce together to advance significant contributions in their research and professional fields.

As an instrument of information purveyor, we seek to combine academic rigor and originality with the nuanced development of policy and practice. Via our journals, client database, online campaigns, and social media presence, we offer a platform for industry professionals to interconnect, as well as opening doors towards cost-effective solutions for them to succeed, and we confidently hope to inspire a new generation of multidisciplinary researchers, think-tank experts, policymakers and business entities to innovate and advance their knowledge across fields.



EnPress Publisher, LLC

Add: 14701 Myford Road, Suite B-1, Tustin, CA 92780, United States

Tel: +1 (949) 299 0192

Email: contact@enpress-publisher.com

Web: <https://enpress-publisher.com>